AlCrVN – Design of high-temperature low-friction coatings

Dipl.-Phys. Robert Franz

Leoben, October 2007

being a thesis in partial fulfilment of the requirements for the degree of a

Doctor of Montanistic Sciences (Dr. mont.)

at the University of Leoben

This thesis was supported by the Christian Doppler Research Association in the framework of the Christian Doppler Laboratory for Advanced Hard Coatings at the Department of Physical Metallurgy and Materials Testing at the University of Leoben, Austria, in cooperation with the Institute of Mineralogy and Petrography at the University of Innsbruck, Austria, as well as Plansee GmbH in Lechbruck, Germany, and Oerlikon Balzers AG in Balzers, Principality of Liechtenstein.

Affidavit

I declare in lieu of oath that I did the PhD thesis by myself using only literature cited in this volume.

Leoben, October 2007

Acknowledgement

I would like to thank Christian for giving me the opportunity to carry out this work, having great trust in me and allowing a physicist to play with engineer's machines.

I am also very grateful to my office mate Jörg who revealed a tremendous patience in discussing with me subjects concerning work, life, the universe and all the rest. A special thanks is due to always encouraging me to rewrite my manuscripts just one more time.

A lot of the data that is included in this thesis has been measured by my colleagues in Innsbruck. I am thankful to Bernhard, Reinhard and Richard for supplying me with chemical analyses of my coatings and helping me out when crystallography stood in the way between me and a scientific conclusion.

To our project partners Plansee and Oerlikon Balzers, in particular Peter and Michael as well as Volker, Wolfgang, Andreas, Orlaw, Markus and Denis, I am very grateful for generously providing me with targets, substrates etc. and, most of all, rendering the CD laboratory possible.

To all the people from the thin films group, Christian T., Claudia, David, Florian, Gerardo, Harald, Jörg P., Kerstin, Martin M., Martin P., Nazanin, Paul, Rostislav, Vicky as well as the former members Gert, Herbert and Joe, it was a great time working with you.

Not to be forgotten: Hilde who was always available to help me finding a way through the Austrian bureaucracy and many other things.

Danksagung

Ein ganz besonderes Dankeschön gilt meinen Eltern, Maria und Manfred, für ihre Unterstützung während meiner gesamten Studienzeit, unabhängig davon wo in Europa ich mich gerade aufhielt. Das Gleiche gilt auch für meine Geschwister Cordula, Katharina, Ulrike und Philipp sowie Lars, Enrico und Thomas und nicht zu vergessen Konrad, Rebekka, Amélie und Ruben, die ich alle immer viel zu selten sehe.

Agradecimento

O último e mais importante obrigado é reservado para a minha querida esposa Marisa. O teu amor ajuda-me imenso a passar a minha vida todos os dias, mesmo quando faço coisas menos importantes como escrever uma tese de doutoramento.

Preface

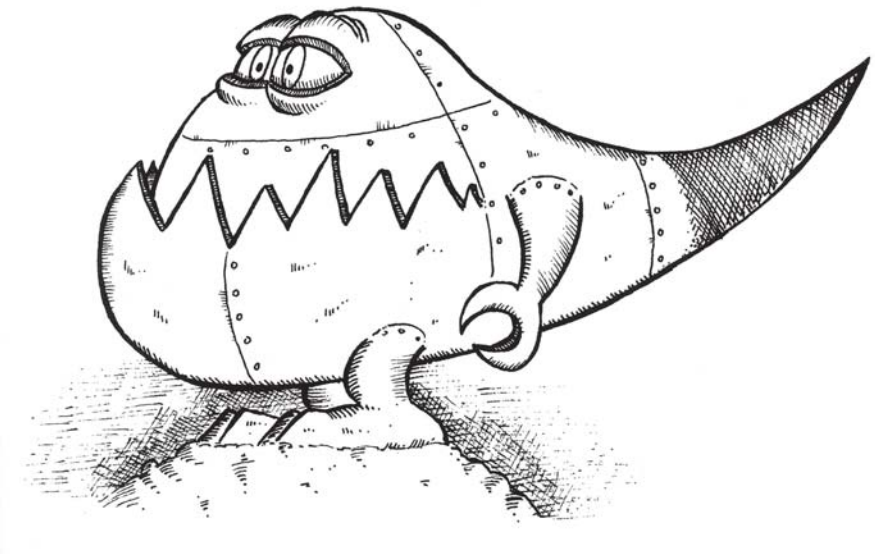

Aus dem
»Lexikon der erklärungsbedürftigen Wunder, Daseinsformen und Phänomene Zamoniens und Umgebung«
von Prof. Dr. Abdul Nachtigaller

Finsterbergmade, die: Die Finsterbergmade (Mado inferioris) oder *Eisenmade* gehört, obwohl man es bei ihrem Äußeren kaum zu glauben vermag, zur Spezies der ordinären Erdwürmer, freilich auf einer sehr hohen Entwicklungsstufe. [...] Sie leben davon, sich durch die Metallschichten der Finsterberge (wo sie ausschließlich beheimatet sind) zu arbeiten und dabei alle Nährstoffe aus dem gefressenen Metall zu filtern und zu verdauen. Dafür sind sie mit außergewöhnlichen Kauwerkzeugen ausgestattet, um die sie jeder Raubsaurier beneiden würde. Die ausgewachsene Finsterbergmade ist außerdem in der Lage, Feuer zu speien, ähnlich wie die Feuerwerksdrachen des brasilianischen Regenwaldes, mit denen sie aber nicht verwandt ist, denn Drachen gehören zur Familie der Knotenhäutler, während die Oberfläche der Finsterbergmade von poliert wirkender Struktur ist. Der ganze Körper der Finsterbergmade ist aus schimmerndem rostfreien Edelstahl. Sie hat einen Unterkiefer in der Form einer Baggerschaufel, besetzt mit diamantstaubbeflockten Sägezähnen. Anstelle von Armen hat die Made Kneifzangen, als Füße Stahlklauen, und ihr Hinterkörper läuft in eine riesige Metallfeile aus. [1]

From the
'Encyclopedia of Marvels, Life Forms and Other Phenomena of Zamonia and its Environs'
by Professor Abdullah Nightingale

Mountain Maggot, The. Although its outward appearance renders this hard to believe, the Mountain or *Iron Maggot* (Vermis montanus) belongs to the same family as the commom earthworm, but is much more highly developed. [...] They live by gnawing their way through the mineral deposits in the Gloomberg Mountains (their only habitat), filtering all the nutrients out of the metal they devour, and digesting them. For this purpose they are equipped with masticatory organs so exceptional that any saurian predator would covet them. The mature Mountain Maggot is also capable of spitting fire like the Firework Dragon of the Brazilian rain forest, to which it is not, however, related, for dragons belong to the nodulodermal family, whereas the Mountain Maggot's epidermis is so smooth that it looks polished. Its entire body does, in fact, consist of gleaming stainless steel. Its lower jaw is shaped like an excavator shovel edged with sawteeth coated in diamond dust. It has pincers in lieu of hands and steel claws in lieu of feet, and its body terminates in a huge, tapering metal file. [2]

References

[1] W. Moers, *Die 13 1/2 Leben des Käpt'n Blaubär* (Eichborn, Frankfurt am Main, 1999).
[2] W. Moers, *The 13 1/2 Lives of Captain Bluebear* (The Overlook Press, Woodstock & New York, 2006), translated by John Brownjohn.

Contents

1 Introduction **1**

2 Tribology **3**
2.1 Friction and wear . . . 3
2.2 Lubrication . . . 5
2.2.1 Solid lubricants . . . 6
2.2.2 Lubricious oxides - Magnéli phases . . . 8

3 Material selection **11**
3.1 AlCrN hard coatings . . . 11
3.2 Vanadium oxides - V_2O_5 . . . 13
3.3 Nitride coatings with incorporated V . . . 14

4 Coating synthesis **21**
4.1 Arc-evaporation . . . 21
4.1.1 Cathode spot . . . 21
4.1.2 Arc source design and magnetic fields . . . 23
4.1.3 Macroparticles . . . 24
4.2 Thin film growth . . . 26
4.2.1 Nucleation . . . 26
4.2.2 Microstructure - Structure zone models . . . 27
4.2.3 Ion bombardment . . . 30
4.3 Synthesis of V alloyed AlCrN hard coatings . . . 31

5 Coating characterisation **35**
5.1 Ball-on-disc tests and optical profilometry . . . 35
5.2 Raman spectroscopy . . . 36
5.3 Secondary ion mass spectrometry (SIMS) . . . 39
5.4 Transmission electron microscopy (TEM) . . . 41
5.5 X-ray photoelectron spectroscopy (XPS) . . . 44

6 Summary **49**

7 Abbreviations **51**

8 Publications **53**
8.1 List of included publications . . . 53
8.2 List of related publications . . . 53
8.3 My contribution to included publications . . . 54

Publication I **55**

Publication II **69**

Publication III **83**

Publication IV **97**

Publication V **113**

1 Introduction

The importance of surface science arises from the fact that any interaction between two bodies is solely mediated by their surfaces. Since, nowadays, a control of the surface constitution on an atomic scale is feasible, the physical and chemical properties of the near surface area can be altered according to specific requirements. This can be accomplished by incorporating auxiliary material using, e.g., implantation or by covering the surface with a thin film of a different material. For the latter case, several different techniques have been developed while within this work arc-evaporation was applied for synthesising the coatings. In general, coatings are used in optical, electronic and magnetic devices, machine parts and tools and for decorative purposes, whereas the present thesis focuses on wear resistant and low-friction coatings that are applied to protect bearings, gears, metal cutting and forming tools, hard discs and biomedical devices. A great success has been achieved by applying combinations of a tough base material and a hard coating in metal cutting and forming applications where very demanding contact situations are commonly encountered and the materials have to withstand temperatures of up to 1000°C and contact pressures exceeding 1.2 GPa [1].

Hard coatings are generally characterised by high hardness and toughness and a superior thermal stability and oxidation resistance. The first coatings applied were binary nitrides and carbides like TiN, CrN and TiC as well as diamond or diamond-like carbon (DLC) coatings. A major progress in terms of improving the mechanical properties and oxidation resistance has been achieved by depositing metal-aluminium ternary nitrides like TiAlN and AlCrN leading to an enhanced cutting performance. On the other hand, these coatings reveal an increased level of residual stress causing problems in the adhesion to the substrate and spalling of the entire coating is frequently observed. In order to accommodate the high stress states, multilayer coatings including an optimised adhesion layer have been developed. Additionally, multilayer or superlattice coatings as well as nanocomposites may combine rather different properties that originate from the individual material subsystems, while, beyond this, also new properties can emerge due to, e.g., superlattice or composite hardening. Nevertheless, so far no single or particular arrangement of coatings exists that can fulfil all requirements, especially because of the enormous variety of application situations commonly associated with contradicting demands. Thus, the design of hard coatings with tailored properties for certain applications presents a promising strategy.

The contribution of the present work is due to the development of a coating that offers lubricious effects at elevated temperatures while maintaining the necessary level of mechanical integrity. At temperature ranges normally encountered in metal cutting and forming, the usually applied low-friction coatings like TiCN and DLC lose their lubricating properties due to oxidation or other processes leading to early coating failure. Other more oxidation resistant coatings like TiAlN and AlCrN reveal a rather high coefficient of friction at elevated temperatures which in turn results in an amplified energy dissipation in the tri-

bological contact zone. This situation is usually overcome by the addition of supplemental lubricants, even though ecological as well as economical considerations favour cutting with reduced coolants or even dry cutting. Therefore, the design of next generation hard coatings is aiming for combining the apparent good mechanical integrity of the state-of-the-art hard coatings with friction reducing effects in order to limit the heat generation in tribological operations. For this work, AlCrN was chosen as it exhibits high hardness values and an oxidation resistance up to ∼1000°C [2], whereas V was added since the oxides that it forms at elevated temperatures are known to act as solid as well as liquid lubricants [3].

The outline of the thesis at hand starts with a general overview of tribological aspects regarding friction and wear as well as lubrication with a focus on solid lubricants. In the next chapter, the involved materials, i.e., AlCrN hard coatings and V_2O_5, are characterised in detail by reviewing the published literature, whereas a survey of similar approaches is included in order to estimate expected results as well as for comparative purposes. Subsequently, the synthesis of V alloyed AlCrN coatings is described by first explaining the technique used for depositing the coatings and second summarising the possible growth mechanisms and the resulting microstructures. Characterisation methods applied to study the deposited AlCrVN are disclosed in Chapter 5 while the methods that provided the key findings within this work are described in detail. Finally, a summary of the obtained results is given in order to point out the interrelationship between synthesis, structure, oxidation behaviour as well as mechanical and tribological properties.

Details concerning the findings and conclusions are presented in the appended publications, while cross references in the text guide to the relevant paper. The order of the publications is structured as follows: Publication I summarises the tribological observations regarding AlCrN coatings covering the complete composition range from pure CrN to pure AlN. The effects of the V incorporation as to the tribological properties and the microstructure are addressed in Publication II and III, respectively. As expected, oxidation, i.e., the formation of V_2O_5, plays a major role in reducing the friction and, therefore, one coating was analysed with respect to the occurring diffusion and oxidation processes during annealing experiments in Publication IV. Correlations between the structural evolution, formation of oxides and tribological behaviour are described in Publication V including also preliminary results of application tests.

References

[1] K. Holmberg and A. Matthews, *Coatings Tribology: Properties, Techniques and Applications in Surface Engineering*, vol. 28 of *Tribology Series* (Elsevier, Amsterdam, 1994).

[2] A. Reiter, V. Derflinger, B. Hanselmann, T. Bachmann, and B. Sartory, Surf. Coat. Technol. **200**, 2114 (2005).

[3] G. Gassner, P. Mayrhofer, K. Kutschej, C. Mitterer, and M. Kathrein, Tribol. Lett. **17**, 751 (2004).

2 Tribology

The science of contacting surfaces in relative motion is nowadays denoted by the term 'tribology' which includes all phenomena related to friction and wear. Although the very complex fundamental effects in tribology are not yet fully understood, controlling the friction and wear in numerous industrial applications is a major issue. Studying the tribological behaviour of AlCrVN hard coatings with an emphasis on the lubricious effects of the formed oxides at elevated temperatures is a central point within this work and, therefore, a brief overview of the basic principles of friction and wear as well as lubrication is presented in this chapter.

2.1 Friction and wear

As difficult as a fundamental understanding of friction and wear seems, their definition is rather clear. Friction being the resistance to the relative motion of two bodies with their surfaces in contact is characterised by three basic laws [1, 2]:

1. The friction force F_f is proportional to the normal force F_N: $F_f = \mu F_N$, defining the coefficient of friction μ which is abbreviated by COF in the following.

2. The friction force is influenced by the real area of contact as due to surface roughness contact between two solid bodies only occurs at the asperities. If the applied load is low causing only elastic deformation of the asperities, the situation can be described as a Hertzian contact. Higher loads leading to plastic deformation of the softer material are associated with an increased real area of contact. More details about the real and apparent area of contact can be found in many tribology books [1–4].

3. The friction is independent of the sliding velocity.

In general, the first two laws are well obeyed, whereas the third law is only true when sliding is already established rather than during the initiation of such a process. According to Suh and Sin, six stages can be distinguished before reaching steady-state friction while three different mechanisms contribute to the overall friction: adhesion, ploughing and asperity deformation [5].

On the other hand, material removal from two contacting solid surfaces as a result of moving over one another is determined as wear [1, 2]. From the total volume V of the removed material the wear rate or wear coefficient is calculated:

$$K = \frac{V}{w \cdot s} ,$$

with the applied load w and the sliding distance s [6]. This equation is derived from the relationship as observed by Holm and Archard:

$$V = K' \cdot \frac{w \cdot s}{H} \ ,$$

with the hardness of the material H and $K' = K \cdot H$. Although, expressing the wear coefficient K as defined above is not ideal, it is widely used and is supported by the physical argument that the worn volume is divided by the mechanical energy input into the contact. Further, friction and wear are strongly bonded as they both result from a tribological process, but the details of their interrelationship are still not well understood and, in case of wear, no general classification of the wear mechanisms has been established up to now. However, four different effects, namely adhesive, abrasive, fatigue and chemical wear, are generally accepted [6]. Adhesive wear due to strong adhesion and formation of asperity junctions was the dominating wear theory for sliding contacts after Bowden and Tabor [3]. On the contrary, material removal due to ploughing, wedge formation and cutting leading to abrasive wear is present on a large scale in metal cutting operations. Further, fatigue appears if the surface is exposed to repeated loading and unloading. In sliding contacts cracks can nucleate and propagate below the surface causing the delamination of long and thin wear debris. Among the chemical wear processes, oxidation is the most common. Although a thin oxide layer sometimes might actually protect the underlying surface, its continuous removal leads to oxidative wear.

The above presented effects of friction and wear were mainly obtained from investigations of metal surfaces. In the last decades new methods in the field of surface engineering were developed and, especially, the deposition of protective hard coatings was very successful in reducing undesired friction and wear [7]. However, introducing another component to the tribological contact leads to an even more complex situation and new effects have to be added to the general description. As shown in Figure 2.1, Holmberg and Matthews classified the tribological mechanisms of coated surfaces as being macromechanical, micromechanical, tribochemical as well as mechanisms of material transfer and the nanophysical contact [6, 8, 9]. In the following a brief overview of this classification is presented.

Macromechanical friction and wear mechanisms The macromechanical tribological mechanisms consider the stress and strain distributions in the entire contact, the resulting elastic and plastic deformation and the formation and dynamics of the wear particles. There are four main parameters that influence the tribological contact: coating-to-substrate hardness relationship, coating thickness, surface roughness and the size and hardness of the wear debris. As in the present case of a hard coating on a soft substrate, several conditions determining friction and wear can be distinguished. These contact conditions are schematically depicted in Figure 2.2 and further explained in Reference [6].

Micromechanical tribological mechanisms If stress and strain are considered at an asperity level, then micromechanical mechanisms can be observed. Shear and fracture influence the nucleation and propagation of cracks that finally might result in material liberation. In general, the friction and wear phenomena as discussed above originate from these micromechanical processes.

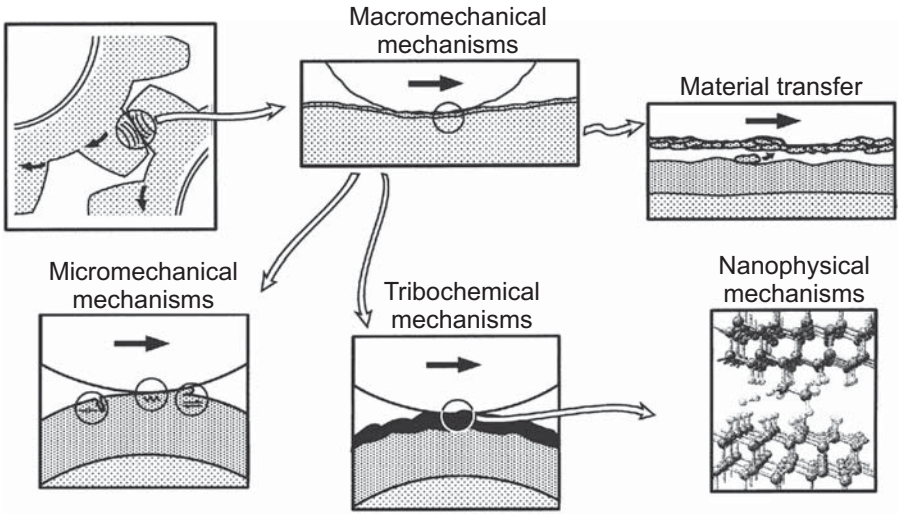

Figure 2.1: Categories of contact mechanisms according to Holmberg and Matthews [9].

Tribochemical mechanisms High local pressures and flash temperatures exceeding 1000°C at the asperities can trigger chemical reactions in the tribological contact zone. On hard coatings thin microfilms with low shear strength can form which might explain the low-friction behaviour observed for some coatings. On a micro scale, this situation is equal to a soft coating on a hard substrate which is commonly attributed to a distinct reduction of friction. However, most common in practical applications is the formation of oxide microfilms. Depending on the properties of the oxide layer, the tribological contact adapts and a friction and wear behaviour influenced by the formed oxides is observed.

Mechanisms of material transfer In a similar way as the formation of microfilms on hard coatings influences the tribological contact, material transfer from or to the counterface results in a new material pair. If the wear debris attaches to the counterface, sliding of coating versus transfer layer occurs, whereas sliding of counterface versus counterface can appear in case of soft counterface materials.

Nanophysical contact mechanisms These mechanisms include all tribological phenomena related to the interaction between molecules and atoms, such as the effects of van der Waal's forces and related interatomic phenomena. Even though no comprehensive theory could be established up to now, since investigations of the material's crystal and bonding structure influencing friction and wear have only been possible in the past few years, more details about the origin and also the existence of friction can be expected from this emerging field [8–11].

2.2 Lubrication

Traditionally, the most common way of reducing friction and wear in a tribological contact is due to the usage of lubricants. Various materials can serve as lubricants and it is convenient

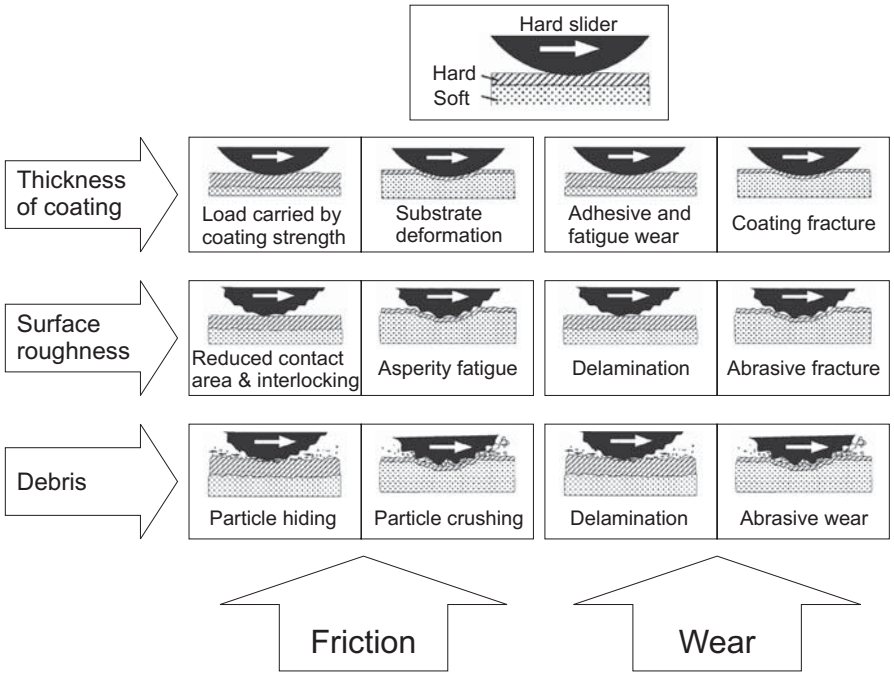

Figure 2.2: Macromechanical contact conditions for different mechanisms which influence friction and wear in case a hard spherical slider moves on a hard coating with a soft substrate underneath [6].

to distinguish between three types of lubrication [2, 4]. In hydrodynamic lubrication the pressure created within the lubricant is sufficient to support the normal load and the sliding surfaces are completely separated by a relatively thick film of a fluid lubricant. If the thickness of the lubricating film is reduced due to, e.g., different geometries of the surfaces, then elastic deformation of the surface occurs and the elastohydrodynamic lubrication regime is active. In case of boundary lubrication, the surfaces are only separated by an adsorbed molecular film with low shear strength. Asperity contact and junction formation occur, but are reduced as compared to dry sliding.

2.2.1 Solid lubricants

Liquid and grease lubricants have made a great success in reducing friction and wear, starting already a few 1000 years ago. Limitations are, however, given when severe conditions in the tribological application are present. At very low or high temperatures, in vacuum or extreme contact pressures the only way to control the tribological behaviour might be by using solid lubricants. Erdemir summarised the key advantages of solid lubricants in tribological applications over liquid and grease lubricants in Reference [12] and presented a classification of solid materials with self-lubricating capabilities including the following groups: lamellar solids, soft metals, mixed oxides, single oxides, halides and sulfates of alkaline earth metals, carbon-based solids and organic materials or polymers. In general, solid lubricants are materials that reveal a low shear strength which in turn can arise from a variety of specific properties. In Figure 2.3 the basic sliding mechanisms of solid lubricants are illustrated. Soft

metals owe their lubricity to a crystal structure with multiple slip planes and the fact that they do not work harden noticeably. Examples of soft metals used as solid lubricants are Ag and Pb. Among the polymers polytetrafluoroehtylene (PTFE) is most common. Polymers consist of long molecular chains, are highly chemically inert and/or have a very low surface energy which avoids sticking effects or makes them insensitive to chemical bonding.

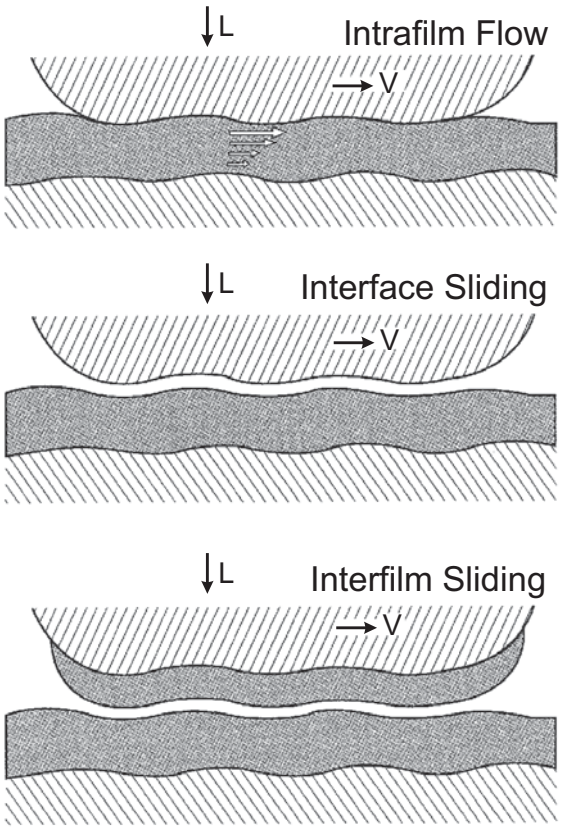

Figure 2.3: Schematic illustration of the mechanisms by which sliding can be accommodated between an uncoated and a coated surface [12].

However, most widely used in solid lubrication are lamellar solids, e.g. MoS_2, graphite, hexagonal boron nitride and boric acid H_3BO_3. They reveal a unique layered structure where the atoms within the layers are closely packed and strongly bonded. The distance between the layers is more extended and the bonding is only due to weak forces, e.g. van der Waals forces. In a sliding contact, these layers can align parallel to the direction of relative motion and slide over each other which in turn reduces the friction. In general, lubrication by lamellar solids is due to an interlayer shear mechanism, but the formation of a smooth transfer film on the counterface material as shown in Figure 2.3 was also found to be important in order to accommodate the sliding velocity.

A major drawback in using lamellar solids as lubricants is the strong dependence of their friction and wear behaviour on the test environment and/or conditions. Graphite and boric acid need moisture or other condensable vapours to lubricate, otherwise the coefficient of friction increases drastically. On the contrary, MoS_2 reveals the lowest friction in vacuum or

dry atmospheres. The presence of humidity can increase the COF by more than two orders of magnitude. However, a factor affecting most of the presented lubricants detrimentally is due to thermal degradation at elevated temperatures.

2.2.2 Lubricious oxides - Magnéli phases

In modern industrial operations like metal cutting, it is very common that the tribological contact zone is exposed to ambient air during the application process while the temperatures exceed 500°C easily. As mentioned, most of the lamellar solids decompose in this temperature range due to the limited thermal stability which is accompanied by a loss of the lubricious effects [12]. As a result, the sliding surfaces oxidise and friction and wear are subsequently dominated by the formed oxide films while severe abrasive wear leading to an early failure of the system can occur in case of wear debris particle generation.

On the contrary, oxides with low shear strength can serve as lubricants at elevated temperatures and are, therefore, referred to as lubricious oxides. Pioneering work by Gardos in 1988 demonstrated that oxygen vacancies in rutile TiO_2 significantly change the shear strength in the surface region and in the bulk [13]. A reduction from $\sim TiO_2$ to $TiO_{1.93-1.98}$ results in a decrease of the shear strength τ_S from 21 MPa to 8 MPa [14]. This value of $\tau_S = 8$ MPa is in the range of sputtered MoS_2 films in vacuum presenting a shear strength of 7–10 MPa [14]. Further work by Gardos revealed the interrelationship between shear strength, coefficient of friction and the oxygen stoichiometry of TiO_{2-x} in detail [15]. There, the lowest COF of 0.08 was obtained for an O/Ti ratio of ∼1.98. Similarly, dry sliding tests of different ceramic composites containing Ti by Woydt et al. revealed the formation of substoichiometric TiO_{2-x} due to tribo-oxidation processes [16]. The lubricious oxides were tribologically active up to high temperatures reducing the wear, whereas a distinct reduction of the COF could not be noticed. After testing at 400°C and 800°C, γ-Ti_3O_5, Ti_5O_9, Ti_9O_{17} and a few double oxides were evidenced beside TiO_2.

First investigations of the crystal structure of substoichiometric metal oxides were done by Magnéli, who discovered that Mo and W form oxides with planar faults belonging to homologous series based on the common structural principles Me_nO_{3n-1} or Me_nO_{3n-2} [17]. Similar studies on the Ti-O system by S. Andersson et al. revealed the series Ti_nO_{2n-1} ($4 \leq n \leq 9$) in the composition range $TiO_{1.7-1.9}$ [18]. Their structure can be derived from a perfect rutile parent by crystallographic shear at regular intervals on planes parallel to (121). The series can be extended to compositions of $TiO_{1.9-2.0}$ with $16 \leq n \leq 40$, but the shear planes are now parallel to (132) [16]. All oxides possess a high concentration of vacancies and different stoichiometries are attained by different spacings between the crystallographic shear planes. The apparent parallelism between Ti and V oxides was first reported by G. Andersson who indicated the existence of a homologous series corresponding to the formula V_nO_{2n-1} with $n \geq 4$ [19]. In general, these sequences of oxides with ordered structures and definite but 'grotesque' stoichiometries are referred to as Magnéli phases. However, a shortcoming of TiO_x-based and analogue solid lubricants is the very narrow range of oxide stoichiometry where a good lubricity is obtained [12].

A new approach for predicting the lubricity of oxides or oxide mixtures was introduced by Erdemir applying the principles of crystal chemistry [20]. The crystal chemical parameter of interest is the ionic potential or cationic field strength $\varphi = Z/r$, defined as the ratio between the formal cationic charge Z and the radius of the cation r by Dietzel [21], who

also obtained a strong interdependence between the melting point of an oxide and its ionic potential. Further, a close relationship between the heat of formation of many oxides and the ionic potential of their cations was discovered by Knapp [22]. In general, a high ionic potential is related to an extensive screening of the cation by the surrounding anions. Oxides with highly screened cations are normally soft and their melting points are low. Re_2O_7, e.g., where the Re ion has a charge of $Z = 7$ and a radius of $r(Re^{7+}) = 0.52$ is described by an ionic potential of $\varphi = 13.46$ and a melting point of 297°C [23]. The lubricity of these oxides arises from the fact that highly screened cations interact only very little with other cations which allows for easy shearing. Figure 2.4 presents a comparison between the ionic potential and measured coefficients of friction at elevated temperatures. There, it can be noticed, that V_2O_5 with an ionic potential of $\varphi = 10.2$ reveals a COF of ∼0.2. The structure of V_2O_5 in an idealised way can be considered as built up of infinitely extending groups of MeO_6 octahedra joined at the edges [17]. In case of the homologous series Me_nO_{3n-1} or Me_nO_{3n-2}, two or four MeO_6 octahedra are participating in the joining of the blocks. More details concerning the structure of V_2O_5 are presented in Section 3.2.

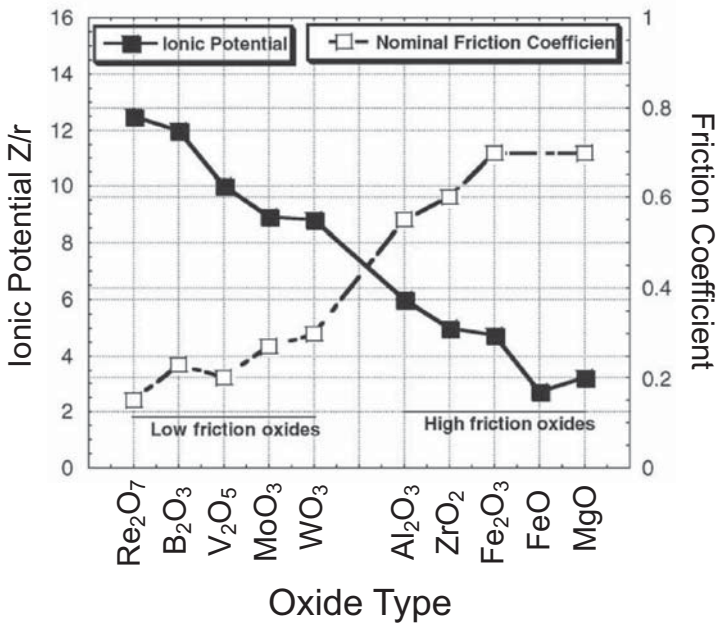

Figure 2.4: Relationship between ionic potentials and averaged coefficients of friction of various oxides [24].

References

[1] E. Rabinowicz, *Friction and Wear of Materials* (Wiley-Interscience, New York, 1995), 2nd ed.

[2] I. Hutchings, *Tribology - Friction and Wear of Engineering Materials* (Edward Arnold, London, 1992).

[3] F. Bowden and D. Tabor, *The Friction and Lubrication of Solids* (Clarendon Press, Oxford, 1954).

[4] B. Bhushan, *Principles and Applications of Tribology* (John Wiley & Sons, New York, 1999).
[5] N. Suh and H. Sin, Wear **69**, 91 (1981).
[6] K. Holmberg and A. Matthews, *Coatings Tribology: Properties, Techniques and Applications in Surface Engineering*, vol. 28 of *Tribology Series* (Elsevier, Amsterdam, 1994).
[7] Y. Pauleau and P. B. Barna, eds., *Protective Coatings and Thin Films* (Kluwer Academic Publishers, Dordrecht, 1997).
[8] K. Holmberg, A. Matthews, and H. Ronkainen, Tribology International **31**, 107 (1998).
[9] K. Holmberg, H. Ronkainen, and A. Matthews, Ceramics International **26**, 787 (2000).
[10] B. Bhushan, ed., *Handbook of Micro/Nano Tribology* (CRC Press, 1999), 2nd ed.
[11] K. Holmberg, H. Ronkainen, A. Laukkanen, and K. Wallin, Surf. Coat. Technol. (2007), doi:10.1016/j.surfcoat.2007.07.105.
[12] A. Erdemir, in *Modern Tribology Handbook*, edited by B. Bhushan (CRC Press, Boca Raton, 2001), vol. 2, chap. 22, pp. 787–825.
[13] M. Gardos, Tribology Transactions **31**, 427 (1988).
[14] M. N. Gardos, H.-S. Hong, and W. O. Winer, Tribology Transactions **22**, 209 (1990).
[15] M. Gardos, Tribol. Lett. **8**, 65 (2000).
[16] M. Woydt, A. Skopp, I. Dörfel, and K. Witke, Tribology Transactions **42**, 21 (1999).
[17] A. Magnéli, Acta Crystallogr. **6**, 495 (1953).
[18] S. Andersson, B. Collén, U. Kuylenstierna, and A. Magnéli, Acta Chem. Scand. **11**, 1641 (1957).
[19] G. Andersson, Acta Chem. Scand. **8**, 1599 (1954).
[20] A. Erdemir, Tribol. Lett. **8**, 97 (2000).
[21] A. Dietzel, Z. Elektrochem. **48**, 9 (1942).
[22] W. J. Knapp, J. Am. Ceram. Soc. **36**, 43 (1953).
[23] D. R. Lide, ed., *CRC Handbook of Chemistry and Physics* (CRC Press, 2004), 85th ed.
[24] A. Erdemir, Surf. Coat. Technol. **200**, 1792 (2005).

3 Material selection

Within this chapter a detailed review of the available literature concerning the base materials is provided. Further, similar approaches for designing low-friction coatings applicable at elevated temperatures are presented, whereas some results obtained from the investigation of the AlCrVN coatings are included for comparison.

3.1 AlCrN hard coatings

The development of AlCrN hard coatings was initially inspired by the incorporation of Al into TiN. The so formed TiAlN coatings were characterised by higher hardness, an improved oxidation resistance and superior wear properties as compared to TiN [1]. Increased hardness values are due to solid solution hardening effects since the Al atoms substitute the Ti atoms in the crystal lattice. The improvements in oxidation resistance could be associated with the formation of a thin protective Al_2O_3 scale on the coating surface which is of special interest as coated tools or machine parts in industrial applications are usually exposed to oxidative environments. In contrast to TiO_2, Al_2O_3 being a stable oxide hinders further oxygen diffusion into the coating because of its dense microstructure. Münz reported an onset temperature of oxidation at ~800°C which is 200 K higher than for TiN [1].

One important aspect concerning the synthesis of $Ti_{1-x}Al_xN$ and $Al_xCr_{1-x}N$ is the maximum solubility of AlN in the fcc lattice of the corresponding transition metal nitride. In thermodynamic equilibrium, AlN with its wurtzite (w) type structure (hexagonal close packed) is not soluble in either phase, but due to the growth conditions in PVD, e.g., very high cooling rates, metastable chemical compounds can be synthesised. Makino presented a theory based on band parameters that can be used to estimate the concentration where phase changes will occur when alloying transition metal nitrides with Al [2, 3]. This method applied to TiN and CrN yields a maximum solubility of AlN in the fcc crystal structure of 65.3% and 77.2%, respectively [4]. In Figure 3.1 the substitution of Cr atoms by Al atoms is depicted which finally leads to the formation of a w-AlCrN phase at higher Al contents. Several investigations covering the whole concentration range from pure CrN to pure AlN confirmed the appearance of a phase transition close to the estimated point while the actual value slightly depends on the energetics of the used deposition method [4–9]. Thermal stability studies by Willmann et al. of fcc-AlCrN in inert atmospheres revealed a decomposition of the metastable ternary compound AlCrN for temperatures exceeding 900°C [10]. The formation and growth of hexagonal AlN precipitates results in a CrN-enrichment of the remaining coating. At higher temperatures the decomposition to Cr_2N and pure Cr is accompanied by a loss of nitrogen which finally leads to a complete degradation of the original coating at ~1200°C.

As mentioned above, the addition of Al to TiN resulted in an improved oxidation behaviour of TiAlN. Thus, many studies examined the formation of oxides during annealing

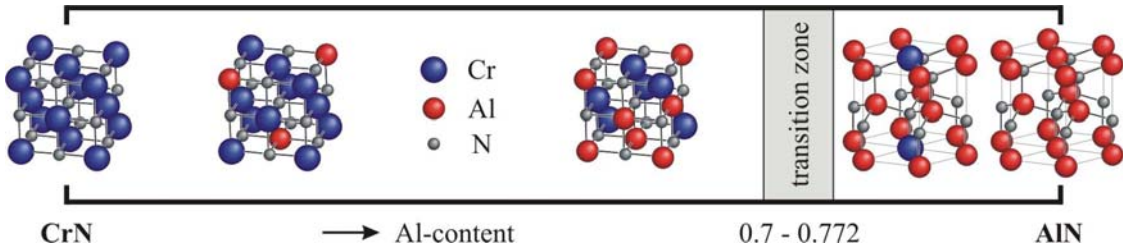

Figure 3.1: Crystal structure evolution of AlCrN hard coatings in dependence on Al content [11]. A phase transition from fcc-AlCrN to w-AlCrN appears at AlN concentrations in the range of 0.7–0.77.

of AlCrN in air expecting similar effects, whereas, contrary to TiO_2, Cr_2O_3 with its self-passivating properties should be beneficial [8, 12–18]. Kawate et al. reported on a superior oxidation resistance of the investigated AlCrN coatings as compared to TiAlN [16]. A detailed oxidation study by Banakh et al. revealed the presence of a mixed $(Cr,Al)_2O_3$ phase after the heat treatment in air at 900°C [15]. Further, higher Al contents shift the onset of oxidation to higher temperatures and the best resistance was observed for coatings with concentrations of $x = 0.34 \ldots 0.63$. The formed oxide layer can be as thin as 100 nm after exposure to ambient air for 30 min at a temperature of 1050°C as shown by Reiter et al. [8]. There, the best oxidation behaviour was found for $Al_{0.71}Cr_{0.29}N$ and $Al_{0.46}Cr_{0.54}N$, i.e., for coatings with an Al concentration close to the maximum solubility. The oxidation resistance of w-AlCrN decreases despite the higher Al content. In general, AlCrN offers an improved oxidation behaviour as compared to TiAlN while the highest possible onset of oxidation is in the range of 900–1000°C depending on the Al content, crystal structure and deposition method.

Traditionally, most attention when investigating AlCrN hard coatings is paid to the mechanical properties [6, 8, 12–14, 19–28]. Thereby, a direct comparison of the published data is not very conclusive since different measurement methods were applied and the coatings were synthesised by a wide range of deposition techniques and conditions. From the publications covering the whole composition range of Al-Cr-N, Hirai et al. and Kawate et al. obtained a similar maximum Vickers hardness of ∼2700 for the composition with the highest Al content, but still with fcc crystal structure [6, 14]. This result was corroborated by Reiter et al. who obtained a maximum hardness of $HU_{pl} = 38$ GPa in the same composition range [8]. The influence of the applied bias voltage during deposition on the mechanical properties was investigated by Romero et al. [28]. For coatings with an Al/Cr ratio of slightly less than 0.75 and deposited at bias voltages ranging from −50 to −400 V, hardness values of 31–40 GPa were obtained without correlation to the applied bias voltage. Within the work at hand, a series of AlCrN coatings has been synthesised and investigated as to their mechanical properties. The results are presented in Publication V and reveal slightly higher hardness values from ∼32 to ∼34 GPa for an increase of the bias voltage from −40 to −150 V. The residual coating stress, on the other hand, rises distinctly from –1.6 to –3.7 GPa.

Comprehensive studies of the tribology of AlCrN are rather rare in literature [12, 13, 24, 26, 28, 29]. Ide et al.obtained a COF of ∼0.4 when testing against Al_2O_3 balls at room

temperature while a slight increase for higher Al contents can be noticed [13]. For elevated temperatures up to 500°C the COF is in the range of 0.6–0.8. In terms of wear a reduction of the wear rate by more than one order of magnitude was revealed using AlCrN coatings as compared to TiN and TiAlN [13]. Closely related to tribological testing are application tests like metal cutting or forming. Instead of studying the properties using laboratory equipment and methods, the suitability of the coating for usage in industrial operations is of interest in this case. Due to its, in general, superior properties, AlCrN presents excellent results in milling [27, 30, 31], turning [25, 29, 31] and drilling [8] of metal as well as gear cutting [31] and wood machining [32].

Publication I contains a detailed analysis of the tribological properties of arc-evaporated AlCrN with a focus on the high-temperature behaviour as these temperatures are commonly encountered in metal cutting operations. There, the minimum wear was observed for $Al_{0.62}Cr_{0.38}N$ which correlates well with the best oxidation resistance and maximum hardness as mentioned before. However, the COF can reach values of up to 1.0 leading to energy dissipation in the tribological contact zone and, in that way, even higher temperatures. An approach for reducing the friction in the relevant temperature range is presented in the following.

3.2 Vanadium oxides - V_2O_5

In Section 2.2.2 the concept of lubricious oxides for high-temperature lubrication was introduced. Several promising results have been achieved by implementing the functionality of vanadium oxides, in particular V_2O_5, as most of the observed lubricious effects are attributed to its structural and physical properties. Thus, a few insights regarding the crystal structure and mechanical properties will be presented.

V_2O_5 is an important oxide in many fields of chemistry and first investigations of the crystal structure were undertaken in the 1930s [33]. It crystallises in an orthorhombic structure (space group *Pmmn*) with the lattice constants $a = 1.1512$ nm, $b = 0.3564$ nm and $c = 0.4368$ nm [34]. A general expansion of the lattice constants with increasing temperature was obtained by Galy, but no phase transition could be noticed [35]. Vanadium and oxygen form distorted VO_5 square pyramids sharing edges and corners. This results in the formation of layers parallel to the (001) plane that are only weakly bonded as shown in Figure 3.2. Since no chemical bond exists between the atoms V_a and O_{3b}, the layers are solely held by van der Waals forces between the O atoms. This specific structure allows for easy crystallographic shearing of the (001) planes giving rise to its potential use as solid lubricant.

One way to obtain lubricious coatings is due to the direct deposition of these oxides [36–47]. Different deposition techniques, e.g. magnetron sputtering, sol-gel method and thermal evaporation, have been applied and the crystallinity and the phases formed strongly depend on the conditions during deposition. Benmoussa et al. reported on the synthesis of crystalline V_2O_5 films with (001) orientation by sputtering a V_2O_5 target in the presence of oxygen [36]. Similar results could be obtained by Rajendra Kumar et al. using thermal evaporation for deposition [43]. There, a substrate temperature $T_S \geq 300$°C is needed to obtain polycrystalline films, whereas lowering the temperature results in amorphous films. Annealing of V_2O_5 films in vacuum at 400°C or higher causes a reduction to VO_2 as reported by Benmoussa [36] and Ningyi [42]. The reaction follows a sequence with several vanadium

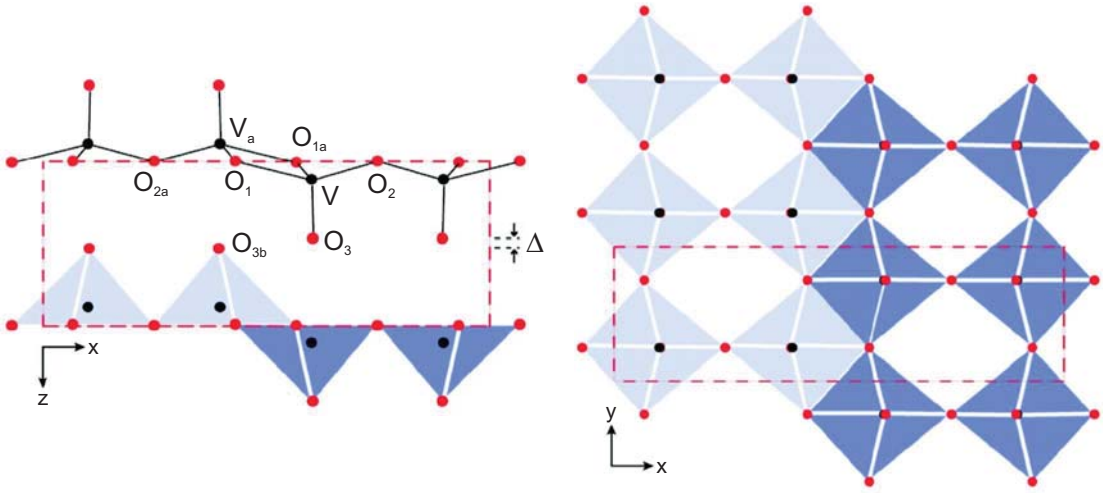

Figure 3.2: Schematic illustration of the V_2O_5 bulk crystal structure [35].

oxides formed in the intermediate steps: $V_2O_5 \rightarrow V_3O_7 \rightarrow V_4O_9 \rightarrow V_6O_{13} \rightarrow VO_2$ [42].

The mechanical properties of V_2O_5 thin films are only rarely investigated since their usage lies more within fields like, e.g., catalysis, electrochromic or optical devices. However, Lugscheider et al. measured a hardness of sputtered V-O coatings with polycrystalline V_2O_5, polycrystalline VO_2 or amorphous structure in the range of 13–18 GPa [41]. Tribological data that was obtained from tests at room temperature against a steel counterpart revealed a COF of ∼0.25. A dependence of the friction behaviour on the temperature was presented by Gulbiński et al. who recorded the COF during a temperature cycle ranging from 100–700°C using an alumina ball as counterpart [44]. At the starting temperature of 100°C a COF of 0.8 is obtained, whereas a continuous reduction to 0.3 with increasing temperature can be noticed. An apparent slight increase in friction for temperatures exceeding 660°C was associated to the melting of V_2O_5. During the cooling sequence nearly identical COF values were recorded confirming the stability of the vanadium oxide coatings while indications of phase transformation due to the annealing process are absent.

3.3 Nitride coatings with incorporated V

Nowadays, most of the hard coatings used in industry are nitrides and, hence, VN coatings were synthesised and analysed as to their friction behaviour during high-temperature ball-on-disc tests with a focus on the influences due to oxidation. As shown by Gassner et al., the oxidation of VN coatings leads to the formation of lubricious oxides on the coating surface [48]. Besides VO_2 and V_2O_5, Magnéli phases from the series V_nO_{2n-1} could be identified and the COF was reduced from 0.5 to 0.4 by increasing the temperature from room temperature (RT) to 700°C in case alumina was used as counter material. A more pronounced reduction was obtained using stainless steel balls as counterpart where the COF dropped from 1.4 at RT to 0.4 at 700°C accompanied by a noticeable decrease of the scattering. Similar results were reported by Fateh et al. who observed a minimum temperature of 500°C for the reduction of friction, whereas the COF generally decreased from 0.45 to 0.25 by increasing

the temperature from RT to 700°C [49]. However, aside from leading to the formation of lubricious oxides and reducing of friction, oxidation has severe adverse effects on the mechanical properties and high wear rates leading to early coating failure are observed.

In order to design low-friction coatings that are applicable for industrial operations, the incorporation of V into existing state-of-the-art hard coatings presents a promising strategy where possible candidates have to retain an adequate mechanical integrity in combination with a controlled V out-diffusion. Successfully prepared coatings that follow this approach are TiAlN/VN multilayers [50–56] and Ti-Al-V-N solid solutions [57–60].

First synthesis of TiAlN/VN multilayers was reported by Münz et al. using unbalanced magnetron sputtering [50]. The deposited coating crystallises in fcc structure and has a multilayer period of 3.0 nm while ball-on-disc tests against alumina at RT revealed a low COF and wear rate of 0.4 and 1.26×10^{-17} m^2N^{-1}, respectively. Raman investigations of the wear debris after testing by Constable et al. showed the formation of weakly crystalline V_2O_5, whereas annealing in air to temperatures in the range of 600–700°C resulted in the formation of crystalline V_2O_5 [51]. Different observations were, however, obtained by Luo et al. studying the TEM cross-sections of the wear track [55]. There, the formation of a tribolayer with a thickness of 20–50 nm was observed which consisted of a multicomponent oxide V-Al-Ti-O with inhomogeneous density and amorphous structure. Tribo-oxidation was clearly the dominating wear mechanism, but the formation of V_2O_5 could not be evidenced. Contrary to room temperature tests where oxidation occurs due to the very high flash temperatures in the asperities, high-temperature tests with external heating result in the formation of lubricious oxides as already mentioned. Similar to the tests on VN, ball-on-disc tests with TiAlN/VN multilayers at elevated temperatures were performed by Mayrhofer et al. [52]. First, the COF increased from 0.55 at RT to 1.0 at 500°C, but a further increase in temperature to 700°C resulted in a drop to 0.2. Mayrhofer et al. also showed that the obtained friction at this temperature is sensitive to the oxides that are formed. After a certain holding time at 700°C a transition from V_2O_5 to lower oxidised VO_2 analogue to Reference [42] was observed which is accompanied by a rise of the COF to 0.5. This reduction reaction was corroborated by differential scanning calorimetry measurements which revealed a complete transition to VO_2 at temperatures up to 1450°C as well as melting of V_2O_5 at ∼635°C. On this basis, the obtained low friction value at 700°C can be attributed to the formation and melting of V_2O_5 which acts as a liquid lubricant. The loss of V_2O_5 due to the transition to VO_2 with a higher melting point results in higher friction and the lubrication regime changes from liquid to solid.

While in TiAlN/VN multilayers VN still forms a separate phase, V atoms substitute Ti and Al atoms in the crystal lattice of Ti-Al-V-N solid solutions. Kutschej et al. reported on the synthesis and tribological behaviour of coatings with different Al/Ti ratios and varying V content [58]. The incorporation of V into TiAlN stabilises the fcc crystal structure as fcc-VN can dissolve higher amounts of Al than fcc-TiN according to Reference [4]. Tribological tests at different temperatures revealed a similar behaviour of TiAlVN as compared to the multilayer system TiAlN/VN. Depending on the V content the COF rises from 0.7–0.9 to 0.8–1.1 if the testing temperature increases from RT to 500°C, whereas a COF as low as 0.25 for the coating with the highest content of V within the experiments was obtained at 700°C. As it was the case for TiAlN/VN multilayers, the measured friction strongly depends on the oxides that are formed on the coating surface, i.e., low-friction effects are only observed in the

presence of V_2O_5 providing a liquid lubricious layer at 700°C. During longer testing times, which means longer exposure to air at elevated temperatures, $AlVO_4$ is formed by a solid state reaction of V_2O_5 and Al_2O_3 [61]. This oxide does not provide particular lubricating effects and the COF rises to 0.5–0.6 [59].

Tribological data of the newly synthesised AlCrVN hard coatings is presented in Publications II and V. First, the dependence of friction and wear on the V content was investigated revealing pronounced low-friction effects at 700°C for higher V concentrations. The lowest observed COF of 0.2 was attributed to a liquid V_2O_5 phase that was formed on the coating surface. If deposited at low bias voltages of –40 V and substituting Cr by V, the AlCrVN coatings present a dual-phase structure containing a fcc-AlCrVN and a w-AlCrVN phase since fcc-CrN can dissolve higher amounts of Al than fcc-VN. Higher energetic growth conditions as investigated in Publication III result in a reduction of the wurtzite-type phase and, finally, in a single-phase fcc-AlCrVN coating. The influence of these structural changes on the tribological behaviour is subject of Publication V. There, an increase of the COF for higher bias voltages was observed which is most likely caused by the higher oxidation resistance of the fcc-AlCrVN. In case of the single-phase fcc-AlCrVN coating deposited at –150 V, smaller amounts of V_2O_5 are formed which appears not to be sufficient for maintaining a continuous lubricious layer during the ball-on-disc tests.

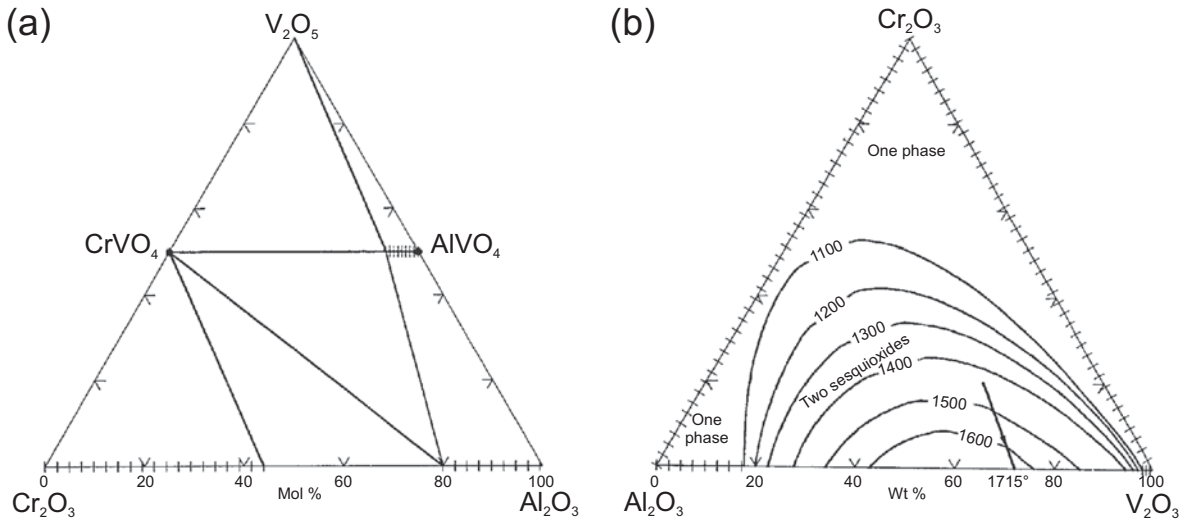

Figure 3.3: Phase diagrams of the systems (a) V_2O_5-Cr_2O_3-Al_2O_3 and (b) Al_2O_3-V_2O_3-Cr_2O_3 [62].

The processes leading to the formation of V_2O_5 were studied in several investigations that addressed the oxidation and diffusion behaviour of TiAlN/VN multilayers [52, 63–65]. A dual-layer structure of the formed oxides was observed by Zhou et al. who annealed samples at temperatures of 600°C and higher [63]. At 638°C, the presence of V_2O_5 was clearly evidenced by XRD, whereas increasing the temperature to 672°C resulted in complete oxidation and spalling of the entire coating. According to Lewis et al., the onset for rapid oxidation is in the range between 632–645°C [64]. There, TiO_2 and $AlVO_4$ were observed as the main constituents of the formed oxide at 670°C. A different situation was, however, encountered when studying the oxidation and diffusion behaviour of AlCrVN. In Publication

IV it is shown, that V_2O_5 is only detected at 700°C while at lower temperatures a mixed $(Al,Cr,V)_2O_3$ and $AlVO_4$ are present. According to the phase diagrams in Figure 3.3, the V oxides are immiscible with Al_2O_3 and Cr_2O_3 and, therefore, the formation of the dual-layer structure with a V-rich outer oxide layer and a V-depleted layer underneath can be understood by the occurrence of a phase separation. In general, the oxidation behaviour of AlCrVN coatings seems to be beneficially influenced by the higher oxidation resistance of AlCrN as compared to TiAlN [16].

The suitability of hard coatings for industrial operations is commonly evaluated in application tests and, thus, the TiAlN-based coatings with incorporated V were tested as to their cutting performance. Luo et al. reported on drilling tests of austenite stainless steel where HSS drills coated with TiAlN/VN outperformed the other tested coatings by an increase of tool lifetime of 50% and 20% as compared to TiAlN and TiCN, respectively [53]. In a similar manner, TiAlVN coatings showed a superior performance in dry milling of 42CrMo4 steels as presented by Kathrein et al. [60]. The lifetime of cemented carbide cutting inserts increased to ∼30 min as compared to ∼20 min if coated with TiAlN while the best results within these tests were obtained by using a TiAlN/TiAlVN multilayer configuration revealing a lifetime of ∼45 min. For AlCrVN coatings preliminary results are presented in Publication V where a competitive performance as compared to commercial AlCrN was obtained in side milling of stainless steel under dry conditions.

References

[1] W. Münz, J. Vac. Sci. Technol. A **4**, 2717 (1986).
[2] Y. Makino, Intermetallics **2**, 55 (1994).
[3] Y. Makino, Intermetallics **2**, 67 (1994).
[4] A. Sugishima, H. Kajioka, and Y. Makino, Surf. Coat. Technol. **97**, 590 (1997).
[5] Y. Makino and K. Nogi, Surf. Coat. Technol. **98**, 1008 (1998).
[6] M. Kawate, A. Kimura, and T. Suzuki, J. Vac. Sci. Technol. A **20**, 569 (2002).
[7] A. Kimura, M. Kawate, H. Hasegawa, and T. Suzuki, Surf. Coat. Technol. **169-170**, 367 (2003).
[8] A. Reiter, V. Derflinger, B. Hanselmann, T. Bachmann, and B. Sartory, Surf. Coat. Technol. **200**, 2114 (2005).
[9] P. Mayrhofer, D. Music, and J. Schneider, J. Appl. Phys. **100**, 094906 (2006).
[10] H. Willmann, P. Mayrhofer, P. Persson, A. Reiter, L. Hultman, and C. Mitterer, Scripta Mater. **54**, 1847 (2006).
[11] H. Willmann, Ph.D. thesis, Montanuniversität Leoben (2007).
[12] J. Vetter, E. Lugscheider, and S. Guerreiro, Surf. Coat. Technol. **98**, 1233 (1998).
[13] Y. Ide, T. Nakamura, and K. Kishitake, in *Proceedings of the Second International Conference on Processing Materials for Properties*, edited by B. Mishra and C. Yamauchi (2000), pp. 291–296.
[14] M. Hirai, Y. Ueno, T. Suzuki, W. Jiang, C. Grigoriu, and K. Yatsui, Jpn. J. Appl. Phys., Part 1 **40**, 1056 (2001).
[15] O. Banakh, P. Schmid, R. Sanjinés, and F. Lévy, Surf. Coat. Technol. **163-164**, 57 (2003).
[16] M. Kawate, A. Hashimoto, and T. Suzuki, Surf. Coat. Technol. **165**, 163 (2003).

[17] J. Sánchez-López, D. Martínez-Martínez, C. López-Cartes, A. Fernández, M. Brizuela, A. García-Luis, and J. Oñate, J. Vac. Sci. Technol. A **23**, 681 (2005).
[18] A. E. Reiter, C. Mitterer, and B. Sartory, J. Vac. Sci. Technol. A **25**, 711 (2007).
[19] O. Knotek, F. Loeffler, and H.-J. Scholl, Surf. Coat. Technol. **45**, 53 (1991).
[20] M. Okumiya and M. Griepentrog, Surf. Coat. Technol. **112**, 123 (1999).
[21] S. Ulrich, H. Holleck, J. Ye, H. Leiste, R. Loos, M. Stüber, P. Pesch, and S. Sattel, Thin Solid Films **437**, 164 (2003).
[22] E. Lugscheider, K. Bobzin, and K. Lackner, Surf. Coat. Technol. **174-175**, 681 (2003).
[23] R. Wuhrer and W. Yeung, Scripta Mater. **50**, 1461 (2004).
[24] M. Uchida, N. Nihira, A. Mitsuo, K. Toyoda, K. Kubota, and T. Aizawa, Surf. Coat. Technol. **177-178**, 627 (2004).
[25] B. Schramm, H. Scheerer, H. Hoche, E. Broszeit, E. Abele, and C. Berger, Surf. Coat. Technol. **188-189**, 623 (2004).
[26] M. Brizuela, A. Garcia-Luis, I. Braceras, J. Oñate, J. Sánchez-López, D. Martínez-Martínez, C. López-Cartes, and A. Fernández, Surf. Coat. Technol. **200**, 192 (2005).
[27] G. Fox-Rabinovich, B. Beake, J. Endrino, S. Veldhuis, R. Parkinson, L. Shuster, and M. Migranov, Surf. Coat. Technol. **200**, 5738 (2006).
[28] J. Romero, M. Gómez, J. Esteve, F. Montalà, L. Carreras, M. Grifol, and A. Lousa, Thin Solid Films **515**, 113 (2006).
[29] H. Scheerer, H. Hoche, E. Broszeit, B. Schramm, E. Abele, and C. Berger, Surf. Coat. Technol. **200**, 203 (2005).
[30] J. Endrino, G. Fox-Rabinovich, and C. Gey, Surf. Coat. Technol. **200**, 6840 (2006).
[31] W. Kalss, A. Reiter, V. Derflinger, C. Gey, and J. Endrino, Int. J. Refract. Met. Hard Mater. **24**, 399 (2006).
[32] C. Nouveau, C. Labidi, J.-P. Martin, R. Collet, and A. Djouadi, Wear **263**, 1291 (2007).
[33] J. A. A. Ketelaar, Nature **137**, 316 (1936).
[34] R. Enjalbert and J. Galy, Acta Crystallogr. C: Cryst. Struct. Commun. **42**, 1467 (1986).
[35] J. Galy, A. Ratuszna, J. Iglesias, and A. Castro, Solid State Sci. **8**, 1438 (2006).
[36] M. Benmoussa, E. Ibnouelghazi, A. Bennouna, and E. Ameziane, Thin Solid Films **265**, 22 (1995).
[37] J. Cui, D. Da, and W. Jiang, Appl. Surf. Sci. **133**, 225 (1998).
[38] E. Lugscheider, S. Bärwulf, and C. Barimani, Surf. Coat. Technol. **120-121**, 458 (1999).
[39] S. Lu, L. Hou, and F. Gan, Thin Solid Films **353**, 40 (1999).
[40] E. Cazzanelli, G. Mariotto, S. Passerini, W. Smyrl, and A. Gorenstein, Sol. Energy Mater. Sol. Cells **56**, 249 (1999).
[41] E. Lugscheider, O. Knotek, K. Bobzin, and S. Bärwulf, Surf. Coat. Technol. **133-134**, 362 (2000).
[42] Y. Ningyi, L. Jinhua, and L. Chenglu, Appl. Surf. Sci. **191**, 176 (2002).
[43] R. Rajendra Kumar, B. Karunagaran, S. Venkatachalam, D. Mangalaraj, S. Narayandass, and R. Kesavamoorthy, Mater. Lett. **57**, 3820 (2003).
[44] W. Gulbinski, T. Suszko, W. Sienicki, and B. Warcholinski, Wear **254**, 129 (2003).
[45] W. Gulbinski, T. Suszko, and D. Pailharey, Wear **254**, 988 (2003).
[46] G. Silversmit, H. Poelman, and R. De Gryse, Surf. Interface Anal. **36**, 1163 (2004).
[47] C. Ramana, R. Smith, O. Hussain, and C. Julien, J. Vac. Sci. Technol. A **22**, 2453 (2004).

[48] G. Gassner, P. Mayrhofer, K. Kutschej, C. Mitterer, and M. Kathrein, Tribol. Lett. **17**, 751 (2004).
[49] N. Fateh, G. Fontalvo, G. Gassner, and C. Mitterer, Wear **262**, 1152 (2007).
[50] W.-D. Münz, L. Donohue, and P. Hovsepian, Surf. Coat. Technol. **125**, 269 (2000).
[51] C. Constable, J. Yarwood, P. Hovsepian, L. Donohue, D. Lewis, and W.-D. Münz, J. Vac. Sci. Technol. A **18**, 1681 (2000).
[52] P. Mayrhofer, P. Hovsepian, C. Mitterer, and W.-D. Münz, Surf. Coat. Technol. **177-178**, 341 (2004).
[53] Q. Luo, P. Hovsepian, D. Lewis, W.-D. Münz, Y. Kok, J. Cockrem, M. Bolton, and A. Farinotti, Surf. Coat. Technol. **193**, 39 (2005).
[54] Q. Luo, Z. Zhou, W. Rainforth, and P. Hovsepian, Tribol. Lett. **24**, 171 (2006).
[55] Q. Luo and P. Hovsepian, Thin Solid Films **497**, 203 (2006).
[56] Z. Zhou, C. Calvert, W. Rainforth, Q. Luo, L. Chen, and P. Hovsepian, J. Phys.: Conf. Ser. **26**, 95 (2006).
[57] H. Poláková, J. Musil, J. Vlcek, J. Allaart, and C. Mitterer, Thin Solid Films **444**, 189 (2003).
[58] K. Kutschej, P. Mayrhofer, M. Kathrein, P. Polcik, and C. Mitterer, Surf. Coat. Technol. **188-189**, 358 (2004).
[59] K. Kutschej, P. Mayrhofer, M. Kathrein, P. Polcik, and C. Mitterer, Surf. Coat. Technol. **200**, 1731 (2005).
[60] M. Kathrein, C. Michotte, M. Penoy, P. Polcik, and C. Mitterer, Surf. Coat. Technol. **200**, 1867 (2005).
[61] O. Yamaguchi, T. Uegaki, Y. Miyata, and K. Shimizu, J. Am. Ceram. Soc. **70**, C (1987).
[62] R. S. Roth, ed., *Phase Equilibria Diagrams - Phase Diagrams for Ceramists*, vol. XI - Oxides (The American Ceramic Society, Westerville, Ohio, USA, 1995).
[63] Z. Zhou, W. Rainforth, D. Lewis, S. Creasy, J. Forsyth, F. Clegg, A. Ehiasarian, P. Hovespian, and W.-D. Münz, Surf. Coat. Technol. **177-178**, 198 (2004).
[64] D. Lewis, S. Creasey, Z. Zhou, J. Forsyth, A. Ehiasarian, P. Hovsepian, Q. Luo, W. Rainforth, and W.-D. Münz, Surf. Coat. Technol. **177-178**, 252 (2004).
[65] W. M. Rainforth and Z. Zhou, J. Phys.: Conf. Ser. **26**, 89 (2006).

4 Coating synthesis

Today, most of the by physical vapour deposition industrially produced wear protective coatings are synthesised by arc-evaporation since higher deposition rates are commonly achieved as compared to, e.g., sputtering. As arc-evaporation was used within this work, some aspects and characteristics of the method are described in this chapter followed by phenomena regarding the growth of thin films. Arc plasmas normally exhibit high ionisation rates and, hence, emphasis is laid on the influence of ion bombardment on the microstructural evolution. Finally, the parameters applied for the synthesis of the AlCrVN hard coatings are presented.

4.1 Arc-evaporation

Physical vapour deposition (PVD) techniques like sputtering or arc-evaporation utilise electrical discharges which are defined as the passage of electrical current through a normally insulating medium [1]. The electrical conductivity is determined by collision processes, in particular by collisions between electrons and atoms or ions. Inelastic collisions can cause excitation or ionisation of the atoms or ions which in turn leads to the establishment of a self sustained plasma. Electrons, mainly conducting the electrical current in the plasma, originate from the cathode and are emitted due to several processes, e.g. photoelectric process, Auger process, thermionic or field emission. Processes like evaporation, sublimation or sputtering lead to an atomic emission from the cathode.

Arc-discharges are commonly characterised by high currents between ∼30 A and several kA and low discharge voltages ranging from 20–100 V [2]. The voltage depends linearly on the cohesive energy of the cathode material while it generally increases if magnetic fields are present in the vicinity. Two regimes, high-current and low-current, are normally distinguished and as the latter is usually applied in industrial-scale deposition devices like the one used within this work, the description of the arc-evaporation process in the following will focus on this regime.

4.1.1 Cathode spot

Contrary to the glow discharge used in sputter deposition, the current in an arc discharge is concentrated in a small spot of high luminosity which is known by the term cathode spot. The cathode spot with a diameter of ∼1 μm is an ensemble of heated surface area and a dense plasma cloud in front of the surface and is a highly dynamic, self-organised structure [3]. Within this very narrow volume, four different phases are present: solid, liquid, vapour and plasma [1]. After an ignition and explosive time of 1–10 ns, their residence time (or "lifetime") is only 10–100 ns. Spot ignition is most likely to occur at surface asperities as they concentrate the electric field leading to an amplification by a factor of 10^2 to 10^5 [2].

The attracted ions bombard and heat the asperity and due to the combination of high field strength and heat, thermoionisation occurs. Further heating of the asperity by the electron current finally leads to sublimation and explosion while hypersonic jets of highly ionised plasma are generated. Characteristic values for the current density and the plasma density before expansion are usually $\sim 10^{12}$ A/m^2 and $>10^{26}$ m^{-3}, respectively.

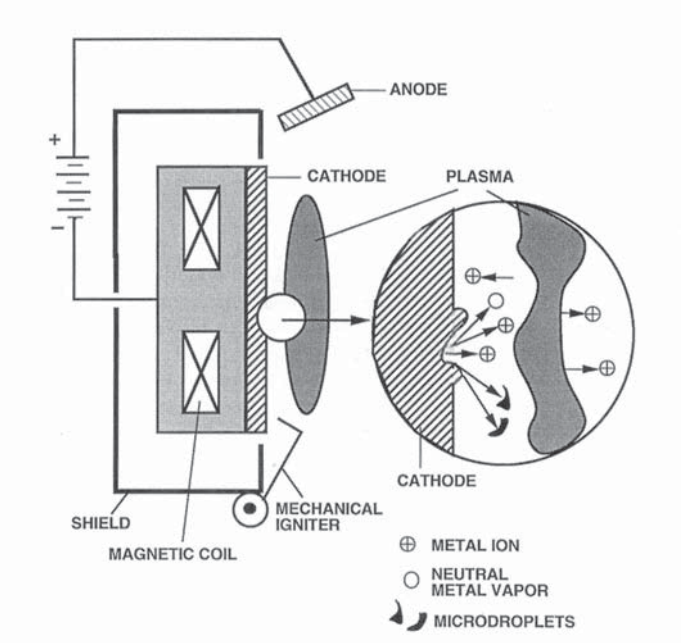

Figure 4.1: Schematic outline of a cathodic arc source and the plasma that is produced by the cathode spot [4, 5].

After recovery of the explosion shockwave the ionisation stops and the plasma expands in a 'frozen' state, i.e., the charge state distribution and the degree of ionisation are preserved [2]. Hence, the emission products from vacuum arc discharges can be characterised by the material dependent properties charge, degree of ionisation and energy. Commonly encountered multiple charged metal ions can reach a charge state of +6 [6] and, hence, the charge state distribution and the mean ion charge state $\overline{Q}$ for the relevant elements Al, V and Cr are shown in Table 4.1. It can be noticed, that the main ionisation state for all three elements is +2, whereas V and Cr reveal slightly higher mean ion charge states. This can be explained by the different ionisation energies. Due to the electron configuration, there is a strong increase of ionisation energy from the +3 to the +4 state for Al (see Table 4.1). This increase is rather moderate for the other two elements, V and Cr. In case a working gas is present, which is normally true for industrial production of state-of-the-art hard coatings where reactive processes are applied, charge exchange with the atoms or molecules from the background gas leads to a reduced mean ion charge state mainly caused by the loss of higher charged states [7]. Nevertheless, the plasma in general can be ionised up to 100% and the ions possess kinetic energies in the range of 20–150 eV while the ion energy is only weakly influenced by the charge state, but by the cohesive energy of the cathode material [2]. The ion energy can be increased by applying a negative bias voltage on the substrates, but care has to be taken since too high bias voltages lead to massive resputtering of the deposited

Table 4.1: Charge state distribution [%, particle fraction] (ionisation energies [eV]) and mean ion charge state $\overline{Q}$ of the metal elements used within this work. The values are according to References [6, 8–10] where an arc current of ∼100 A (without working gas or magnetic fields) was applied for the measurements.

Element	+1	+2	+3	+4	+5	$\overline{Q}$
Al	38 (5.99)	51 (18.83)	11 (28.45)	– (120.0)	– (153.8)	1.73
V	8 (6.75)	71 (14.66)	20 (29.31)	1 (46.71)	– (65.28)	2.14
Cr	10 (6.77)	68 (16.49)	21 (30.96)	1 (49.16)	– (69.46)	2.09

film and no net deposition may be obtained.

As already mentioned, the cathode spot is also an emission source for electrons with a rather low energy ranging from 2–4 eV. These electrons can excite the working gas, e.g. N_2 or C_2H_2, while an appropriate magnetic field around the source leads to an increase of the electron energy that, in turn, might be sufficient to dissociate and ionise the background gas molecules [1].

4.1.2 Arc source design and magnetic fields

First, basic considerations in the design of arc sources will be presented, whereas details about the impact of magnetic fields on the control of the arc discharge are discussed subsequently. There are a few important requirements which an arc source has to fulfil: (1) confinement of the arc to the appropriate cathode surface, (2) dissipation of the heat generated by the arc spot and (3) the anode must carry the arc current. According to Reference [1] ∼1/3 of the total arc supply power is converted into heat and, therefore, it is common to use water cooling systems mounted on the back of the cathode in industrial deposition devices. In such devices the chamber wall normally serves as anode. However, the confinement of the arc needs to be addressed first. In the absence of a magnetic field, the cathode spot moves randomly over the cathode surface. If a magnetic field $\mathbf{B}$ is present in the vicinity of the cathode, with the current vector $\mathbf{I}$ normal to the surface, the cathode spot moves in the direction of $-(\mathbf{I} \times \mathbf{B})$ [11]. This phenomenon is known as retrograde motion while the velocity of the spot is proportional to the aforementioned product. Other factors that influence the spot motion are the background gas pressure, the cathode temperature and, to a limited extent, the cathode material.

The actual control of the cathode spot motion is due to magnetic fields or the use of insulators or electrically isolated shields. The latter restricts the formation of arc spots to the cathode surface and contamination due to evaporation of other machine parts or even complete destruction of the device are avoided. In addition, magnetic fields can support the limitation of the spot motion to a certain zone, but they alter the plasma in dependence on their strength and configuration. As shown in Figure 4.2, magnetic fields that act on the cathode spot can be divided into two groups: arched magnetic field and through-field configurations [12, 13]. The fields are generated by coils or permanent magnets that are

placed behind the cathode while the specific arrangement is optimised with regard to the cathode material. Here, special attention is paid to the material utilisation factor, that can be distinctly reduced if a very narrow race-track path of the cathode spot, due to a circular retrograde motion, occurs resulting in cathode erosion from a limited area only [11]. Further, magnetic fields influence the charge state distribution of the metal species while commonly higher mean ion charge states are observed [6, 9, 10]. However, this effect is counteracted by the charge transfer to the working gas, particularly if the plasma is confined near the cathode which is normally the case for arched magnetic fields revealing a comparable configuration as magnetrons used in sputter deposition [2].

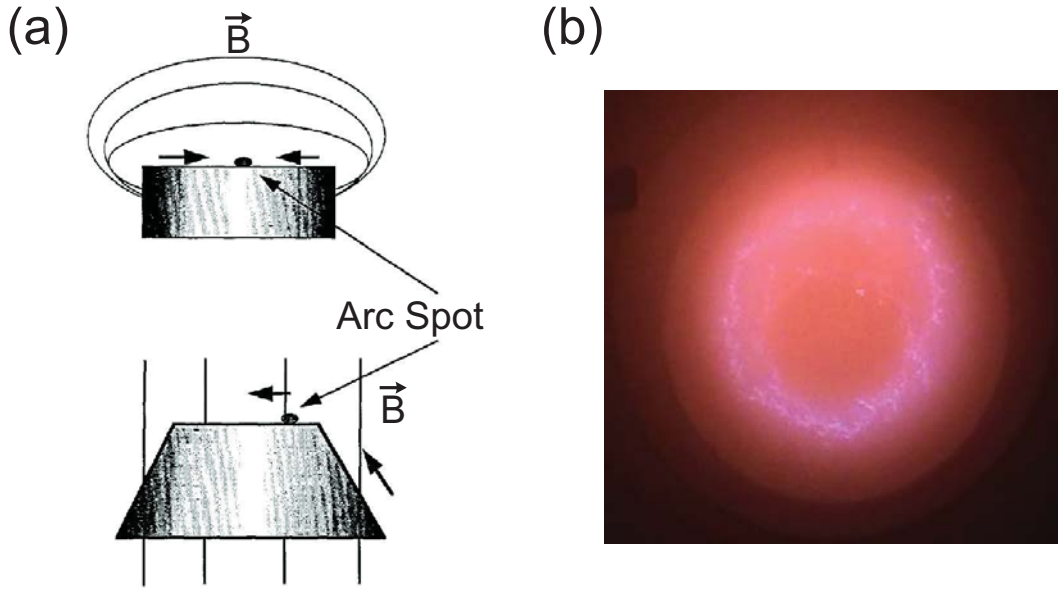

Figure 4.2: (a) Illustration of possible internal magnetic field configurations: arched field (upper part) and through-field configuration (lower part) [14]. (b) Cathode spot on AlCrV target moving along the race track as forced by the used magnetic field configuration.

Other magnetic fields are employed for handling the plasma stream emitted by the arc cathode. These fields, in general, can be used to accelerate the plasma, enhance the synthesis of compound films, improve the adhesion or filter droplets and neutral species. The latter case is of special interest for many fields where thin films are applied since the emission of droplets or macroparticles by arc-evaporation is a major issue. The origin of droplets and strategies in order to suppress or filter them will be presented in the following.

4.1.3 Macroparticles

In a conventional arc-evaporation source, a numerous amount of droplets, also known by the term macroparticles, are produced. As shown in Figure 4.1, droplets are created at the outer margins of the cathode spot and consist of target material that melted but did not sublimate or evaporate [2]. Hence, their ejection is most pronounced at small angles

to the cathode surface and depends strongly on the cathode material. In general, higher cathode temperatures favour the formation of droplets, whereas for materials with high melting points a reduced number of droplets was observed. However, macroparticles with sizes in the range of 0.01–10 μm make up a significant fraction of the target erosion as well as the total deposition rate and surfaces of arc-evaporated films have, therefore, a matt appearance. Even though, hard coatings that contain droplets still show good cutting performances, their protective properties are weakened as the incorporation of droplets leads to the formation of growth defects that extent through the remainder of the coating [15]. Underdense or porous areas in the vicinity of these growth defects can act as fast diffusion channels causing corrosion of the underlying substrate while the mechanical properties are generally compromised [1, 16, 17].

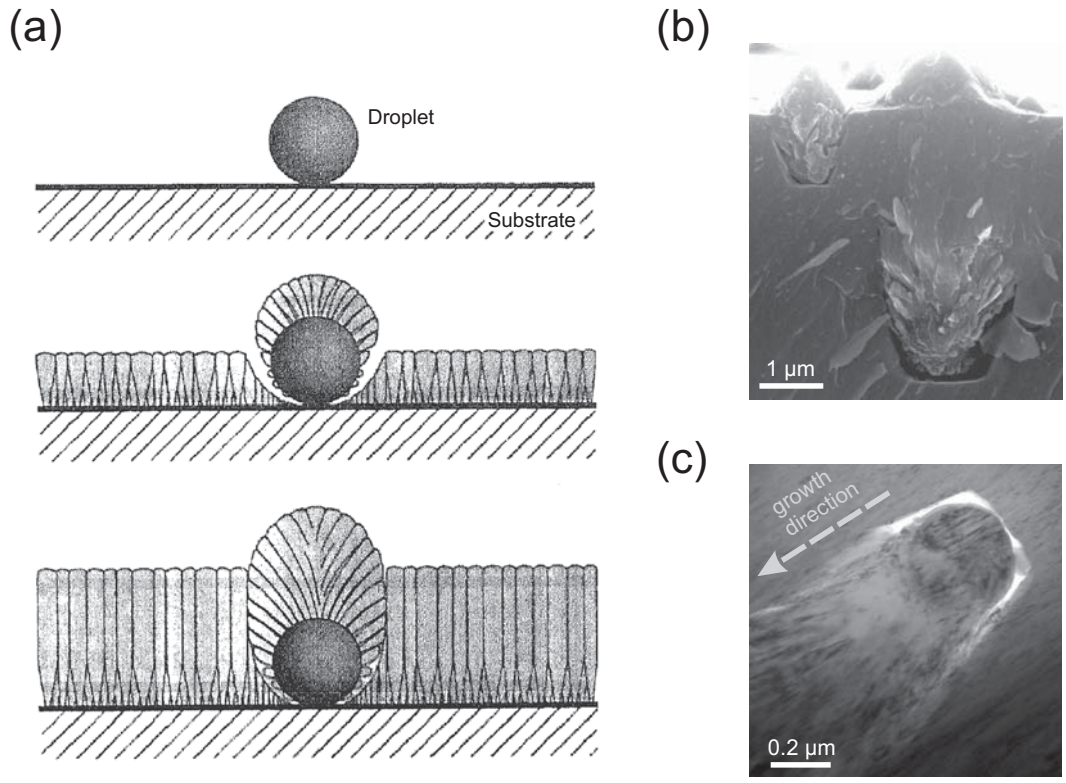

Figure 4.3: (a) Schematic illustration of the formation of a growth defect that results from an attached droplet [15]. SEM (b) and TEM (c) cross-sectional images of droplets and growth defects as observed in AlCrVN coatings.

Several strategies were developed and applied in order to reduce or completely avoid the incorporation of macroparticles in the deposited films. A simple way is to increase the partial pressure of the reactive gas during deposition. It is well known, that in the presence of a working gas, e.g. N_2, a thin compound layer can form on the cathode surface. If this compound presents a higher melting point, e.g. 2950°C for TiN as compared to 1670°C for pure Ti [18], then the number and the maximum size of the emitted droplets

can be reduced [19, 20]. In a similar way, steering of the cathode spot by magnetic fields influences the formation of macroparticles. Due to the increased velocity of the cathode spot motion, the emission of large droplets is avoided since melting of extended areas is suppressed [21, 22]. However, some applications require a complete removal which can be accomplished by electromagnetic filtering of the arc plasma prior to deposition. Although filter techniques increase the technological complexity significantly, high-quality films with low roughness values are obtained. A very common filter design is the quarter torus which allows for placing the substrates out of sight from the cathode [2]. Here, the plasma is forced through a 90° bend by strong magnetic fields, while neutral atoms and droplets propagate unaffected. In addition, droplets reaching the substrates by bouncing from the chamber or filter walls, especially when quickly solidifying materials are used, can be suppressed by mounting baffles in order to block the droplet pathways. On the other hand, the removal of neutral particles leads to extremely high ion-to-neutral ratios and the deposited coatings develop extreme residual stresses [23]. Therefore, the usage of arc filters is commonly accompanied by methods of stress control.

4.2 Thin film growth

In the absence of macroparticles or droplets undisturbed thin film growth can occur as it was investigated by many researchers. Since detailed discussions of mechanisms involved in the growth process of thin films exist in several textbooks and publications [4, 24–27], only a short summary is presented here.

4.2.1 Nucleation

When particles, atoms or ions, arrive at the substrate, it is the appearance of the substrate surface that strongly influences whether the particles adhere or not. Normally, most particles remain on the substrate surface for a certain time and if they encounter a stable lattice site during their diffusion time, nucleation starts (see Figure 4.4). Thus, the nucleation rate is determined by the adsorption rate of the impinging particles while other parameters such as the substrate temperature and deposition rate influence the nucleation as they alter the adparticle diffusion [4]. Once, the radius of a metastable cluster exceeds the critical value, i.e., the change in free energy starts to decrease, a stable nucleus of adparticles is formed and thin film growth commences [27].

As shown in Figure 4.5, three different growth modes can be distinguished, (1) 3-D island or Volmer-Weber growth, (2) 2-D layer-by-layer or Frank-van der Merwe growth and (3) Stranski-Krastanov growth which is a combination of the first two. In case the adatoms are stronger bonded to each other than to the substrate, they form clusters and island and a continuous film covering the whole substrate is produced due to coalescence of the growing islands [25]. On the other hand, if the binding energy between the adatoms is equal or smaller than between adatom and substrate, then layer-by-layer growth appears. Here, a second monolayer will only occur after the first monolayer has covered the whole surface. These two growth modes can as well be distinguished in terms of surface energy. Higher values of the film surface energy as compared to the substrate lead to the agglomeration of atoms in islands while large areas of the substrate surface remain unaffected. This atomic

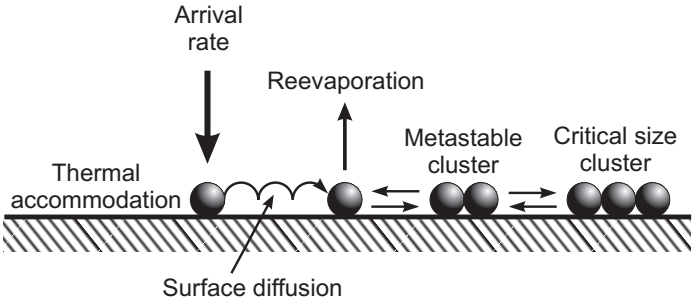

Figure 4.4: Schematic illustration of the nucleation process [25].

distribution reveals a minimum in surface energy for the given case. On the contrary, if the surface energy of the film is lower than the substrate, an energy minimum is reached when the surface is covered with one monolayer of adatoms. Subsequently, the second and more monolayers can grow on the already deposited adatoms. In case this growth procedure is disturbed by some factor and a transition to 3-D island growth occurs, the growth mode often referred to as Stranski-Krastanov is present. Typically, the transition from layer-by-layer to island growth appears after 5–6 monolayers, but the mechanisms that drive this transition are not yet completely understood [4]. One reason might be the release of elastic energy that results from the lattice mismatch between substrate and thin film [25].

However, besides the diffusion and incorporation of single adatoms, the growth of the formed nuclei is characterised by coalescence [4]. One occurring process of coalescence is Ostwald ripening where larger islands grow at the expense of smaller ones resulting in a reduction of surface energy. In case the involved islands are in contact, the coalescence is described by a mechanism termed as sintering. First, a neck that connects the islands is formed, whereas the neck growth due to diffusion is, again, driven by the tendency to reduce the surface energy. At higher temperatures and, in this case, higher diffusivity of the adatoms, complete islands or crystallites can migrate on the surface in random motion. A collision between two islands can result in the mergence of these islands and the formation of a new one.

4.2.2 Microstructure - Structure zone models

The evolution of the thin film microstructure passes from the nucleation in the beginning to the coalescence stage through several hundreds of nm up to μm until it reaches a steady-state configuration [25]. Basic processes of film condensation are given by shadowing, surface diffusion, bulk diffusion and desorption. While the latter three processes are energy dependent and, hence, scale with the melting point of the deposited material, shadowing is influenced by the surface roughness and the incident angle of the arriving particles [4]. In case one of these processes dominates the thin film growth at a certain substrate temperature, a specific film morphology is obtained. On this basis, different structure zone models have been derived in order to represent the relation between deposition parameters and the resulting film structure. The first model for evaporated films was introduced by Movchan and Demchishin who distinguished 3 structural zones which were classified by the homologous temperature,

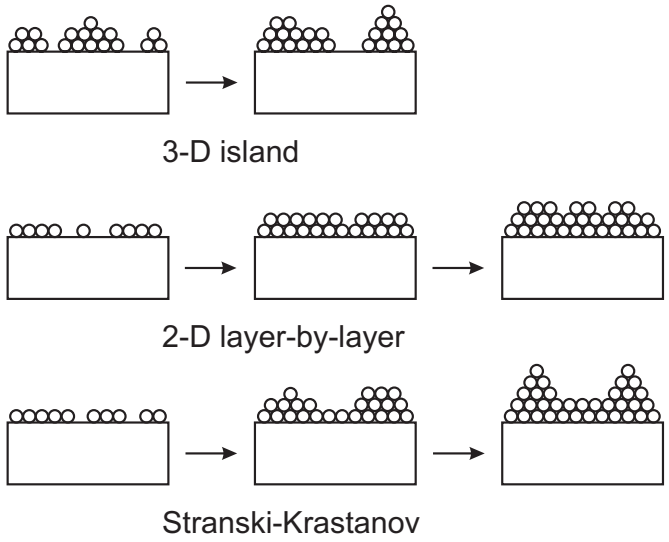

Figure 4.5: Possible thin-film growth modes [4].

i.e., the ratio between substrate temperature and melting point of the deposited material [28]. A similar model for sputtered films was derived by Thornton, whereas additionally to temperature the inert gas pressure was introduced as a variable [29–31]. Messier et al. replaced the gas pressure by the substrate bias voltage which varies in an inverse manner and also included the effects of ion bombardment during film growth [32]. Other structure zone models can be found in the References [24, 26, 33–37]. At this point it should be noted that the zone III present in many models and characterised by equiaxed three dimensional grains as a result of periodical renucleation during film growth, only exists in the presence of impurities. Further, Barna and Adamik also indicated that this structure type is not primarily associated with high temperatures, but can develop at every substrate temperature with different grain sizes [34].

In the following the structure zone model as published by Mahieu et al. will be presented in detail serving as an example (see Figure 4.6). Here, the use of quantitative temperature values is avoided since the diffusion processes and structure formation phenomena are not only influenced by the substrate temperature, but by the total energy flux to the growing surface.

Zone Ia At low temperatures and low particle energies, the adatoms have little or no mobility which does not allow for overcoming the diffusion barrier. Therefore, a so-called hit-and-stick growth or "ballistic" deposition will be obtained where the resulting structure only depends on the incoming direction of the particles. A relation between the angles α representing the inclination of the substrate with respect to the particle flux and β which describes the tilt of the columns (see Figure 4.6) is given by the tangent rule: $\tan\alpha = 2\tan\beta$. This equation is an approximation derived from experimental results and its applicability is limited to a narrow range of α and β. However, the obtained amorphous-like structure consisting of columns that are separated by voids is a result of roughening and self-shadowing. A similar structure can be found at higher temperatures with high deposition rates. Here, the adatoms are "buried" by the high flux of incoming particles and diffusion processes are

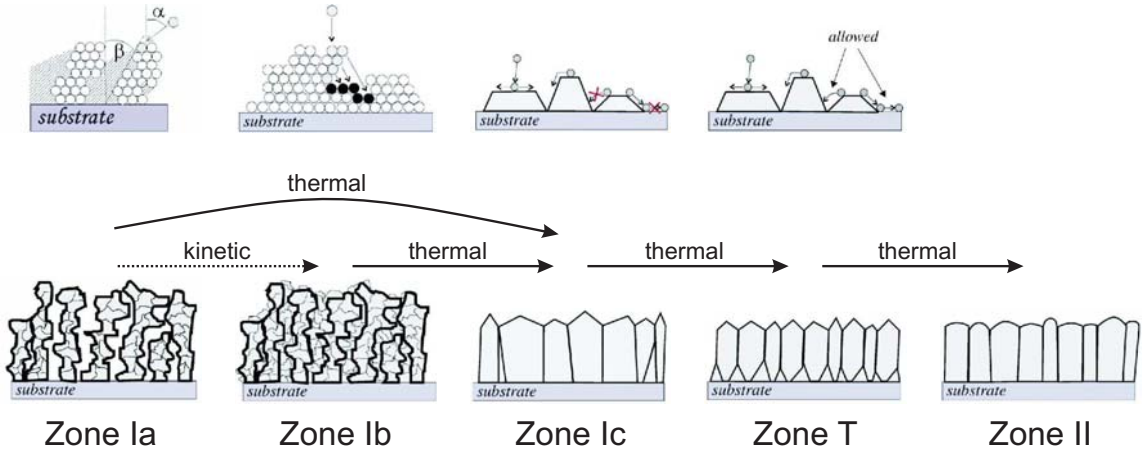

Figure 4.6: Overview of the structure zone model as presented by Mahieu [38]. In the upper row, characteristic processes for each structural zone are depicted while the transition energy and schematic structure are illustrated in the lower row.

suppressed. In general, thin films of this structure zone have low density and no specific crystallographic orientation.

Zone Ib In case of unaltered deposition conditions as compared to zone Ia, but continuous bombardment of the growing film with energetic particles, a slightly different film structure is observed. The voids between the columns will be filled with particles and a dense, amorphous-like structure without preferred crystallographic orientation is obtained. Energetic particles can be accelerated ions or fast neutrals that deliver additional kinetic energy to the film. It should be noted, that an increase in temperature does not lead to a transition to zone Ib.

Zone Ic Depositions at higher temperatures increase the mobility of the adparticles and nucleation and island formation can take place. As the adatoms are able to overcome the diffusion barrier, the grains are faceted with the planes of the lowest crystallographic growth rate. On the other hand, there is no diffusion of atoms from grain to grain and, thus, no interaction or competition between neighbouring grains occurs. This leads to the formation of columns that are separated by grain boundaries, whereas voids are filled due to the adatom mobility. The growth competition is dominated by shadowing and no preferential orientation is obtained.

Zone T A further increase in temperature enables the diffusion of adparticles from grain to grain allowing the grains to grow according to their crystal habit which in turn leads to the occurrence of faceting. However, recrystallisation or restructuring is still not possible and, therefore, the competitive growth of the grains follows an evolutionary way, i.e., the grains with the geometrically fastest growing direction perpendicular to the substrate will overgrow

the other grains. As a result, V-shaped grains develop and, at higher film thicknesses, the columns have faceted tops.

Zone II When recrystallisation and restructuring become available at even higher temperatures, the incorporation of islands in other islands by ripening, cluster diffusion or grain boundary migration can occur. In this growth regime, no evolutionary V-shaped overgrowth is observed, but a columnar structure with approximately straight columns. As the film aims for the thermodynamically most stable situation, the columns are oriented with the plane of the lowest surface energy parallel to the surface. Shadowing effects are negligible and no inclination of the columns for oblique substrates is obtained.

4.2.3 Ion bombardment

As already mentioned in the discussion of the structure zone models, accelerated ions or fast neutrals can have an influence on the formation of a specific film structure. Further, taking into account the high ionisation rate of the common arc plasma, it can be concluded that ion bombardment during thin film growth by arc-evaporation has a strong effect. Although the effects of ion irradiation were mainly studied by using magnetron sputtering, the basic phenomena are generally valid. The main interest in using energetic particle bombardment lies within modifying the morphology, microstructure, stress state and the physical properties of polycrystalline films [25]. That can be realised as ion bombardment increases the nucleation rate and film density, decreases the average grain size, inhibits the formation of columnar structures with rough surfaces and affects the defect density and preferred orientation [39]. Even a low flux of ions with rather low energies can significantly alter the growth of thin films. When depositing at low temperatures, porous structures according to zone Ia are obtained, whereas a moderate irradiation with energetic particles enhances the adatom mobility leading to individual, dense columns. On the other hand, the impact of ions with very high energies besides producing fully dense films causes non-negligible residual damages which is the key issue in applying ion irradiation. Further, these high ion energies result in high defect densities, inert gas incorporation and very high compressive stress which in turn might lead to coating spalling [39]. The situation normally encountered in arc plasmas is described by rather moderate ion energies, but high ion fluxes due to the high ionisation rate. In this case, the transferred energy is not sufficient to cause bulk lattice displacements and columnar, but fully dense structures due to the occurring competitive growth are obtained. A convenient way to study the ion impact during thin film growth is due to Monte Carlo or molecular dynamics simulations [40–42]. In Figure 4.7, the effects of an impinging ion on the distribution of the already deposited atoms are clearly observable. The open void on the right-hand side gets filled with atoms due to a collision cascade while the already established void in the center shrinks significantly in size. In general, a higher densification is obtained for higher kinetic energies of the impact ions [4], but a growth regime described by the above mentioned disadvantages should be avoided. However, ion irradiation can also stabilise the growth of metastable phases due to, e.g., ion-assisted chemistry [25]. Low-energy ions provide for collisional mixing at the growth front which beneficially influences the formation of metastable phases and even compounds with compositions within miscibility gaps can be grown. On the contrary, high-energy ions enhancing bulk diffusion may cause undesired

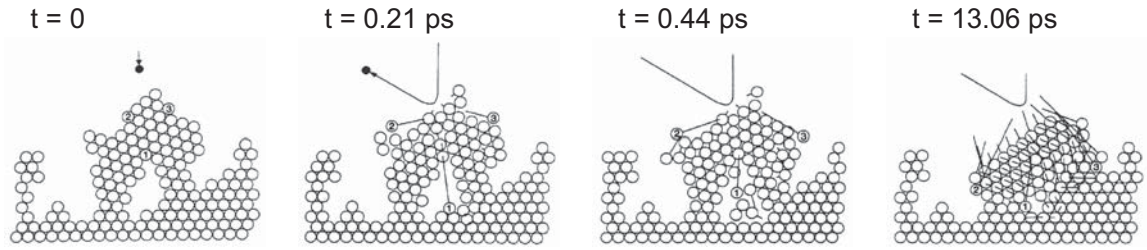

Figure 4.7: Collision sequence resulting from the impact of an ion on a porous film structure as obtained by molecular dynamics simulations [41].

phase separations.

In summary, the high ion to neutral ratio as usually present in arc plasmas allows for a high degree of control and manipulation of the formation of specific thin film structures. As shown in Publication III and V, applying higher energetic growth conditions during the synthesis of AlCrVN hard coatings alters the crystal structure and the mechanical properties. In Section 3.3, it was mentioned that with increasing the bias voltage during deposition the formation of the fcc-phase is stabilised and a single-phase fcc-AlCrVN coating is obtained at –150 V. This crystal structure evolution is a result of enhanced ion impact on the growing films, realised by establishing an increased bias voltage which in turn leads to an acceleration of the ions from the plasma towards the substrate holder. Further consequences of the high-energy growth conditions are higher values of the compressive stress and the hardness. A more detailed discussion about the interplay between structure and mechanical properties is included in Publication III, whereas the effects on the tribological behaviour are treated in Publication V.

4.3 Synthesis of V alloyed AlCrN hard coatings

Within this work, the deposition of V alloyed AlCrN hard coatings was done in an industrial-scale arc-evaporation system Oerlikon Balzers RCS, schematically illustrated in Figure 4.8. Four of the available six arc sources were equipped with powder-metallurgically produced targets and used for deposition. The compositions and the applied parameters are given in Table 4.2. An average mass loss of ∼0.1 g/min for each target was obtained while a voltage of ∼20 V was necessary to maintain the arc-discharge. The substrates were mounted on a carousel which allows for a two-fold rotation during deposition. An additional arc-discharge in the chamber center was used for heating and ion etching of the substrates prior to deposition while the plasma consisted of pure Ar gas. The deposition rate was ∼50 nm/min and the obtained coatings were well adherent and showed a dark greyish colour. Their nitrogen concentration is ∼50% and the metal ratio roughly mirrors the respective target composition independently from the applied deposition parameters. Only a slight aluminium deficiency of 2–3% was typically observed. Further, as mentioned in the previous section, the addition of V results in the formation of a dual-phase structure if the coatings are deposited at low bias voltages (–40 to –100 V), whereas no preferential incorporation of V into

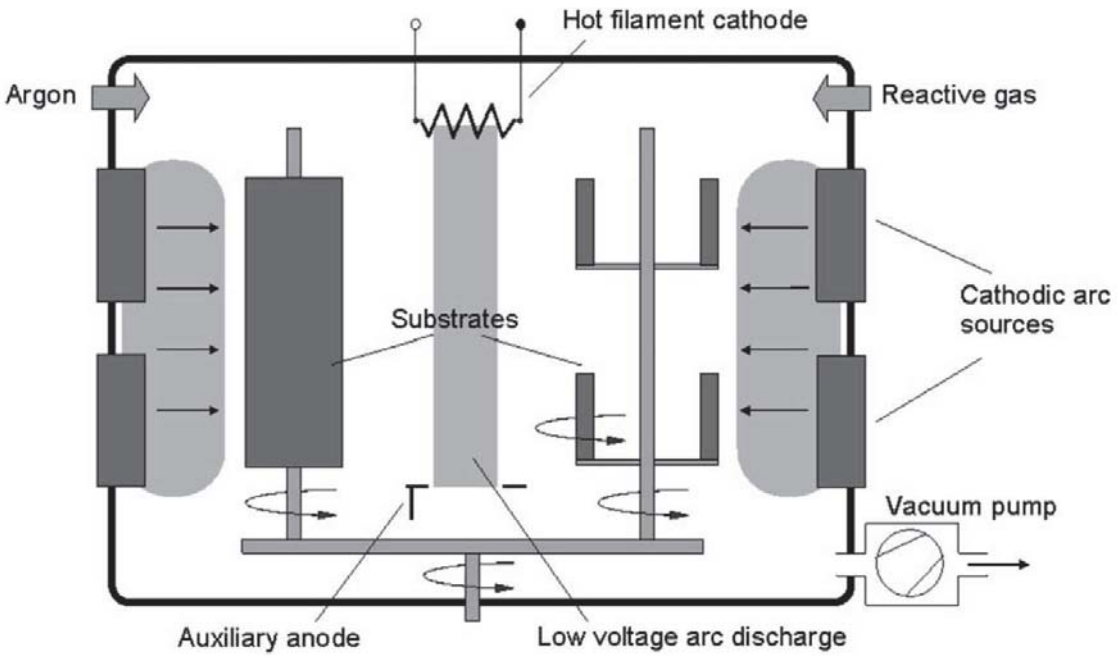

Figure 4.8: Schematic illustration of the Oerlikon Balzers RCS used for the coating deposition [43].

Table 4.2: Overview of the applied deposition parameters.

Deposition parameters	
Targets	$Al_{0.70}Cr_{0.30}$
	$Al_{0.70}Cr_{0.20}V_{0.10}$
	$Al_{0.70}Cr_{0.15}V_{0.15}$
	$Al_{0.70}Cr_{0.10}V_{0.20}$
	$Al_{0.70}Cr_{0.05}V_{0.25}$
	$Al_{0.70}V_{0.30}$
Arc current	140 A (4 sources)
N_2 gas pressure	3.5 Pa
Temperature	500°C
Bias voltage	–40 V, –70 V, –100 V, –150 V
Magnet system	Mag 10
Base pressure	4×10^{-3} Pa

either phase occurs. More details can be found in Publication II containing crystallographic data in dependence on the vanadium content, whereas Publication III reports on structural changes due to higher bias voltages.

Prior to the above mentioned depositions, a series of $Al_xCr_{1-x}N$ coatings ranging from pure CrN to pure AlN was synthesised using similar parameters. Here, all six available arc sources were employed while the substrate bias voltage was set to −40 V. In case of pure AlN, a pulsed bias voltage was applied due to its insulating character. The main focus within this series was on studying the tribological behaviour as shown in Publication I. Details regarding the crystal structure can be found in Reference [44] where a comparable series of coatings was investigated.

References

[1] R. L. Boxman, D. M. Sanders, and P. J. Martin, eds., *Handbook of Vacuum Arc Science and Technology: Fundamentals and Applications* (Noyes Publications, New Jersey, 1995).

[2] U. Helmersson, M. Lattemann, J. Bohlmark, A. Ehiasarian, and J. Gudmundsson, Thin Solid Films **513**, 1 (2006).

[3] A. Anders, E. Oks, G. Yushkov, K. Savkin, I. Brown, and A. Nikolaev, IEEE Trans. Plasma Sci. **33**, 1532 (2005).

[4] M. Ohring, *Materials Science of Thin Films - Deposition and Structure* (Academic Press, San Diego, 2002), 2nd ed.

[5] J. Vossen and W. Kern, eds., *Thin Film Processes II* (Academic Press, Boston, 1991).

[6] A. Anders, Phys. Rev. E: Stat. Phys., Plasmas, Fluids, Relat. Interdiscip. Topics **55**, 969 (1997).

[7] P. Martin, D. McKenzie, R. Netterfield, P. Swift, S. Filipczuk, K. Müller, C. Pacey, and B. James, Thin Solid Films **153**, 91 (1987).

[8] I. G. Brown, Rev. Sci. Instrum. **65**, 3061 (1994).

[9] E. M. Oks, I. G. Brown, M. R. Dickinson, R. A. MacGill, H. Emig, P. Spadtke, and B. H. Wolf, Appl. Phys. Lett. **67**, 200 (1995).

[10] E. Oks, A. Anders, I. Brown, M. Dickinson, and R. MacGill, IEEE Trans. Plasma Sci. **24**, 1174 (1996).

[11] R. Boxman, I. Beilis, E. Gidalevich, and V. Zhitomirsky, IEEE Trans. Plasma Sci. **33**, 1618 (2005).

[12] D. Karpov, Surf. Coat. Technol. **96**, 22 (1997).

[13] A. Ehiasarian, P. Hovsepian, R. New, and J. Valter, J. Phys. D: Appl. Phys. **37**, 2101 (2004).

[14] B. Coll and D. Sanders, Surf. Coat. Technol. **81**, 42 (1996).

[15] I. Petrov, P. Losbichler, D. Bergstrom, J. Greene, W.-D. Münz, T. Hurkmans, and T. Trinh, Thin Solid Films **302**, 179 (1997).

[16] H. Ljungcrantz, L. Hultman, J.-E. Sundgren, G. Hakansson, and L. Karlsson, Surf. Coat. Technol. **63**, 123 (1994).

[17] A. Hörling, L. Hultman, M. Odén, J. Sjölén, and L. Karlsson, J. Vac. Sci. Technol. A **20**, 1815 (2002).

[18] D. R. Lide, ed., *CRC Handbook of Chemistry and Physics* (CRC Press, 2004), 85th ed.

[19] A. Baouchi and A. J. Perry, Surf. Coat. Technol. **49**, 253 (1991).
[20] S. Harris, E. Doyle, Y.-C. Wong, P. Munroe, J. Cairney, and J. Long, Surf. Coat. Technol. **183**, 283 (2004).
[21] P. Swift, J. Phys. D: Appl. Phys. **29**, 2025 (1996).
[22] A. Anders, Surf. Coat. Technol. **120-121**, 319 (1999).
[23] P. Martin, A. Bendavid, T. Kinder, and L. Wielunski, Surf. Coat. Technol. **86-87**, 271 (1996).
[24] P. Barna, *Crystal Growth and Recrystallization during Structure Evolution of Thin Films*, in Diagnostics and Applications of Thin Films (eds. L. Eckertová, T. Ruzicka), (Institute of Physics Publishing, 1992).
[25] J. Greene, *Low-Energy Ion/Surface Interactions during Crystal Growth from the Vapor Phase*, in Handbook of Crystal Growth, Vol. 1 (ed. D.T.J. Hurle), (Elsevier Science Publishers, 1993).
[26] Y. Pauleau and P. B. Barna, eds., *Protective Coatings and Thin Films* (Kluwer Academic Publishers, Dordrecht, 1997).
[27] J. Greene, *Thin Film Nucleation, Growth and Microstructure Evolution* (AVS course at the ICMCTF, San Diego, 2006).
[28] B. Movchan and A. Demchishin, Physics of Metals and Metallography **28**, 83 (1969).
[29] J. A. Thornton, J. Vac. Sci. Technol. **11**, 666 (1974).
[30] J. A. Thornton, Annu. Rev. Mater. Sci. **7**, 239 (1977).
[31] J. A. Thornton, J. Vac. Sci. Technol. A **4**, 3059 (1986).
[32] R. Messier, A. P. Giri, and R. A. Roy, J. Vac. Sci. Technol. A **2**, 500 (1984).
[33] H. T. G. Hentzell, C. R. M. Grovenor, and D. A. Smith, J. Vac. Sci. Technol. A **2**, 218 (1984).
[34] P. Barna and M. Adamik, Thin Solid Films **317**, 27 (1998).
[35] P. Kelly and R. Arnell, Vacuum **56**, 159 (2000).
[36] Y. Kajikawa, S. Noda, and H. Komiyama, J. Vac. Sci. Technol. A **21**, 1943 (2003).
[37] E. Mirica, G. Kowach, and H. Du, Cryst. Growth Des. **4**, 157 (2004).
[38] S. Mahieu, P. Ghekiere, D. Depla, and R. De Gryse, Thin Solid Films **515**, 1229 (2006).
[39] I. Petrov, P. Barna, L. Hultman, and J. Greene, J. Vac. Sci. Technol. A **21**, 117 (2003).
[40] K.-H. Müller, J. Vac. Sci. Technol. A **4**, 184 (1986).
[41] K.-H. Müller, Phys. Rev. B **35**, 7906 (1987).
[42] K.-H. Müller, Surface Science **184**, L375 (1987).
[43] W. Kalss, A. Reiter, V. Derflinger, C. Gey, and J. Endrino, Int. J. Refract. Met. Hard Mater. **24**, 399 (2006).
[44] A. Reiter, V. Derflinger, B. Hanselmann, T. Bachmann, and B. Sartory, Surf. Coat. Technol. **200**, 2114 (2005).

5 Coating characterisation

Since several methods were applied in order to study the properties and phenomena of interest regarding AlCrVN coatings, they are explained briefly in this chapter. Some selected methods are described more detailed in conjunction with the obtained results.

Electron probe microanalysis (EPMA) was used to determine the chemical composition of the synthesised coatings by means of wavelength-dispersive X-ray (WDX) spectroscopy. X-ray radiation is induced upon bombarding the sample with a focused electron beam and provides for quantification by comparing the signal of the unknown composition with pure element or binary compound standards [1].

X-ray diffraction (XRD) reveals information as to the crystal structure of the investigated material. According to Bragg's law, a diffraction pattern is obtained that is used to identify crystalline phases, whereas Rietveld refinement of the recorded pattern allows for the quantification of the phase fractions as well as deriving details about crystallite size and residual stress [2].

Scanning electron microscopy (SEM) provides high magnification images and compositional maps by scanning a focused electron beam over the sample [1]. The recorded signal can be due to secondary electrons, internal currents, photon emission, etc. Within this work SEM was mainly used to study fracture cross-sections and the surface morphology, especially after performing tribological tests.

Indentation tests according to Oliver and Pharr [3] can be used to obtain values of the coating hardness and Young's modulus. More details concerning the use of this method can be found in References [4] and [5].

Biaxial stress-temperature measurements by the cantilever beam bending technique reveal values of the residual coating stress in correlation with the temperature. The used method is described in Reference [6], whereas more information regarding the stress in thin films is inclosed in Reference [7].

5.1 Ball-on-disc tests and optical profilometry

A general description about aspects of tribology is included in Chapter 2 while the method applied for obtaining friction and wear data is due to ball-on-disc tests where the counterpart is pressed on the rotating sample. In Figure 5.1a the principle of ball-on-disc tests and typical parameters used within this work are shown. The coatings were deposited on HSS coupons

(AISI M2, DIN 1.3343) with a diameter of 30 mm and a thickness of 10 mm, whereas alumina balls with a diameter of 6 mm were chosen as counterpart because of their chemical inertness at high temperatures. These balls were pressed on the surface during the total sliding distance of 300 or 1000 m causing wear of the coating and the counterpart itself. An example of the recorded COF in dependence on the sliding distance is shown in Figure 5.1b where the beneficial effect of the V incorporation can be seen as the COF at 700°C is reduced significantly.

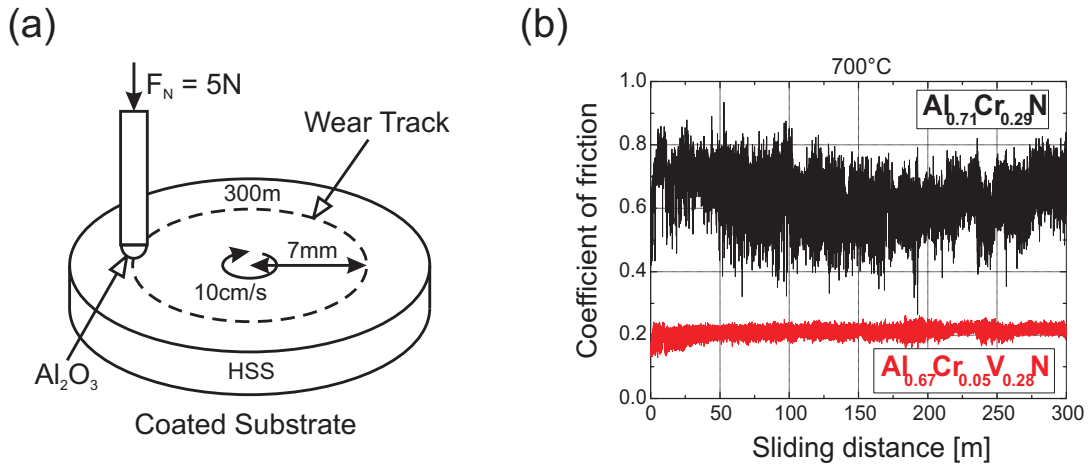

Figure 5.1: (a) Schematic illustration of a ball-on-disc test including typical parameters used within this work. (b) Recorded coefficient of friction vs. sliding distance.

Subsequent to the tribological tests, the wear tracks were investigated with an optical profilometer revealing information about the depth and the volume of the displaced material. The latter was used to calculate the wear coefficient according to the equation given in Section 2.1. Publication I contains a detailed analysis of the tribological behaviour of AlCrN coatings which serves as an example.

5.2 Raman spectroscopy

Raman spectroscopy, first discovered by Krishna and Raman in 1928, can be understood as inelastic scattering of photons with molecules [8]. When a monochromatic light beam impinges on a sample, the electric field interacts with the electron clouds of the present atoms. The resulting excited state of the atom is not necessarily a real quantum state, but can be considered a short lived distortion of the electron cloud [9]. Re-emission of the stored energy is mainly due to elastic Rayleigh scattering in all directions leading to a signal in the recorded spectrum with the frequency of the incident light. Electron clouds, however, are also perturbed by molecule or lattice vibration. In case of coupling between both, optical and vibrational, oscillations, Raman scattering occurs. An energy transfer from the impinging photon to the material causing the creation of a new lattice vibration results in signals in the spectrum at lower frequencies, the Stokes scattering peaks. On the contrary, the photon can also gain the energy of an already existing vibration leading to anti-Stokes peaks at

higher frequencies than the Rayleigh line or incident light. Although Stokes and anti-Stokes peaks are symmetrically positioned relative to the Rayleigh line, the intensities of the single peaks may vary. Further, as anti-Stokes scattering only occurs in the presence of thermally-activated lattice vibrations, it strongly depends on the sample temperature, whereas Stokes scattering is only weakly influenced by the temperature.

Recorded spectra are commonly presented in terms of the difference to the frequency or wave number of the incident light beam. This so-called Raman shift is a direct measure of the vibrational frequencies. Similar results are obtained by infrared absorption, but the mechanisms are different. Especially the difference in intensity between both effects has given preference to infrared absorption for a long time. Rayleigh scattering is in the order of 10^{-3} to 10^{-5} of the intensity of the exciting light, whereas Raman scattering is 10^{-3} to 10^{-6} of the Rayleigh line [1]. In summary, the probability for the Raman effect to occur is by a factor of $\sim 10^{-10}$ lower as compared to, e.g., mid-infrared absorption [9]. Only the development of Fourier transform Raman spectroscopy, charge-couple devices (CCD) and the introduction of computers and near-infrared lasers gave rise to the use of Raman spectroscopy in routine chemical analysis.

Nowadays, several measurement setups due to further technological advances are possible. Combining an optical microscope with a laser providing monochromatic light of high intensity offers Raman investigations with equal resolutions as obtained in optical microscopy. Here, the sample is placed on the microscope stage and the measurement is done in 180° backscattering geometry. Such a system was used within this work while the emission lines from a He-Ne laser (632.8 nm) or an Ar^+ laser (514.5 or 488 nm) could be chosen for spectra excitation.

A rather straightforward way of using Raman spectroscopy is the identification of an unknown material via fingerprints. By comparing the recorded spectrum with a database containing reference spectra, the unknown material of the investigated sample can be identified. Raman spectroscopy was applied for studying the wear tracks after tribological testing in Publication I, II and V. The knowledge of the compounds present after testing reveals information whether the coating withstood the test or not and, more importantly, if lubricious oxides for reducing the friction were formed. In Figure 5.2 two sample spectra taken in the wear track after tribological tests at 700°C are shown. A comparison with standard spectra reveals the presence of Fe oxides in the wear track of the coating on the left-hand side. Fe originates from the underlying substrate signifying that the coating was worn through during the performed test. A different situation is obtained for the coating on the right-hand side where the Raman spectra evidences the presence of V_2O_5. As described in Sections 3.2 and 3.3, this oxide offers lubricious effects and a COF of 0.2 could be recorded. The apparent mismatch in the wave number range of 800–1000 cm^{-1} was attributed to the presence of $AlVO_4$ [10–12]. A more detailed study of the oxide formation on AlCrVN coatings during annealing in ambient air using also Raman spectroscopy is presented in Publication IV.

So far, Raman spectra were only recorded from a few well separated points. Information about the lateral distribution of chemical compounds can be obtained by mounting the sample on a movable microscope stage and scanning the surface. These so-called Raman maps consist of a spectrum for each point while the entire map can contain up to a few thousand points. By selecting the wave number range of a peak that is typical for the investigated compound, its intensity in dependence on the position can be depicted which

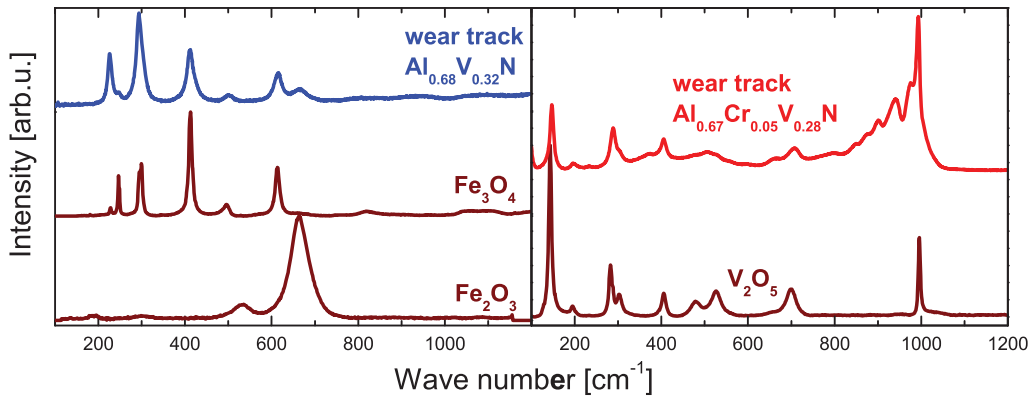

Figure 5.2: Raman spectra as measured in the wear track after tribological testing at 700°C. Standard spectra used for the identification of the chemical compounds are given as reference.

is equivalent to the lateral distribution. In Figure 5.3a a Raman map is shown, where this method was used to visualise the worn surface after tribological tests. Here, the presence of Fe_2O_3 is attributed to high intensities of the wave number 413 cm^{-1}, a typical lattice vibration for this oxide. As observable, the major part of the wear track contains Fe_2O_3 indicating that the original coating was worn through during the test. Further, it is also possible to map two ore more chemical compounds as shown in Figure 5.3b where the red colour indicates higher concentrations of V_2O_5 and green of $AlVO_4$ [13]. In this case, a model spectrum for each compound, that is similar to the standard spectrum, was extracted from the data and these spectra were mapped in a 2-dimensional array of 68×153 data points. The so obtained Raman map corroborates the finding that the formation of V_2O_5 in the tribological test of $Al_{0.68}Cr_{0.07}V_{0.25}N$ (bias –150 V) at 700°C is not sufficient to maintain a continuous lubricious layer in the tribological contact zone as it is removed from the center of the wear track to its margins. This results in an increased friction since $AlVO_4$ does not reveal lubricious effects. Further details can be found in Publication V.

Besides using Raman spectra as fingerprints for unknown materials, the measured Raman shifts are, as mentioned above, directly related to vibrational oscillations of the lattice or molecule. In Reference [14] the obtained Raman bands of AlCrN in fcc configuration were assigned to phonon modes. Further, as shown in Publication III, the studied AlCrVN coatings can be synthesised with the single-phase fcc crystal structure of AlCrN by using higher ion energies during deposition provided by higher bias voltages. Therefore, only slight deviations assigning the Raman shifts of fcc-AlCrVN are expected as compared to AlCrN in Reference [14]. Another possible application of Raman spectroscopy utilises variations of the peak position due to changes in the chemical composition. In Reference [15] the peak shift resulting from varying the Al content in AlCrN coatings is calibrated with the composition obtained by EPMA. In this way, a fast and non-destructive method for measuring chemical compositions is obtained. Limitations are, however, the restriction to a fixed set of elements, while only one element can be varied at a time, and the availability of precise cal-

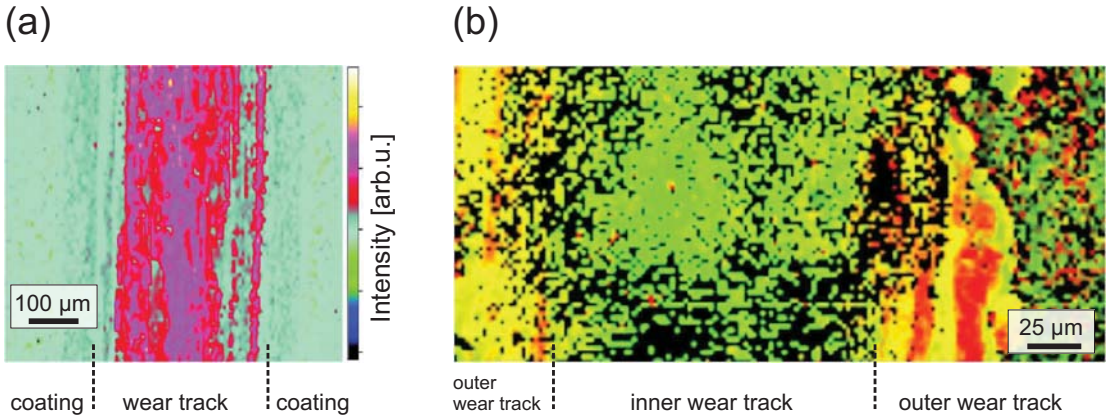

Figure 5.3: Raman maps of the wear track of (a) $Al_{0.40}Cr_{0.60}N$ (bias -40 V) and (b) $Al_{0.68}Cr_{0.07}V_{0.25}N$ (bias -150 V) after ball-on-disc tests at 700°C. In (a) the intensity of 413 cm^{-1}, a typical peak for Fe_2O_3, is mapped. In (b) the red colour indicates higher concentrations of V_2O_5 and green of $AlVO_4$ while in yellow areas both phases are present with approximately equal concentrations [13].

ibration data. Considering these restrictions, semi-quantitative chemical analysis by Raman spectroscopy might be used in industrial operations for routine validation of the chemical composition of hard coatings.

5.3 Secondary ion mass spectrometry (SIMS)

In SIMS the surface of the studied sample is sputtered by energetic primary ions that impact on the surface and transfer their energy through direct or indirect collisions to the material. This leads to the ejection of neutrals or charged particles from the surface while the latter are utilised as signal for SIMS [1, 16]. Normally, ion to neutral ratios in the range of 10^{-3} to 10% are obtained which determine the detection limit for a specific element, whereas higher ratios signify lower or better detection limits. Factors that influence the so-called ion yield are given by the ionisation potential or electron affinity of the selected atom, the chemical nature of the sample and the chemical composition of the primary ion beam that, most commonly, consists of O_2^+ or O^-, Cs^+ and Ar^+ with energies ranging from 0.5–20 keV. In general, SIMS is featured with an excellent sensitivity, i.e., detection limits for most elements in the ppm to ppb range are possible. Further advantages are due to the ability of SIMS to distinguish different isotops of one element and by monitoring molecular ions information on chemical bonding at the surface is revealed. On the other hand, the major drawback in using SIMS is the variation of the detection sensitivities by orders of magnitudes for different elements in one substrate or one specific element in various substrates. The use of standards or reference materials measured under equal conditions is mandatory for quantitative analyses. Further, care has to be taken defining the parameters for investigations since the primary ion beam alters the studied sample due to processes like intermixing, thermal segregation, topography changes and redeposition of other material into the analysed zone [16]. In order to avoid the

latter, the analysis is usually restricted to ions that originate from an area in the center of the sputter crater.

A schematic diagram of a typical spectrometer is shown in Figure 5.4 while SIMS can be operated in several different modes and a wide variety of information is obtained [1]. For measuring impurities present in the investigated material, a mass scan by monitoring all secondary ions as a function of their mass is performed. Since this mode is operated continuously during a certain time, information about the depth or the position of specific elements on the surface is not provided. The lateral distribution of chosen elements can be studied by scanning the primary ion beam over the surface while the resolution of the recorded SIMS image depends on the spot size. Here, diameters of the primary ion beam as low as 50 nm are possible. A third mode of operating SIMS is obtained, if material is continuously removed from the surface allowing the analysed zone to advance into the sample. In this case, selected ions can be monitored as a function of time leading to depth profiles of the studied sample. Calibration of the depth scale is done by measuring the crater depth and correlating the result to the total sputter time while assuming a constant sputter rate.

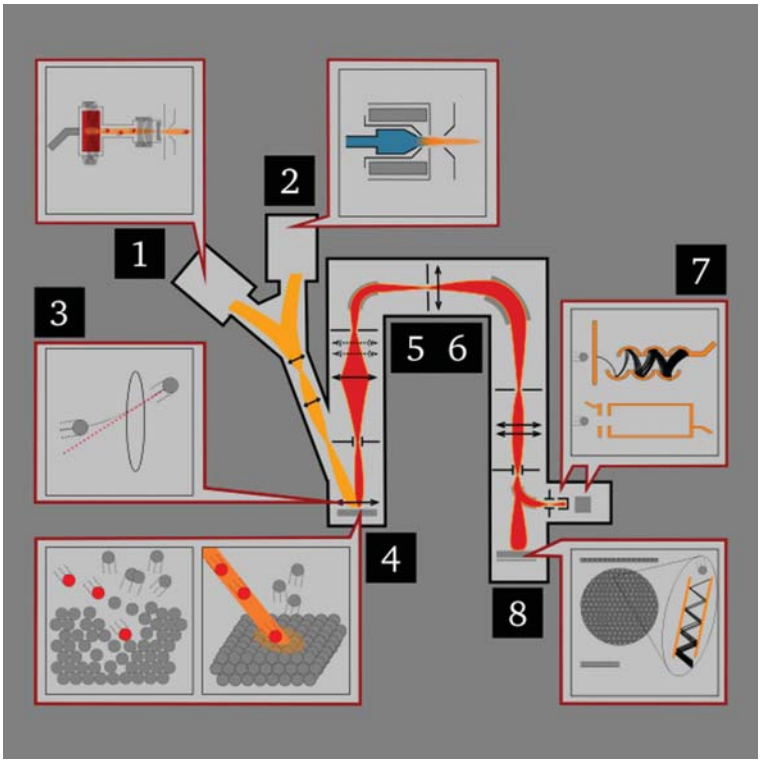

Figure 5.4: Schematic illustration of a SIMS instrument: (1) and (2) primary ion sources, (3) electrostatic lens, (4) sample, (5) electrostatic sector - ion energy analyser, (6) electromagnet - mass analyser, (7) electron multiplier / Faraday cup and (8) channel-plate / fluorescent screen - ion image detector.

Publication IV presents SIMS measurements of oxidised AlCrVN coatings while the depth profiles for V, Al and Cr are shown in Figure 5.5. The results reveal an onset temperature of oxidation at 600°C, whereas a dual-layer structure of the oxidised part is obtained at 700°C.

V out-diffusion, most likely driven by a phase separation, leads to the formation of a V-rich toplayer containing the lubricious oxide V_2O_5 and an underlying V-depleted layer consisting of a mixed $(Al,Cr,V)_2O_3$ and $AlVO_4$. On the other hand, there are no indications for a directed diffusion of Al and Cr as can be seen in Figure 5.5b and c. Within this work, no calibration of the ion yield and sputter rate in relation to the present chemical composition has been performed and the profiles, therefore, serve only as a qualitative measure of the situation encountered after oxidation.

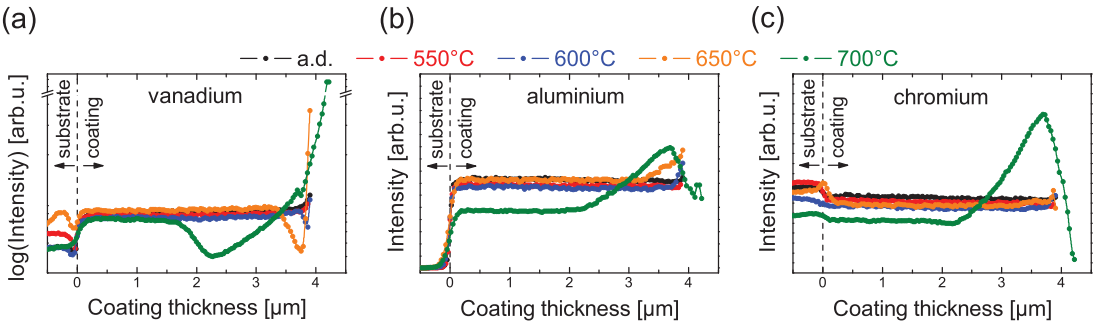

Figure 5.5: (a) V, (b) Al and (c) Cr depth profiles of oxidised $Al_{0.68}Cr_{0.10}V_{0.22}N$ at different annealing temperatures as obtained by SIMS. Lines are a guide for the eye.

5.4 Transmission electron microscopy (TEM)

TEM has become one of the major investigation methods in materials science due to its excellent resolution and versatility. The technique is based on an electron beam penetrating a thin specimen while undeflected and deflected electrons are utilised as signal [1]. Magnetic lens systems guide and focus the electrons to the investigated sample with a thickness of less than 200 nm and further to the detector that can be a fluorescent screen, film plate or camera. Due to the very small wavelength of electrons, magnifications ranging from 50 to 10^6 are possible while the maximum resolution depends on the energy of the electrons. An increase from 100 to 400 keV results in a reduction of the electron wavelength from 0.0037 to 0.0016 nm and, hence, better resolution. However, the beam has to be highly coherent with monochromatic electrons in order to obtain the desired resolution. A shortcoming of TEM is due to the projection of a three-dimensional sample on a two-dimensional detector and, hence, nearly complete loss of depth resolution. Therefore, samples have to be very thin in order to avoid overlapping of features in the projected image which places high demands on the sample preparation methods and in some cases preparing a useful specimen can be at least as difficult as the TEM investigation itself. Nowadays, it is common to use focused ion beams (FIB) to prepare appropriate samples. This method is explained in the References [17] and [18].

In general, two different modes are possible for the operation of a TEM [1]. In diffraction mode the specimen is illuminated with a parallel electron beam for best coherency. The

diffraction volume can be limited by an aperture and a so-called selected area electron diffraction (SAED) pattern is obtained which provides information that is equivalent to XRD. Further details about diffraction in TEM can be found in Reference [19]. The other mode utilises the transmitted electron beam to acquire an image of the illuminated zone. When the electrons penetrate the sample material, they can interact with the present atoms causing the appearance of diffracted beams besides the undiffracted beam consisting of the electrons that conserved their energy. Blocking all diffracted beams, a bright-field image is recorded where the contrast arises from thickness variation, changes of the density (atomic mass) or present structural anomalies. Contrary to bright-field images, dark-field images are obtained if one of the diffracted beams is displayed. Here, dislocations that cause diffraction of electrons appear bright, whereas the undistorted crystal is black. For high-resolution images, the unaltered transmitted and at least one diffracted beam are displayed in a way that their amplitude and phase are preserved. Constructive or destructive interference between both beams leads to phase-contrast images of columns of atoms [19]. In the Publications III and IV bright field images and SAED were used to characterise the synthesised AlCrVN coatings as well as the formed oxides after heat treatment in ambient air.

However, TEM has no inherent ability to distinguish atomic species and two complementary methods are used for analytical TEM investigations which will be presented more detailed. High-energy electrons that pass through matter can cause excitations of the present atoms giving rise to energy-dispersive X-ray (EDX) spectroscopy and electron energy-loss spectroscopy (EELS) [1]. The process of X-ray emission by excited or ionised atoms is well studied and utilised in EDX. As all atomic species emit specific energies, a recorded spectrum contains the "fingerprints" of each element and can be used to quantify the chemical composition of the investigated sample. On the other hand, the inelastically scattered electrons lose energy as they interact with the atoms. The resulting energy distribution reflects the energy transfer while EELS spectra yield the highest amount of information per inelastic scattering event. Contrary to other analytical signals that arise from secondary decay processes, EELS is obtained from a primary interaction event providing the basis for energy-filtered TEM (EFTEM).

In conventional EFTEM, the study of structure and chemical composition of a certain material is possible with a resolution better than 1 nm. As EFTEM images are not directly interpretable due to the non-element-specific background in EELS, two techniques have been established: the three-window and the jump-ratio technique [20]. Figure 5.6 visualises the three-window technique which allows for preparing a quantitative image where the intensity is proportional to the intensity in the EELS spectrum under the studied excitation edge. In order to estimate the background according to the model AE^{-r} with the energy loss E and two fitting parameters A and r, two pre-edge images are acquired first, whereas the post-edge image recorded next contains the excitation edge of interest. Subtracting the estimated background from the post-edge image, an excitation-specific image remains, the so-called elemental map. The parameters that can be varied for improving the quality of the obtained map, are the position and width of each energy window. However, several artifacts, e.g. drift, can lead to a false quantification while some issues can be overcome by acquiring only one pre-edge and one post-edge image. Dividing both images results in a jump-ratio image which contains qualitative information of the elemental distribution. Normally, the signal-to-noise ratio is improved since no extrapolation of the background is necessary and

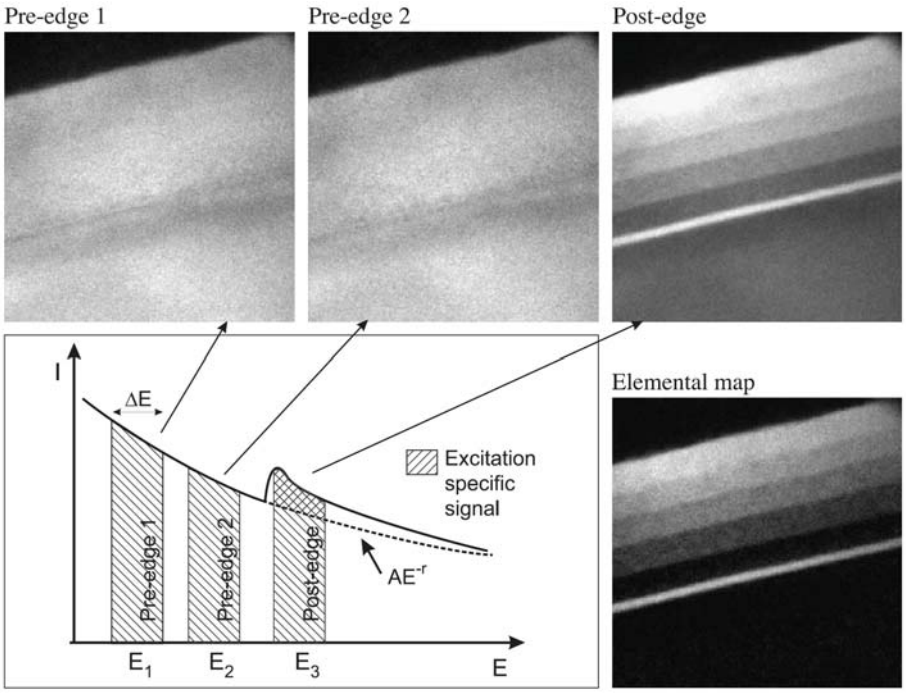

Figure 5.6: Schematic overview of the three-window technique. Two pre-edge images are used to estimate the background by fitting a background model AE^{-r}. This background estimation is subtracted from the post-edge image to obtain an elemental map. [20]

the acquisition of only two images slightly reduces drift problems. A jump-ratio image of AlCrVN was recorded in order to study any preferential incorporation of V into fcc-AlCrVN or w-AlCrVN (see Publication III).

Deficiencies using energy windows, however, arise when elements with overlapping ionisation edges are of interest. As shown in Figure 5.8a and b, analysing the content of V, O and Cr in oxidised AlCrVN coatings by conventional EFTEM results in an incorrect estimation of the EELS background. For Cr, e.g., the two pre-edge images are influenced by the V and O signal and other methods have to be applied. In advanced energy-resolved techniques like scanning TEM spectrum imaging (STEM SI), the collected data can be seen as a three-dimensional data cube as shown in Figure 5.7. A dataset with two spatial axes and one energy axis allows for precise correlation between spatial and spectral features [21]. Elemental mappings in case of STEM SI are obtained by scanning with a focused electron beam over the investigated zone while a complete EELS spectrum is acquired at each point or pixel. This method was first proposed by Jeanguillaume and Colliex in 1989 [22], but only increased computational speed and memory as well as fast spectrum readout in the last years enabled the usage of STEM SI for routine measurements. The key advantage of STEM SI is the availability of the full spectrum permitting postacquisition processing of the data. By choosing the spectral feature of interest from the recorded spectra, elemental mappings can be extracted which in turn means, that no prior knowledge of the expected spectral characteristics is necessary. Further, a full and accurate processing of each individual spectrum results in improved quality and more precise maps. Among the shortcomings of STEM SI,

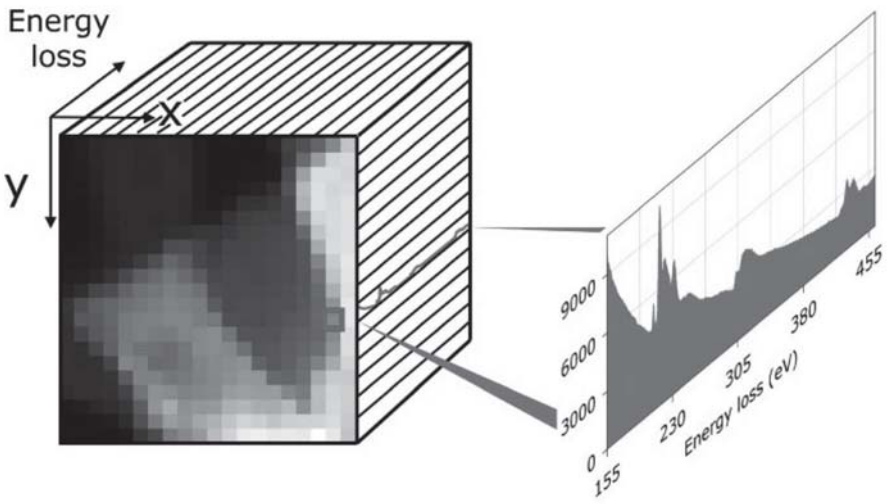

Figure 5.7: Schematic illustration of the three-dimensional data cube with two spatial axes, x and y, and an energy axis, E, that is used in STEM SI. [21]

the long total acquisition time is a major issue. In order to avoid a very long measurement time, the acquisition time at each pixel has to be very short leading to very noisy individual spectra and, therefore, the low-energy part with its higher intensity is commonly preferred.

Although STEM SI was developed using EELS spectra, the energy axis can also be given by, e.g., EDX spectra. In Publication IV elemental mappings of N and O from EELS and V, Al, Cr and Fe from EDX are presented (see also Figure 5.8). As already mentioned, the limitation in using conventional EFTEM due to the apparent overlap was overcome by applying the STEM SI method for extracting the elemental maps. In principle, it is possible to use EELS as well as EDX for all studied elements, but it is favourable to use one of them for certain elements. The signals in the low-loss region of the EELS spectrum that result from scattering on Al atoms (Al-L lines) are overlapped by the background which would lead to an inaccurate Al mapping. On the other hand, the specific X-ray radiation from light elements is out or near the lower limit of the energy range of common EDX detectors. Therefore, the elemental mappings of the non-metallic and light elements, N and O, were obtained by recording EELS spectra serving as energy axis, whereas EDX spectra at the same position were acquired for the metal components, V, Al, Cr and Fe. Further details as to the results and conclusions are included in Publication IV.

5.5 X-ray photoelectron spectroscopy (XPS)

In the above mentioned EDX spectroscopy, the atoms were excited by an electron beam and emitted X-ray radiation subsequently. The opposite process creates the basis for XPS where the sample is illuminated with X-rays of a well known energy $h\nu$ [16]. Ionisation of the atoms leads to the ejection of electrons, the photoelectrons, that are analysed towards their kinetic energy E_{kin}. Both values are correlated by Einstein's photoelectric law:

$$E_{kin} = h\nu - E_b \,,$$

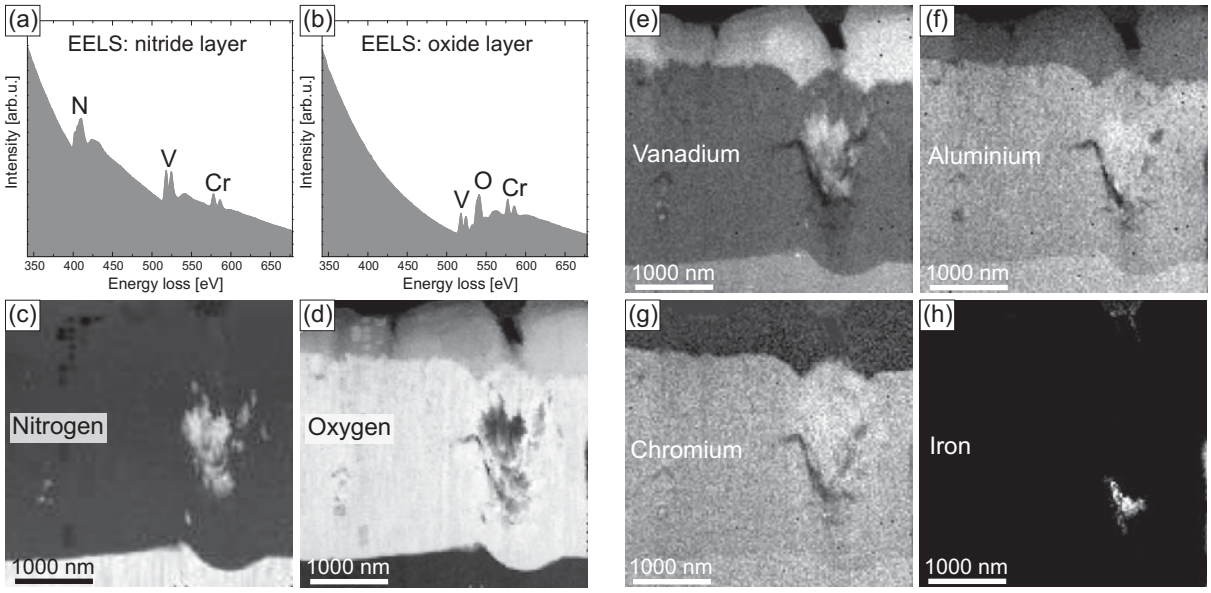

Figure 5.8: Examples of EELS spectra from (a) the unaffected $Al_{0.68}Cr_{0.10}V_{0.22}N$ coating and (b) the oxidised part. The elemental mappings were obtained by the STEM SI technique from EELS spectra in case of (c) N and (d) O while EDX spectra were used for (e) V, (f) Al, (g) Cr and (h) Fe.

from where the original binding energy of the electron can be calculated. A typical XPS spectrum is shown in Figure 5.9 which was excited by using a monochromised Al K_α beam of 1486.6 eV. Highly energetic X-ray sources are needed in order to eject electrons from the core levels, whereas monochromatisation is advantageous as the appearance of X-ray line satellite peaks can be avoided. On the other hand, the incident beam has to be sufficiently intense in order to provide for a detectable electron flux for the electron energy analyser which mainly determines the sensitivity and resolution of the XPS system. Here, the inelastic mean-free path of the electrons inside the sample is very limited leading to the exceptional surface sensitivity of XPS. Electrons with energies in the range of 100–1200 eV have a mean-free path of 0.5–2.0 nm, i.e., a typical information depth is not more than 15–20 monolayers [1, 16]. Further, the actual escape depth depends on the emission angle and measurements at high angles to the surface normal reveal information from the first monolayers only.

The spectrum itself contains a series of lines that arise from the unique excitation energies of each present element and, in principle, all elements except H are detectable while the spectral features vary. Elements like N and O with 1s orbital energies in the measureable energy range reveal single lines, whereas spin-orbit splitting causes two separate lines for p, d and f orbitals. As depicted in Figure 5.9, the splitting of V2p and Cr2p is clearly observable, in case of Al2p the energy difference is below the resolution limit. Other spectral features are due to the emission of Auger electrons and shake-up processes. The latter appears if the ionised atom remains in an excited state after ejecting the photoelectron which in turn results in peaks at slightly higher binding energies. Commonly, peak shifts are caused by different chemical environments, different oxidation states, different lattice sites, etc. These chemical shifts can be up to several eV and allow for a determination of the binding state of

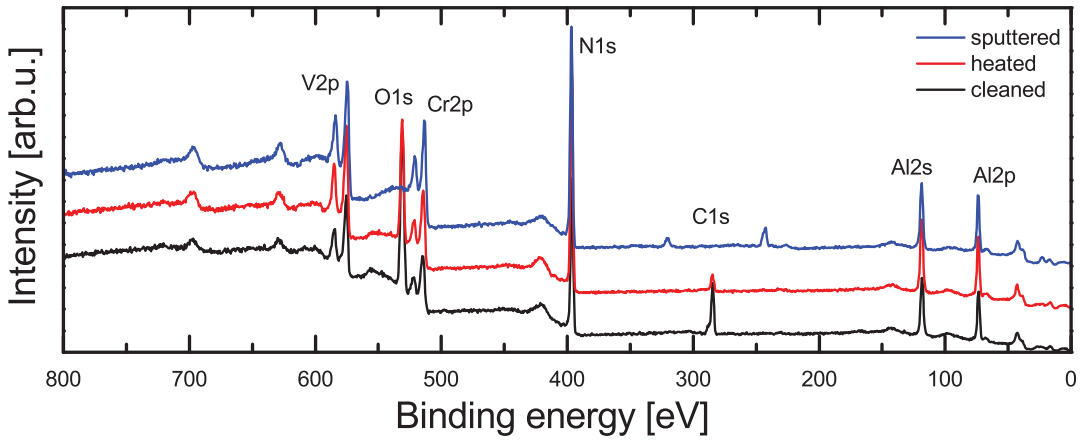

Figure 5.9: XPS spectra of $Al_{0.67}Cr_{0.17}V_{0.16}N$ recorded after different sample pretreatments: ultra-sonic cleaning in ethanol, in-situ heating to 350°C and sputter cleaning with 2 keV Ar ions.

the investigated element by comparing with reference catalogues [23, 24]. In Publication III analyses of the relevant core level spectra revealed the absence of intermetallic compounds in the synthesised AlCrVN coatings. All metallic components are exclusively bonded to N or, in the near-surface zone, to O. The surface oxides make up a considerable fraction of the total recorded signal as XPS represents a very surface sensitive method.

On this account, certain care has to be taken during sample preparation since every adsorbed compound will interfere as well with the desired signals. In Figure 5.9 a comparison between ultra-sonic cleaning, in-situ heating and sputter cleaning is shown. In this case, heating the sample to 350°C prior to the analysis, reduces adsorbed O and C or compounds containing these elements. A complete removal of these adsorbates is achieved by sputter cleaning, but the significant energy transfer might alter the binding states, especially if metastable chemical compounds are subject of the analysis. Thus, for the XPS investigation of AlCrVN coatings, heating prior to recording the spectra was applied.

References

[1] C. R. Brundle, C. A. Evans, and S. Wilson, eds., *Encyclopedia of Materials Characterization*, Materials Characterization Series (Butterworth-Heinemann, Boston, 1992).
[2] E. Mittemeijer and P. Scardi, eds., *Diffraction Analysis of the Microstructure of Materials* (Springer, Berlin, 2004).
[3] W. Oliver and G. Pharr, J. Mater. Res. **7**, 1564 (1992).
[4] A. Fischer-Cripps, *Nanoindentation* (Springer, New York, 2004), 2nd ed.
[5] A. Fischer-Cripps, Surf. Coat. Technol. **200**, 4153 (2006).
[6] P. Mayrhofer and C. Mitterer, Surf. Coat. Technol. **133-134**, 131 (2000).

[7] L. Freund and S. Suresh, *Thin Film Materials - Stress, Defect Formation and Surface Evolution* (Cambridge University Press, 2003).
[8] W. Demtröder, *Experimentalphysik 3: Atome, Moleküle und Festkörper* (Springer, Berlin, 1996).
[9] R. McCreery, *Raman Spectroscopy for Chemical Analysis*, vol. 157 of *Chemical Analysis* (Wiley-Interscience, New York, 2000).
[10] V. Brázdová, M. Ganduglia-Pirovano, and J. Sauer, J. Phys. Chem. B **109**, 394 (2005).
[11] L. Briand, J.-M. Jehng, L. Cornaglia, A. Hirt, and I. Wachs, Catal. Today **78**, 257 (2003).
[12] B. Leyer, H. Schmelz, H. Göbel, H. Meixner, T. Scherg, and H. Knözinger, Thin Solid Films **310**, 228 (1997).
[13] R. Kaindl, private communication.
[14] R. Kaindl, R. Franz, J. Soldan, A. Reiter, P. Polcik, C. Mitterer, B. Sartory, R. Tessadri, and M. O'Sullivan, Thin Solid Films **515**, 2197 (2006).
[15] R. Kaindl, B. Sartory, J. Neidhardt, R. Franz, A. Reiter, P. Polcik, R. Tessadri, and C. Mitterer, Anal. Bioanal. Chem. (2007), doi: 10.1007/s00216-007-1540-4.
[16] D. O'Conner, B. Sexton, and R. Smart, eds., *Surface Analysis Methods in Materials Science*, Springer Series in Surface Science (Springer, Berlin, 2003), 2nd ed.
[17] L. Giannuzzi and F. Stevie, Micron **30**, 197 (1999).
[18] J. Mayer, L. Giannuzzi, T. Kamino, and J. Michael, MRS Bulletin **32**, 400 (2007).
[19] B. Fultz and J. Howe, *Transmission Electron Microscopy and Diffractometry of Materials* (Springer, Berlin, 2002), 2nd ed.
[20] J. Verbeeck, D. Van Dyck, and G. Van Tendeloo, Spectrochim. Acta, Part B **59**, 1529 (2004).
[21] V. Keast and M. Bosman, Microsc. Res. Tech. **70**, 211 (2007).
[22] C. Jeanguillaume and C. Colliex, Ultramicroscopy **28**, 252 (1989).
[23] La Surface database, *http://www.lasurface.com/accueil/*.
[24] NIST database, *http://srdata.nist.gov/xps/*.

6 Summary

In order to design a hard coating that offers lubricious effects at elevated temperatures, V was incorporated into AlCrN coatings. The state-of-the-art AlCrN hard coatings are characterised by high hardness and good thermal stability and oxidation resistance, but reveal a high coefficient of friction in high-temperature tribological tests. On the contrary, the V oxide V_2O_5 has been found to act as a solid and liquid lubricant in the temperature range from 500 to 700°C and, in general, it was shown that alloying AlCrN hard coatings with V beneficially influences their tribological behaviour. The synthesis of the new AlCrVN hard coatings by arc-evaporation in an industrial-scale deposition system results in coatings with the for transition metal nitrides typical columnar and dense morphology. Differences, on the other hand, are observed when investigating the crystal structure of coatings deposited at low bias voltages (–40 to –100 V). Within this work, a constant Al concentration in the targets was used that results in nitride coatings with compositions close to the metastable solubility limit of AlN in fcc-CrN. As shown in Table 4.2, Cr was stepwise substituted by V while fcc-VN exhibits a slightly lower solubility for AlN. This leads to the formation of an additional phase with the thermodynamically stable wurtzite type structure of AlN which is more pronounced at higher V contents. An analysis of the elemental distribution of V by EFTEM revealed no preferential incorporation in either phase and it can be concluded that the fcc-AlCrVN as well as the w-AlCrVN phase have a comparable composition. As to the mechanical properties, the occurrence of the dual-phase structure results in reduced hardness and residual stress values.

However, the formation of the fcc-AlCrVN phase can be stabilised by using higher energetic growth conditions which are obtained by applying higher bias voltages during deposition. At a bias voltage of –150 V, a metastable single-phase fcc-AlCrVN can be retained, even for the composition that revealed the maximum w-AlCrVN phase fraction at –40 V. The crystal structure of the so formed coating is equal to the structure of $Al_{0.71}Cr_{0.29}N$ that was the starting point for the V incorporation and, thus, serves as a reference. This structural evolution may be due to the strong increase of compressive stress caused by the higher defect density that is generated by the bombardment with highly energetic ions at higher bias voltages. Since the fcc phase presents a by 25% higher density as compared to the wurtzite type phase, its formation might be energetically favoured. Additionally, ion irradiation during thin film growth enhances adatom diffusion and collisional mixing at the growth front which should be beneficial for the stabilisation of the fcc phase as they counteract the mechanisms of adatom mobility driven phase separation. However, the change in the crystal structure has a distinct influence on the hardness. The measured hardness values rise with increasing bias voltage due to strain hardening as a result of the higher defect density and the transformation of the w-AlCrVN phase to the mechanically more favourable fcc-AlCrVN.

The main focus within this work, however, was on the tribological behaviour of AlCrVN coatings as investigated by ball-on-disc tests. At room temperature the addition of V does

not alter the coefficient of friction, only at temperatures of 500°C and higher differences were observed. Detailed analyses of in ambient air annealed samples by SIMS depth profiling and STEM SI elemental mapping revealed the appearance of a dual-layer structure of the oxidised part while the outer oxide is V enriched and the inner oxide V depleted. This development is most likely driven by a phase separation since the present V oxides, V_2O_5 and V_2O_3, are immiscible with Al_2O_3 and Cr_2O_3 (see phase diagrams in Figure 3.3). The separation process appears to be incomplete after one hour of annealing and, hence, the inner oxide consists of a mixed $(Al,Cr,V)_2O_3$ with a porous morphology. On the other hand, the main constituent of the outer oxide is V_2O_5 with its orthorhombic crystal structure where the weakly bonded (001) planes allow for easy shearing which in turn gives rise to the expected solid lubrication. Additionally, V_2O_5 exhibits a low melting point of 670°C and forms a liquid lubricious layer in this temperature range. Thus, the recorded lowest COF of 0.2 in tribological tests at 700°C is mainly attributed to liquid lubrication mechanisms. Further, if compared to V alloyed TiAlN based coatings, the AlCrVN coatings mirror the higher oxidation resistance of AlCrN and, hence, retain their mechanical integrity at higher temperatures still offering low-friction effects.

More details concerning the interrelationship between structure, oxidation and tribological properties were obtained by investigating the influence of the bias voltage during deposition. The aforementioned single-phase fcc-AlCrVN coating reveals a moderate increase of the COF at 700°C as compared to the coatings deposited at lower bias voltages. From analyses of the oxidation behaviour of fcc-AlCrN and w-AlCrN it is known, that the denser cubic phase is more oxidation resistant than the wurtzite type phase. Assuming a similar behaviour for AlCrVN, the reduced formation of V_2O_5 with increasing fcc-AlCrVN phase fraction is not sufficient to maintain a continuous lubricious layer. The present V_2O_5 is probably removed from the wear track during sliding which results in the observed higher friction.

Finally, AlCrVN coatings that showed a low-friction behaviour at 700°C were tested as to their suitability in metal cutting operations. Despite the fact of partly exhibiting lower hardness, tools coated with AlCrVN revealed a lifetime in the range of commercial AlCrN in side milling tests of stainless steel under dry conditions. In these preliminary results, no lubricious effects could be evidenced so far, especially because of contamination with wear products, but the obtained results give reason to further optimisation. In summary, the synthesised AlCrVN coatings retain the necessary mechanical integrity in tribological tests and applications while the formation of V_2O_5 offers lubricious effects at temperatures $\sim$700°C leading to a distinct reduction of the coefficient of friction.

7 Abbreviations

CCD	charge-couple device
COF	coefficient of friction
DLC	diamond-like carbon
EDX	energy-dispersive X-ray spectroscopy
EELS	electron energy-loss spectroscopy
EFTEM	energy-filtered transmission electron microscopy
EPMA	electron probe microanalysis
fcc	face-centered cubic
HSS	high-speed steel
PTFE	polytetrafluoroehtylene
PVD	physical vapour deposition
RT	room temperature
SAED	selected area electron diffraction
SEM	scanning electron microscopy
SIMS	secondary ion mass spectrometry
STEM SI	scanning transmission electron microscopy spectrum imaging
TEM	transmission electron microscopy
w	wurtzite type
XPS	X-ray photoelectron spectroscopy
XRD	X-ray diffraction

8 Publications

8.1 List of included publications

I. High-temperature tribological studies of arc-evaporated $Al_xCr_{1-x}N$ coatings,
R. Franz, B. Sartory, R. Kaindl, R. Tessadri, A. Reiter, V.H. Derflinger, P. Polcik, C. Mitterer,
in Proc. 16th Int. Plansee Seminar, (ed. G. Kneringer et al.), Reutte (A), Vol. **2**, 932-945 (2005).

II. High-temperature low-friction properties of vanadium-alloyed AlCrN coatings,
R. Franz, J. Neidhardt, B. Sartory, R. Kaindl, R. Tessadri, P. Polcik, V.H. Derflinger, C. Mitterer,
Tribology Letters **23(2)**, 101-107 (2006).

III. Micro- and bonding structure of arc-evaporated AlCrVN hard coatings,
R. Franz, J. Neidhardt, B. Sartory, R. Tessadri, C. Mitterer,
Thin Solid Films, submitted.

IV. Oxidation and diffusion processes during annealing of AlCrVN hard coatings,
R. Franz, J. Neidhardt, B. Schaffer, H. Hutter, R. Kaindl, B. Sartory, R. Tessadri, M. Lechthaler, P. Polcik, C. Mitterer,
Journal of Vacuum Science and Technology A, submitted.

V. Influence of phase transition on the tribological performance of arc-evaporated AlCrVN hard coatings,
R. Franz, J. Neidhardt, R. Kaindl, B. Sartory, R. Tessadri, M. Lechthaler, P.Polcik, C. Mitterer,
final preparation.

8.2 List of related publications

VI. Structural investigation of aluminium-chromium-nitride hard coatings by Raman microspectroscopy,
R. Kaindl, R. Franz, J. Soldan, A. Reiter, P. Polcik, C. Mitterer, B. Sartory, R. Tessadri, M. O'Sullivan,
Thin Solid Films **515**, 2197-2202 (2006).

VII. Semi-quantitative chemical analysis of hard coatings by Raman micro-spectroscopy: the aluminium chromium nitride system as an example,
R. Kaindl, B. Sartory, J. Neidhardt, R. Franz, A. Reiter, P. Polcik, R. Tessadri, C. Mitterer,
Analytical and Bioanalytical Chemistry (2007) in press.

8.3 My contribution to included publications

	Conception and planning[1]	Experiments	Analysis and interpretation	Manuscript preparation[1]
Publication I	100	50	70	100
Publication II	100	50	75	95
Publication III	100	50	85	100
Publication IV	100	30	60	100
Publication V	100	50	80	100

[1]Supervision not included

Publication I

High-temperature tribological studies of arc-evaporated $Al_xCr_{1-x}N$ coatings

R. Franz, B. Sartory, R. Kaindl, R. Tessadri, A. Reiter, V.H. Derflinger, P. Polcik, C. Mitterer

in Proc. 16th Int. Plansee Seminar, (ed. G. Kneringer et al.), Reutte (A), Vol. **2**, 932-945 (2005)

High-temperature tribological studies of arc-evaporated $Al_xCr_{1-x}N$ coatings

R. Franz[1], B. Sartory[2], R. Kaindl[2], R. Tessadri[2], A. Reiter[3], V.H. Derflinger[3], P. Polcik[4], C. Mitterer[1]

1 Christian Doppler Laboratory for Advanced Hard Coatings at the Department of Physical Metallurgy and Materials Testing, University of Leoben, Austria
2 Christian Doppler Laboratory for Advanced Hard Coatings at the Institute for Mineralogy and Petrography, University of Innsbruck, Austria
3 Balzers AG, Balzers, Liechtenstein
4 Plansee AG, Reutte, Austria

The recently introduced $Al_xCr_{1-x}N$ coatings are characterised by their outstanding thermal stability and oxidation resistance. Although several studies on the microstructure and mechanical properties of these coatings have been published, the tribological behaviour especially at elevated temperatures has not been addressed yet. Within this work, the tribological properties of arc-evaporated $Al_xCr_{1-x}N$ coatings were investigated at different temperatures as a function of the Al to Cr ratio. Coatings were deposited using an industrial-scale arc-evaporation system (Balzers RCS) and AlCr targets with an Al to Cr ratio ranging from 0 to 1. The chemical composition of the resulting coatings was analysed by electron probe microanalysis. Tribological properties were evaluated using a high-temperature ball-on-disc tribometer at room temperature, 500°C and 700°C against alumina balls. The wear coefficients of the coatings and their wear mechanisms were investigated using optical profilometry and Raman spectroscopy. It is shown that the friction and wear behaviour strongly depends on the Al content and the testing temperature. Although higher ratios of Al/Cr increase the friction, the wear resistance of these coatings is improved. These results support the previously established superior performance for these coatings in cutting applications.

Keywords: AlCrN, arc-evaporation, tribology, wear, Raman spectroscopy

1 Introduction

The ternary Al-Cr-N coating system has been introduced and investigated over the last years in order to improve the properties of CrN, which already shows excellent corrosion resistance and low friction properties [1]. These properties make CrN an excellent coating for metal forming applications [2] and extrusion [3]. However, in the field of metal cutting and other high temperature applications it failed to fulfil the high demands on hardness and resistance against abrasive wear and oxidation.

It was shown that the performance of CrN can be improved by alloying with other metals. Although CrN already shows good oxidation resistance it can be further improved by alloying with Al [4]. For the Ti-Al-N system it is known, that the onset temperature for oxidation can be increased from app. 550°C for pure TiN to app. 800°C [5]. A protective layer of Al2O3 was observed on the surface of coating resulting in a superior oxidation resistance compared to TiN. In the case of AlCrN the same process could be found, but with increased temperature [4]. In general, an improved oxidation behaviour for higher aluminium containing coatings was observed. For the ternary Al-Cr-N system a maximum solubility of app. 77% AlN in CrN was predicted and verified [6, 7]. Similar to the oxidation behaviour the thermal stability is significantly enhanced [8] as well as the hardness [9–11] and the abrasive wear [6, 7].

This work investigates the tribological properties of coatings within the ternary Al-Cr-N system, where the compositions range from pure CrN over four different $Al_xCr_{1-x}N$ coatings to AlN.

2 Experimental details

The different $Al_xCr_{1-x}N$ coatings were synthesised in an industrial-scale arc-evaporation system (RCS, Balzers Liechtenstein) with a base pressure below 4×10^{-3} Pa. Prior to deposition the substrates were plasma heated to 500°C in an Ar/H2 atmosphere and etched in pure Ar plasma with ions extracted from an additional discharge. The substrate bias voltage was kept constant at –40 V, except for AlN where a pulsed bias had to be applied due to its insulating character. The 6 cathodes were current controlled during deposition to 140 A and the nitrogen gas pressure was kept constant at 3.5 Pa. For CrN and $Al_{0.19}Cr_{0.81}N$ the deposition time was 100 min, for the other coatings it was increased to 110 min.

The high-speed steel (DIN 1.3343) coupons (ø 40mm) used as substrates were ground and polished to a 3 μm finish after quenching and tempering to a hardness of 65 HRC. Prior to deposition the samples were cleaned in a multi-stage ultrasonic cleaning line using aqueous alkaline baths. The coating thickness was measured by ball cratering.

The tribological tests were performed using ball-on-disc tribometers from CSM Instruments designed for tests at room temperature and high temperature ($\leq$ 700°C), respectively. The normal load was kept constant at 5 N and the sliding speed was set to 10 cm/s. No lubricant was applied. Alumina balls with a purity of 99.8% and a diameter of 6 mm were chosen as counterpart, due to their chemical inertness at high temperatures. For each testing temperature the sliding distance was set to 300 m and the radius of the wear track to 7 mm. In addition, a 1000 m run with a radius of 9 mm was done at room temperature. The wear tracks on the coatings were analysed using an optical 3D white light profiling system (Wyko NT 1000) at 5 spots evenly distributed along the circumference of the track. From these measurements the wear volume was determined and the wear coefficient calculated as ratio of the volume and the applied force times the sliding distance [12].

Hardness measurements were not conducted within this work, values are found in the literature. In reference [11] the Vickers microhardness was obtained using a conventional test with a load of 0.5 N. The values for HU_{pl} taken from an earlier study [8] were measured using a H100C Fischerscope applying a maximal load of 25 mN.

The chemical composition was determined by electron probe microanalysis (EPMA) by means of wavelength dispersive X-ray spectroscopy (WDX) using a JEOL JXA 8100 Superprobe. 10 kV were applied as acceleration voltage which resulted in a beam current of 80 nA. The analysed spot size was approximately 40×40 μm. Cr and Al standards for quantitative analysis had purities of 99.96% and 99.9999%, respectively. A thin layer of Si_3N_4 on Si was used as nitrogen standard, for more details see reference [13].

The Raman analysis of the wear tracks was done by a HORIBA-JOBIN YVON Labram-HR800 confocal spectrometer, employing a He-Ne laser with a wavelength of 632.8 nm for excitation. The Raman signal was detected with a CCD-camera using a 100× objective. Beam diameter and power on the sample surface was about 2 μm at 1 mW. Raman mappings were produced using a motor-driven X-Y-stage and the spectral mapping procedures of the LabSpec spectrometer software.

3 Results

3.1 Coating structure and properties

The results of the EPMA measurements are shown in Table 1 and are in good agreement with earlier results [8]. A deficiency of aluminium in the coating as compared to the target composition is detected. It is most pronounced for the Cr-rich coatings (23.7% for $Al_{0.19}Cr_{0.81}N$ to 5% for $Al_{0.81}Cr_{0.19}N$). The coatings with higher Cr contents are slightly understoichiometric as to the nitrogen concentration as compared to AlN with values ranging from 47.0% to 52.9%, respectively. The thickness is ≥ 4 μm for all coatings.

Table 1: Comparison of the metal ratio in the target and in the coating for all compositions investigated. Additionally the nitrogen content and the coating thickness are shown.

Coating System	Metal Ratio Target		Metal Ratio Coating			Coating Thickness
	Al [%]	Cr [%]	Al [%]	Cr [%]	N [%]	[μm]
CrN	0	100	0	100	47.0	4.1
$Al_{0.19}Cr_{0.81}N$	25	75	19.1	80.9	46.4	4.8
$Al_{0.40}Cr_{0.60}N$	50	50	40.3	59.7	49.1	4.3
$Al_{0.62}Cr_{0.38}N$	70	30	62.2	37.8	49.9	3.9
$Al_{0.81}Cr_{0.19}N$	85	15	80.8	19.2	51.7	5.6
AlN	100	0	100	0	52.9	4.2

Previous XRD investigations [6, 11] revealed with increasing Al content a change in the crystal structure. Up to an Al concentration of app. $x = 0.77$ the coating retains the fcc structure of CrN, while a higher Al content causes a phase change to the hcp structure of AlN. The XRD patterns in Figure 1 illustrate this phase change.

Investigations on AlCrN coatings yielded values for the Vickers microhardness of 2700 HV [11] or for Hu_{pl} of app. 38 GPa [8]. The highest values are found for coatings with the highest ratio Al/Cr, but still remaining the fcc structure.

3.2 Tribological behaviour

From tribological experiments two major results can be derived. On one hand, the behaviour of the coefficient of friction with the sliding distance is recorded. For this study its dependence on the temperature was investigated. Therefore, three different temperatures were chosen, namely room temperature, 500°C and 700°C. Figure 2 gives an overview of the steady-state coefficient of friction for the whole range of coatings. With increasing Al content, the coefficient of friction is rising regardless the temperature. Only for pure AlN there is a reduction at elevated temperatures in comparison to $Al_{0.81}Cr_{0.19}N$. While the highest values were found at 500°C, the coefficient of friction at RT and 700°C are in a comparable range for all coatings.

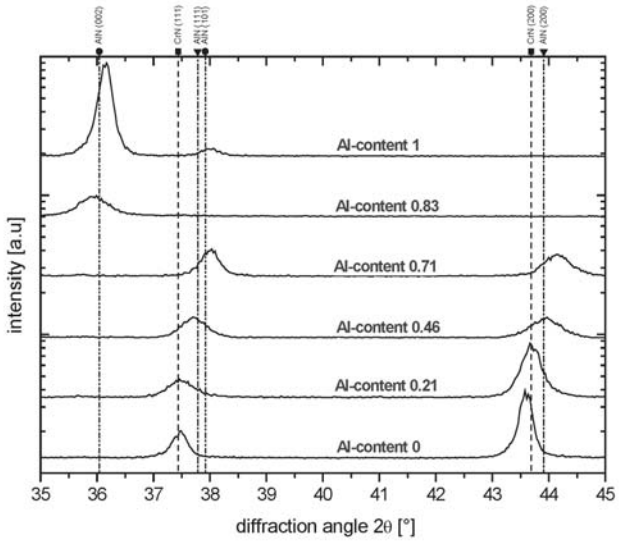

Figure 1: XRD patterns of coatings with different Al to Cr ratios. The phase change from fcc to hcp structure can be seen. The figure was taken from reference [8].

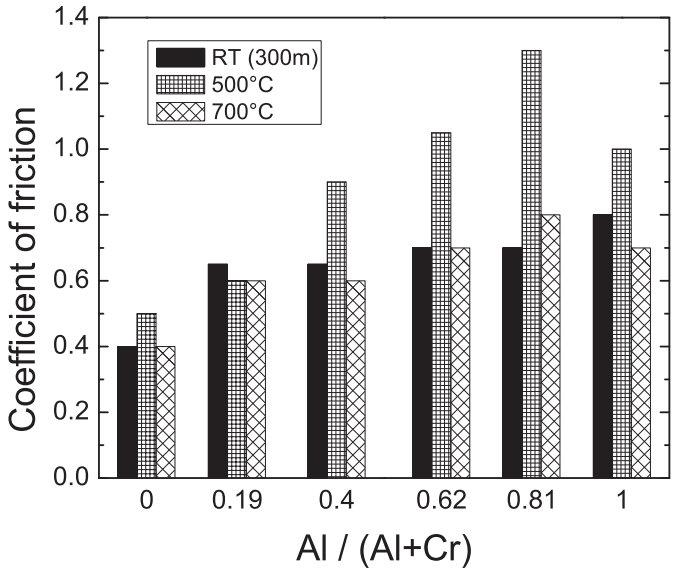

Figure 2: Coefficient of friction against Al_2O_3 in dependence on the coating Al content and the temperature in the tribological test.

Figure 3 exemplifies the coefficient of friction for $Al_{0.62}Cr_{0.38}N$ in dependence on the sliding distance. The black curve shows the friction at room temperature. After a running-in period of app. 50 m, a steady-state friction is reached. By increasing the temperature to 500°C the scattering is more pronounced, but the running-in period decreases to 25 m. An interesting behaviour can be observed for 700°C, where the coefficient of friction in the first 50 m is equal to the one for 500°C. Then it decreases down to the room temperature value and remains constant over the rest of the sliding distance.

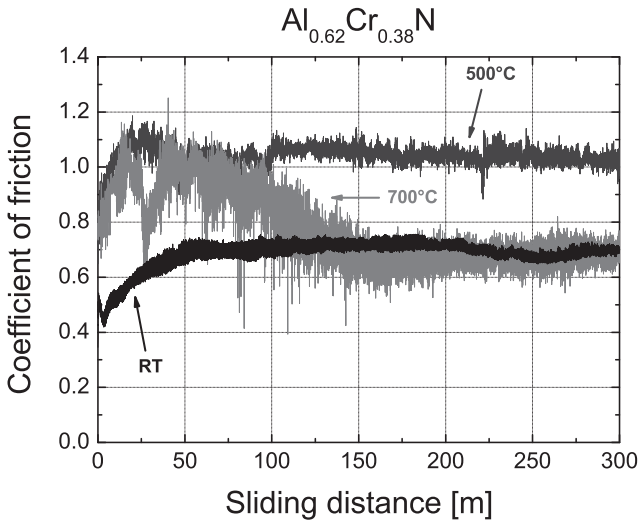

Figure 3: Coefficient of friction obtained against Al_2O_3 in dependence on the sliding distance for the three investigated temperatures. $Al_{0.62}Cr_{0.38}N$ exemplifies all other coatings.

The 3D profile of the wear tracks after testing is shown in Figure 4. The images were obtained by optical profilometry. In the case of room temperature there is no visible wear after a sliding distance of 1000 m. At higher temperatures a wear track can be observed. Table 2 shows a comparison between the depth of the different wear tracks and the thickness of the coating. In the case of CrN only after testing at 500°C the coating is clearly worn through, while it stays intact at RT and 700°C. This behaviour changes when adding Al to the coating. Here, only a very low depth could be measured at RT. Increasing the temperature results in a wear track depth in the range of the coating thickness for the two coatings with low Al contents. The two Al-rich coatings reveal the highest resistance against wear. Even at the maximum temperature of 700°C the depth of the wear track does not reach the coating thickness. The results for AlN show a peculiarity. While the coating is removed in the wear track at RT and 700°C, it stays intact at 500°C.

Using the results from optical profilometry the wear coefficient can be derived as a second tribological value and is displayed for the whole range of the investigated coatings in Figure 5. A minimum in wear is observed for the composition $Al_{0.62}Cr_{0.38}N$ for all temperatures. In general, the wear coefficients for room temperature are app. two orders of magnitude lower than for elevated temperatures. The only exception is AlN, where all coefficients are in the same range.

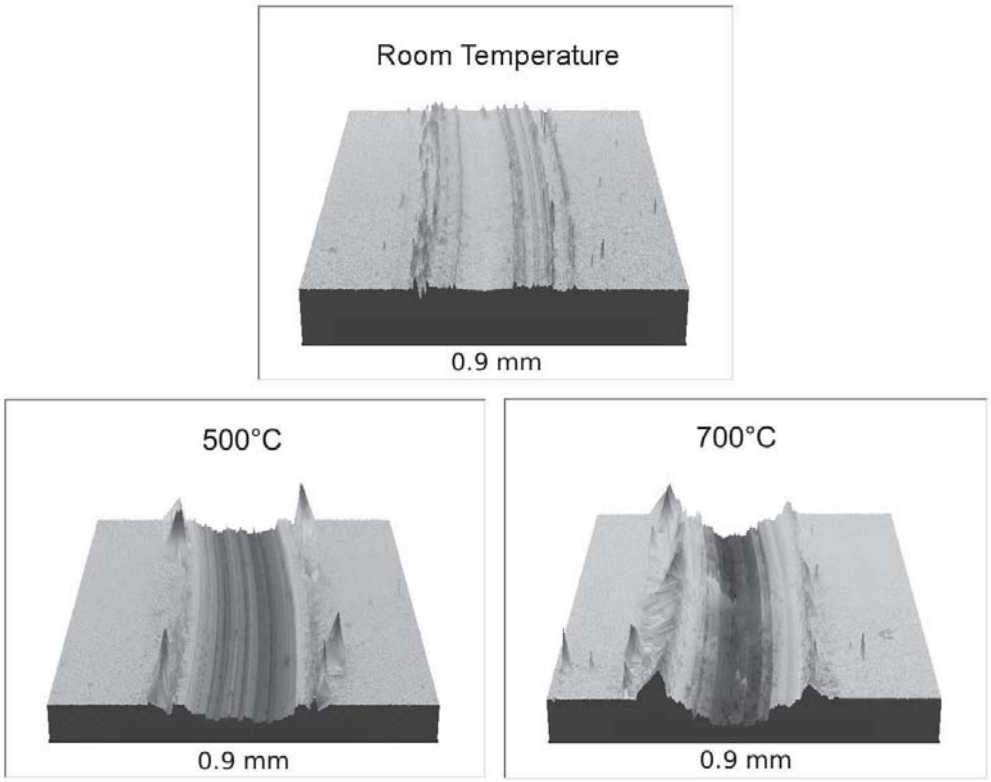

Figure 4: 3D images obtained by optical profilometry of wear tracks after ball-on-disc tests against Al_2O_3 at different temperatures (sliding distances: 1000 m for room temperature; 300 m for 500°C and 700°C). $Al_{0.62}Cr_{0.38}N$ exemplifies all other coatings.

Table 2: Depth of wear tracks after tribological testing compared to coating thickness.

Coating System	Depth of Wear Track [μm]			Coating Thickness [μm]
	RT	500°C	700°C	
CrN	0.2	11.1	1.1	4.1
$Al_{0.19}Cr_{0.81}N$	0.1	3.9	4.0	4.8
$Al_{0.40}Cr_{0.60}N$	0	4.7	3.9	4.3
$Al_{0.62}Cr_{0.38}N$	0	1.3	2.4	3.9
$Al_{0.81}Cr_{0.19}N$	0.2	1.5	3.0	5.6
AlN	4.5	1.6	3.8	4.2

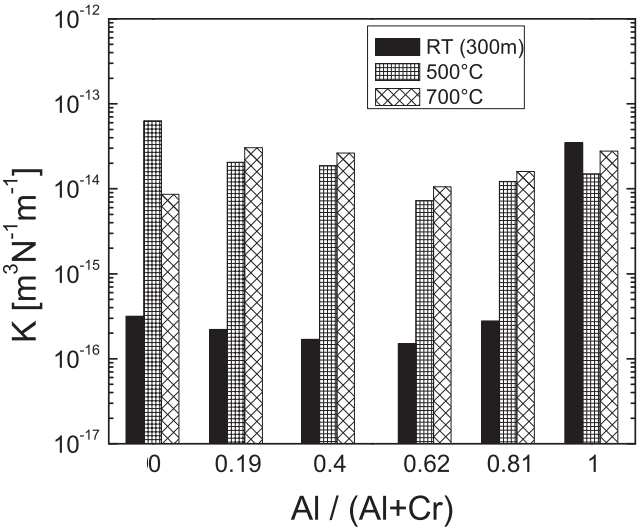

Figure 5: Wear coefficient of $Al_xCr_{1-x}N$ coatings tested against Al_2O_3 in dependence on coating composition and conditions of ball-on-disc test.

3.3 Raman spectroscopy

Raman spectroscopy was used to analyse the material in the wear debris and track after the respective tests. Figure 6 shows the results for all compositions and temperatures. Pure CrN reveals high amounts of iron oxides at 500°C, while at 700°C there is mainly chromium oxide Cr_2O_3 (even though the coating is not worn through). At room temperature there is no distinct peak because of weak intensity of the Raman active scattering modes of CrN.

The first three $Al_xCr_{1-x}N$ coatings (i.e. for $x \leq 0.62$) show a similar wear behaviour. Up to 500°C they retain the fcc structure of pure CrN, accompanied by shifts in relative intensity and frequency of the spectra. Only at 700°C weakly crystallized iron oxides can be observed. From the Raman map in Figure 7 it can be observed, that there are regions where the coating remains, while in the other parts Fe_2O_3 was detected. The coating $Al_{0.81}Cr_{0.19}N$ already shows the hexagonal structure of pure AlN. Again, at 700°C haematite (Fe_2O_3) and magnetite (Fe_3O_4) can be found. For AlN the iron oxides are already detectable at 500°C.

4 Discussion

The behaviour of the wear rate at room temperature can be related to the hardness of the coatings. In reference [8] the highest hardness values (HU_{pl}) were found for Al contents of 0.46 (app. 38 GPa) and 0.71 (app. 37 GPa). This corresponds well to the minimum of the wear coefficient for $Al_{0.62}Cr_{0.38}N$ in this work. Coatings with lower concentration of Al have the same phase structure, but lower hardness. If the Al concentration exceeds app. 77%, the structure changes to hcp and the hardness strongly decreases. Only for pure AlN there is a slight increase in hardness again. But still the observed wear coefficient is two orders of magnitude higher than for $Al_{0.81}Cr_{0.19}N$. This high value does not correspond to the

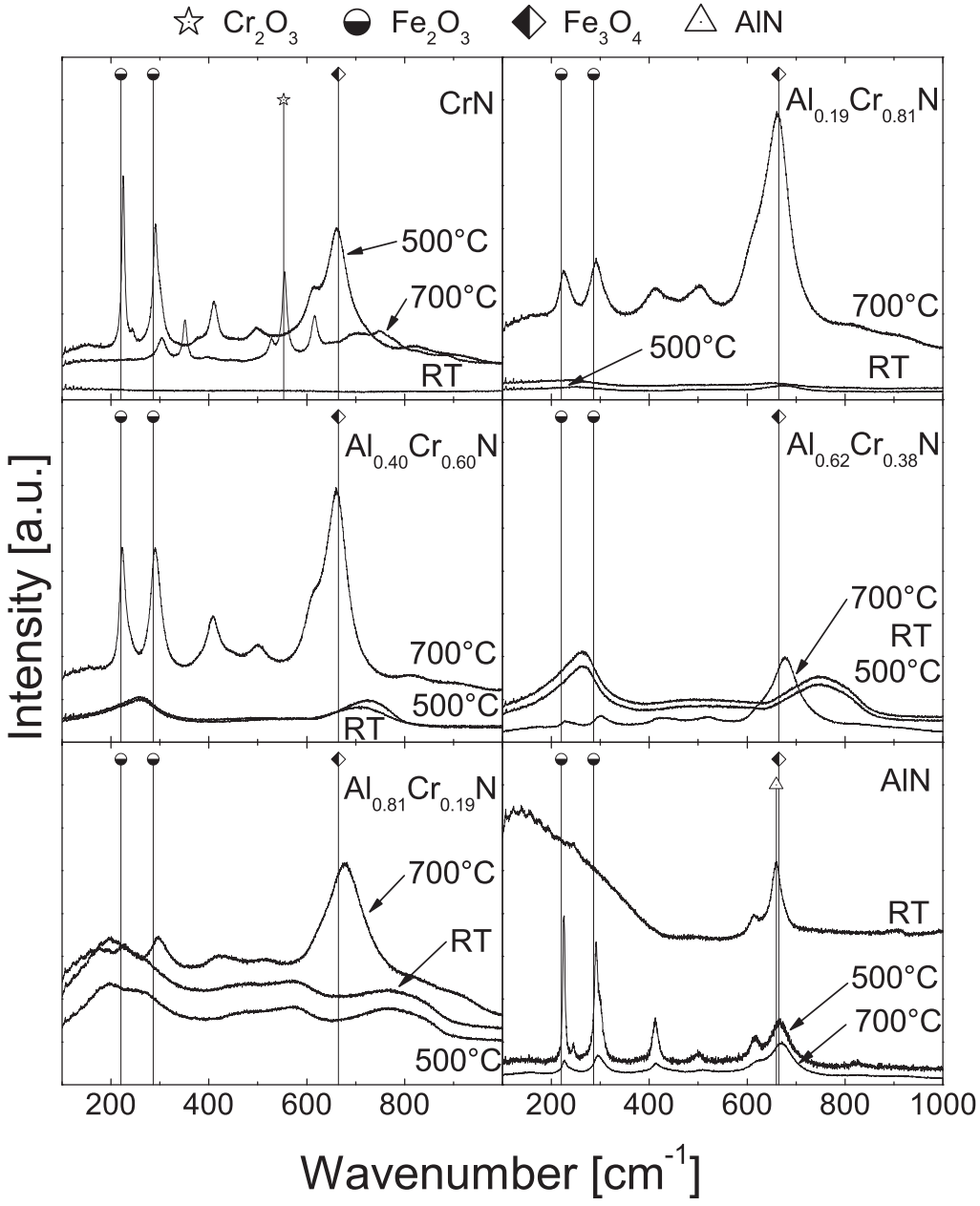

Figure 6: Raman spectra of wear tracks of $Al_xCr_{1-x}N$ coatings tested against Al_2O_3 at RT, 500°C and 700°C. The major Raman peaks of the relevant chemical compounds are indicated.

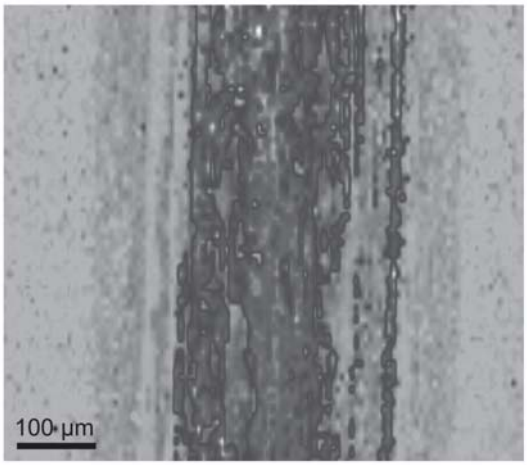

Figure 7: Raman map of the wear track of $Al_{0.40}Cr_{0.60}N$ after ball-on-disc test against Al_2O_3 at 700°C. The intensity of Fe_2O_3 peak at 413 cm^{-1} is given in dependence on the position in the wear track. Darker areas indicate higher intensities.

measurements in [8], but there the abrasive wear was measured by a ball cratering technique according to [14].

At elevated temperatures the wear coefficient increases drastically, but the minimum remains for the $Al_{0.62}Cr_{0.38}N$ coating. Beside the hardness, the oxidation resistance becomes important explaining the wear behaviour. Again, the highest oxidation resistance was found for an Al content of 0.71 in [8], which explains the relatively low wear coefficient. An exception is the pure CrN, which shows the lowest wear at 700°C. The reason for this behaviour is the formation of a Cr_2O_3 layer in the wear track, which was evidenced by Raman spectroscopy.

The origin of the iron oxides found in the wear tracks after testing at elevated temperatures can be explained by comparing the depth of the track with the appearance of specific peaks in the Raman measurements. If the coating is completely or almost worn through, as it is the case for the two coatings with a low Al content ($x \leq 0.40$) at 700°C, then there are distinct Raman peaks of Fe_2O_3 and Fe_3O_4. It was shown, that the coating stays intact in some parts of the wear track, but the diffusion barrier for iron atoms from the substrate is very low and a thin film of iron oxides is formed on the surface. For higher Al concentrations the peaks for haematite and magnetite weaken, indicating less diffusion of iron atoms to the surface. The reason can be found in higher wear resistance of $Al_{0.62}Cr_{0.38}N$ and $Al_{0.81}Cr_{0.19}N$ resulting in a decrease of the wear track depth. A different behaviour was found for the binary systems CrN and AlN. After the tribological test at 500°C the CrN coating was completely worn through and iron oxides were detected. The formation of Cr_2O_3 at 700°C prevents the diffusion of iron atoms through the coating. AlN reveals a wear track depth at RT in the range of the coating thickness, but no iron oxide was found. At elevated temperatures there is evidence for an iron oxide layer in the wear track, even though the coating was not worn through after testing at 500°C. It can be concluded, that the AlN coating has a reduced resistance towards diffusion of iron atoms.

Closely connected to the results discussed above are the coefficients of friction obtained

from the tribological test. In the absence of mainly iron oxides in the wear track the values for the friction coefficient are primarily related to the coating properties. The reduction in friction in the steady-state by increasing the testing temperature from 500°C to 700°C can be attributed to the formation of thin friction layer containing high amounts of iron oxides. Testing the uncoated substrates with the same conditions at 700°C, a coefficient of friction of app. 0.3 was obtained. In general, the coefficients of friction are significantly higher as compared to the magnetron sputtered coatings in reference [15].

5 Conclusion

The evolution of the wear coefficient by alloying CrN with Al is directly related to the phase structure and the hardness. Increasing the Al content in the coating increases the hardness and decreases the wear. The optimum is found for the maximum concentration of Al while still retaining the fcc structure of CrN, here $Al_{0.62}Cr_{0.38}N$. If the Al/Cr ratio exceeds app. 0.77, then the phase changes to hcp and the tribological performance of the coating deteriorates.

Summing up, $Al_xCr_{1-x}N$ coatings with their beneficial combination of mechanical, tribological and oxidation behaviour have been proven to be excellent candidates for high temperature tribological applications.

Acknowledgement

Financial support by the Christian Doppler Research Association is highly acknowledged. The authors are grateful to Jörg Neidhardt for fruitful discussions during the preparation of this work.

References

[1] K.-H. Baether, U. Herrmann, and A. Schroeer, Surf. Coat. Technol. **75**, 793 (1995).
[2] J. Vetter, Surf. Coat. Technol. **76-77**, 719 (1995).
[3] T. Björk, M. Berger, R. Westergard, S. Hogmark, and J. Bergström, Surf. Coat. Technol. **146-147**, 33 (2001).
[4] M. Kawate, A. Hashimoto, and T. Suzuki, Surf. Coat. Technol. **165**, 163 (2003).
[5] W. Münz, J. Vac. Sci. Technol. A **4**, 2717 (1986).
[6] A. Sugishima, H. Kajioka, and Y. Makino, Surf. Coat. Technol. **97**, 590 (1997).
[7] Y. Makino and K. Nogi, Surf. Coat. Technol. **98**, 1008 (1998).
[8] A. Reiter, V. Derflinger, B. Hanselmann, T. Bachmann, and B. Sartory, Surf. Coat. Technol. **200**, 2114 (2005).
[9] O. Knotek, F. Loeffler, and H.-J. Scholl, Surf. Coat. Technol. **45**, 53 (1991).
[10] J. Vetter, E. Lugscheider, and S. Guerreiro, Surf. Coat. Technol. **98**, 1233 (1998).
[11] M. Kawate, A. Kimura, and T. Suzuki, J. Vac. Sci. Technol. A **20**, 569 (2002).
[12] E. Rabinowicz, *Friction and Wear of Materials* (Wiley-Interscience, New York, 1995), 2nd ed.

[13] S. Dreer, P. Wilhartitz, E. Mersdorf, and G. Friedbacher, Mikrochimica Acta **130**, 281 (1999).
[14] T. Michler and C. Siebert, Surf. Coat. Technol. **163-164**, 546 (2003).
[15] Y. Ide, T. Nakamura, and K. Kishitake, in *Proceedings of the Second International Conference on Processing Materials for Properties*, edited by B. Mishra and C. Yamauchi (2000), pp. 291–296.

Publication II

High-temperature low-friction properties of vanadium-alloyed AlCrN coatings

R. Franz, J. Neidhardt, B. Sartory, R. Kaindl, R. Tessadri, P. Polcik, V.H. Derflinger, C. Mitterer

Tribology Letters **23(2)**, 101-107 (2006)

High-temperature low-friction properties of vanadium-alloyed AlCrN coatings

R. Franz[a], J. Neidhardt[a], B. Sartory[b], R. Kaindl[b], R. Tessadri[b], P. Polcik[c], V.H. Derflinger[d], C. Mitterer[a]

[a] *Christian Doppler Laboratory for Advanced Hard Coatings at the Department of Physical Metallurgy and Materials Testing, University of Leoben, Franz-Josef-Strasse 18, A-8700 Leoben, Austria*
[b] *Christian Doppler Laboratory for Advanced Hard Coatings at the Institute for Mineralogy and Petrography, University of Innsbruck, Innrain 52, A-6020 Innsbruck, Austria*
[c] *Plansee AG, A-6600 Reutte, Austria*
[d] *Balzers AG, FL-9496 Balzers, Liechtenstein*

V-alloyed AlCrN hard coatings were deposited by reactive arc-evaporation in a commercial Balzers RCS coating system. The Al/(Al+Cr+V) atomic ratio in the target was kept constant at 0.7, while the Cr was stepwise substituted by V. Alloying V into the AlCrN coatings led to the partial transformation to a hexagonal phase of the otherwise metastable cubic lattice, whereas the hexagonal phase fraction was observed to increase with the V concentration in the coating. This results in a reduction of hardness (from 28 GPa to 19 GPa) and biaxial coating stress (from -1700 MPa to -900 MPa). The performed tribological tests at high temperature revealed a significantly lower coefficient of friction down to a value of 0.2 for $Al_{0.67}Cr_{0.05}V_{0.28}N$ at 700°C. This behaviour is due to the formation and melting of the Magnéli phase oxide V_2O_5 forming a low-friction layer on the surface as indicated by Raman spectroscopy and scanning electron microscopy.

KEY WORDS: AlCrVN, AlCrN, lubricious oxides, Magnéli phases, arc-evaporation

1 Introduction

AlCrN coatings have been introduced successfully in metal forming applications, extrusion and metal cutting such as milling and drilling [1, 2]. They are characterised by higher hardness [3–5] and thermal stability [6] as well as increased resistance against abrasive wear [7, 8] and oxidation compared to CrN and TiAlN. This development was initially inspired by the beneficial properties achieved by alloying of Al in TiN, which increased its onset temperature of oxidation to app. 800°C due to the formation of a protective Al_2O_3 layer [9]. The incorporation of Al into CrN with Al/Cr ratios up to 3 increases this onset temperature further [10, 11], while even at these high Al concentrations in the coating a metastable face-centered cubic (fcc) structure is retained [7, 8].

In our previous work we reported on unlubricated ball-on-disc tests of AlCrN coatings with different Al/Cr ratios [12]. There, a minimum wear with a coefficient of friction (COF) of 0.7 was observed for $Al_{0.62}Cr_{0.38}N$ at room temperature. However, in general an increase to 1.0 was found for all AlCrN coatings at elevated temperatures above 500°C, a temperature range commonly encountered in cutting operations - especially under unlubricated conditions. A recently introduced approach for low-friction coatings in intermediate to high-temperature applications is the formation of lubricious surface oxides, the so called Magnéli phases [13]. Possible candidates are W, Mo, Ti and V [14, 15]. The lubricating effect of Magnéli phase oxides with their easily activated crystallographic shear planes due to an oxygen deficiency in the crystal lattice was demonstrated in high-temperature tribological testing of oxidised VN [16]. The intrinsic mechanical properties of VN were, however, not sufficient for the high demands in industrial applications. A break-through was achieved by incorporating

V in an existing hard coating, namely TiAlN via deposition of a superlattice structure like TiAlN/VN [17] or supersaturated Ti-Al-V-N films [18, 19]. It was reported, that the COF was reduced to app. 0.2-0.3 at 700°C compared to the room temperature values of app. 0.6-0.8.

This work, therefore, investigates the influence of V on the structure and mechanical properties of AlCrN with the aim of a potential formation of Magnéli phases and their beneficial effect in high-temperature friction.

2 Experimental

The systematic development of new AlCrVN-based coatings required a simultaneous development of suitable target materials by a flexible production method like powder metallurgy. The so produced AlCrV targets have a constant Al content of 70 at.% and V/(Al+Cr+V) ratios of 0.10, 0.15, 0.20 and 0.25, respectively (see Table 1). Additionally, an AlV target with a V content of 30 at.% was prepared. The addition of V to the AlCr composite does not drastically change the properties of the composite, like thermal conductivity, density, homogeneity or content of impurities, which provides for a V-content independent discharge characteristics. Therefore, the influence of V on the coating properties is assumed to depend only on the V concentration.

The different Al-Cr-V-N coatings were synthesised in an industrial-scale arc-evaporation system (Balzers RCS) with a base pressure below $4 \cdot 10^{-3}$ Pa. High-speed steel (DIN 1.3343, AISI M2) coupons (⊘ 30 mm × 10 mm) used as substrates were ground and polished to a 3 μm finish after quenching and tempering to a hardness of 65 HRC. Other substrates were cemented carbide cutting inserts (grade 10), silicon wafers and stripes (Si (100)) and a low-alloyed steel (DIN 1.0330, AISI 1008). The high-speed steel samples and the cutting inserts were cleaned in a multi-stage ultrasonic cleaning line using alkaline baths. The low-alloyed steel and the silicon were cleaned with ethanol. Prior to deposition, the substrates were plasma heated to 500°C and etched in a pure Ar plasma with ions extracted from an additional arc discharge. During deposition the substrate voltage and the N_2 gas pressure was kept constant at -40 V and 3.5 Pa, respectively, while the 4 cathodes were current-controlled at 140 A. The coatings were deposited to a thickness of 5-6 μm at a rate of app. 3 μm/hr.

The chemical composition of the resulting coatings was determined by electron probe microanalysis (EPMA) by means of wavelength-dispersive X-ray spectroscopy (WDX) using a JEOL JXA 8100 Superprobe under an acceleration voltage of 10 kV. The analysed spot size was approximately 40×40 μm. High purity Cr, V and Al were used as standards for quantitative analysis, while a thin layer of Si_3N_4 on Si served as nitrogen standard. The morphology of the coatings was analysed via cross sections using a Cambridge Instruments Stereoscan 360 scanning electron microscope (SEM). X-ray diffraction (XRD) data were obtained by a D8 diffractometer from Bruker AXS with parallel beam geometry and symetric reflection, a Cu-ceramic tube and an energy-dispersive detector (SolX from Bruker AXS). Hardness measurements were conducted using a H100C Fischerscope equipped with a Berkovich indenter in the constant-depth mode of 500 nm. The device was calibrated using a single crystalline sapphire (100) via the implemented procedures for hardness and tip shape correction. Stress measurements were conducted by means of the cantilever beam bending technique of Si (20

mm × 7 mm × 0.525 mm) stripes according to ref. [20].

The tribological tests were performed using ball-on-disc tribometers from CSM Instruments designed for tests at room and high temperature ($\leq 700°C$). The load was kept constant at 5 N and the sliding speed was set to 10 cm/s. No lubricant was applied. Sintered alumina balls with a purity of 99.8% and a diameter of 6 mm were chosen as counterpart, due to their chemical inertness at high temperatures. For each testing temperature the sliding distance was set to 300 m and the radius of the wear track to 7 mm. The worn-off volume of the wear tracks was determined by an optical 3D white light profiling system (Wyko NT 1000). 5 spots evenly distributed along the circumference of the track were measured and the so calculated volume used to obtain the wear coefficient of the coatings.

Raman spectra were obtained with a HORIBA Jobin Yvon LabRam-HR800 Raman microspectrometer. Spectra were excited at room temperature with the 633 nm line of a 5.9 mW He-Ne laser or the 514 and 489 nm line of a 30 mW Ar^+-laser. The laser spot on the surface had a diameter of approximately 1 μm and a power of 1 mW for the He-Ne and 5 mW for the Ar^+-laser, respectively. The laser power was reduced as soon as spectral changes or sample destruction due to local heating by light absorption was observed. The spectral resolution ranged between 0.8 and 2.1 cm^{-1} and the spectra were recorded unpolarized between 100-150 and 4000 cm^{-1}. All spectra were baseline corrected by subtraction of first- or second-order polynome.

3 Results

3.1 Composition and Structure

All coatings are well adherent and show a dark greyish colouration. An analysis of fracture cross-sections using SEM revealed a dense and homogeneous structure. A comparison between target and coating composition is given in Table 1. The films are all stoichiometric as it can be seen by a N ratio of app. 50 at.%. Further, the Cr and V contents in the coatings do not differ significantly from their respective ratios in the targets; only a minor Al deficiency of 2-3 at.% for the V-containing coatings is detected.

Table 1: Chemical composition of the targets compared to the metal ratio in the coatings and nitrogen concentration. Coating composition obtained by EPMA with an assumed error of 1 at.

Target composition $Al_{y_{Al}}Cr_{y_{Cr}}V_{y_V}$	Coating composition $Al_{x_{Al}}Cr_{x_{Cr}}V_{x_V}N$	N ratio (at.%)
$Al_{0.70}Cr_{0.30}$	$Al_{0.71}Cr_{0.29}N$	47.9 ± 1.0
$Al_{0.70}Cr_{0.20}V_{0.10}$	$Al_{0.68}Cr_{0.21}V_{0.11}N$	50.5 ± 1.0
$Al_{0.70}Cr_{0.15}V_{0.15}$	$Al_{0.67}Cr_{0.17}V_{0.16}N$	50.6 ± 1.0
$Al_{0.70}Cr_{0.10}V_{0.20}$	$Al_{0.68}Cr_{0.10}V_{0.22}N$	50.6 ± 1.0
$Al_{0.70}Cr_{0.05}V_{0.25}$	$Al_{0.67}Cr_{0.05}V_{0.28}N$	51.4 ± 1.0
$Al_{0.70}V_{0.30}$	$Al_{0.68}V_{0.32}N$	50.4 ± 1.0

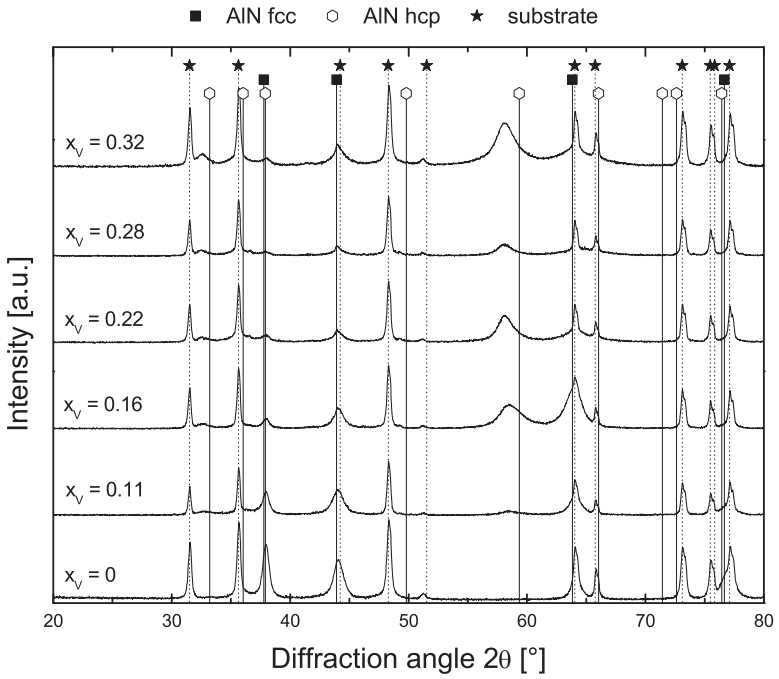

Figure 1: XRD patterns of the investigated coatings in the as-deposited state. Substrate material was cemented carbide.

The coating structure was analysed by means of XRD as shown in Fig.1. It is known from other investigations that AlCrN can be synthesised in the metastable fcc structure of CrN up to an Al/(Al+Cr) atomic ratio of app. 0.75 [7]. Above that limit a stable phase based on hexagonal close packed (hcp) AlN forms. Thus, the V-free coating $Al_{0.71}Cr_{0.29}N$ with an Al/(Al+Cr) atomic ratio lower than the above mentioned limit shows the predicted fcc structure. However, when adding V to the system Al-Cr-N an additional hcp phase forms. With increasing V content, the hcp phase becomes more evident and more crystalline.

A quantitative analysis of the phase fractions was done by Rietveld refinement. As XRD measurements represent bulk information from the whole coating and the substrate, the transition between nucleation and steady-state growth of the coating has to be considered. The XRD patterns were fitted assuming a coating structure with one hcp and two fcc phases. A second fcc phase was introduced in order to achieve a better description of variations in the peak positions, peak widths and peak ratios of the XRD data that are caused by the transition from nucleation to steady-state film growth. The dependency of the phase fractions on the V content is shown in Fig.2 while the fcc phase represents the sum of the two phases. Calculated crystallite sizes from the Rietveld refinement for the cubic phases are in the range of 3-13 nm for fcc phase 1 and 23-33 nm for fcc phase 2. The average lattice parameter of the two fcc phases is app. 4.105 Å which is lower than other reported values in the system Al-Cr-N for the same Al concentration [5–7]. An influence from the substitution of Cr by V can be neglected as the standard lattice parameter of VN is given by 4.137 Å compared to 4.14 Å for CrN.

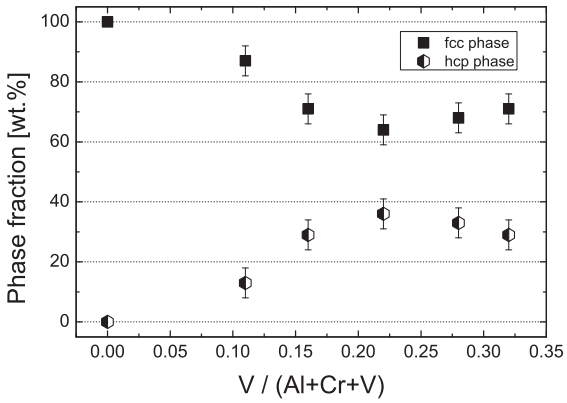

Figure 2: Phase fractions in AlCrVN coatings as a function of V content obtained by the Rietveld refinement method of XRD patterns.

However, the evolution of the hcp phase is more interesting for this work. While no clear trend of the crystallite size, being in the range of 8-10 nm, could be observed, the phase fraction rises with increasing V concentration (see Fig.2). Starting with an hcp phase fraction of 13 wt.% for the coating with the lowest V content ($x_\mathrm{V} = 0.11$), it reaches a saturation of ≈35 wt.% for $x_\mathrm{V} \geq 0.22$. The corresponding lattice parameter a rises from 3.150 Å to 3.171 Å which is distinctly higher than the standard value of 3.111 Å for hcp AlN. This effect of lattice expansion in a is known from investigations of AlCrN with Al concentrations that result in hcp coating structures [6, 7]. There, an expansion in c compared to the standard value of 4.979 Å is reported as well. The incorporation of V into AlCrN leads to a lattice shrinkage to 4.95 Å in c independent from the V content in the coating.

Summarising the structural investigations it can be stated that the incorporation of V leads to a two-phase structure of the coating with hcp and fcc crystallites. A second fcc phase has been added to the data fit in order to improve the description of variations in the XRD patterns due to thickness-dependent changes in the growth behaviour of the coating.

3.2 Mechanical Properties

Fig.3 shows the results of the indentation measurements. In general the indentation hardness $\mathrm{H_{IT}}$ decreases when alloying AlCrN with V. However, low fractions of V cause only slight changes. A significant decrease in hardness can be observed for coatings with $x_V \geq 0.16$. There the hardness is reduced from 28 GPa for $x_V = 0$ to 19 GPa in the case of $x_V = 0.28$. For the highest V concentration there is a slight increase in hardness indicated. The general loss in hardness is accompanied by a reduction in Young's modulus $\mathrm{E_{IT}}$ when V is added to coating. The reduction already starts for small V concentration and is from app. 380 GPa for $x_V = 0$ to app. 260 GPa for $x_V \geq 0.28$.

A similar behaviour can be found in the evolution of the biaxial coating stress. In general, the stress at RT reduces with increasing V ratio from -1700 MPa at $x_V = 0$ to -900 MPa when x_V rises to 0.22 (see Fig.4). A saturation in stress relaxation with increasing V content

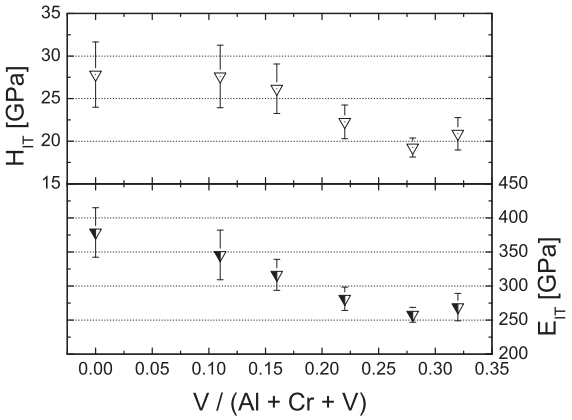

Figure 3: Hardness H_{IT} and Young's modulus E_{IT} depending on the V concentration in the coating.

is indicated for $x_V \geq 0.22$. Higher compressive stresses of up to -3000 MPa are found at a temperature of 500°C, but the overall behaviour varying the V content remains.

3.3 Tribology

All deposited coatings were analysed as to their friction behaviour. Special emphasis was given to high-temperature tribological tests. The recorded COF depending on the sliding distance is shown in Fig.5. At room temperature there is no dependence on the V content in the coating and in all tests a steady-state COF of app. 0.7 is reached, while the running-in period to reach these steady-state values varies between 20 m ($x_V = 0.22$) and 100 m ($x_V = 0.28$).

Similar tests at elevated temperatures revealed pronounced differences between the tested coatings. For $x_V \leq 0.11$ the COF is slightly increased or in the same range as in the case of room temperature. However, the scattering of the COF value increases with increasing testing temperature indicating a more pronounced stick-slip mechanism. A first indication of a reduction of friction can be seen for $x_V = 0.16$. While the COF rises to 0.9-1.0 at 500°C, it decreases to 0.6 at 700°C. A further increase of the V content to $x_V = 0.22$ results in a COF of 0.5 for both high-temperature tests. For 500°C this is the lowest COF recorded in this study. Testing the coating with $x_V = 0.28$ the same steady-state friction at 500°C could be observed, but the scattering is increased. At 700°C the lowest COF (0.2) of all performed tribological tests was recorded. The coating with the highest amount of V ($x_V = 0.32$) revealed an even more pronounced scattering at 500°C and a COF in the range of the RT test. Here, only the tribological test at 700°C resulted in reduction of friction with a COF of 0.4.

In order to investigate the mechanisms active during sliding, chemical analysis of the wear track was performed by means of Raman spectroscopy. Fig.6 shows the results depending on coating composition and temperature during the tribological tests. Starting at room temperature the obtained spectra are determined by the coating structure. Due to the

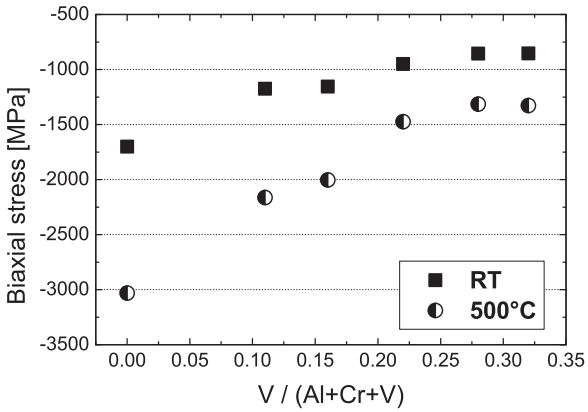

Figure 4: Biaxial coating stress at RT and 500°C of the different coatings. Substrate material was Si.

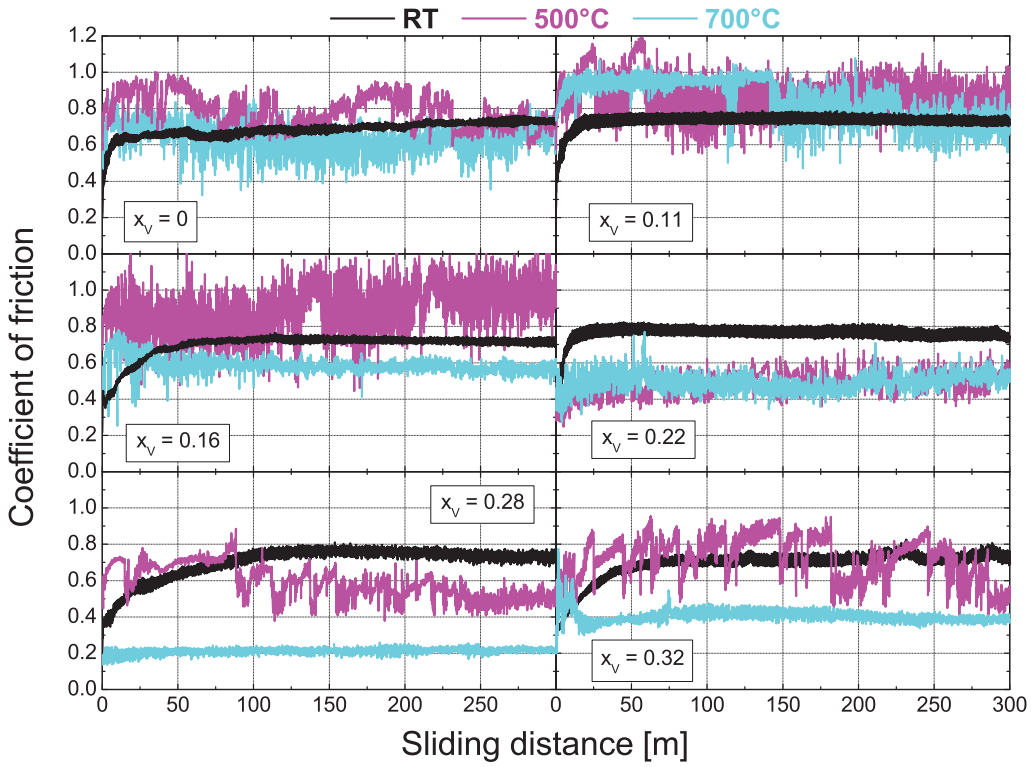

Figure 5: Coefficient of friction versus sliding distance obtained by tribological tests of AlCrVN coatings at RT, 500°C and 700°C.

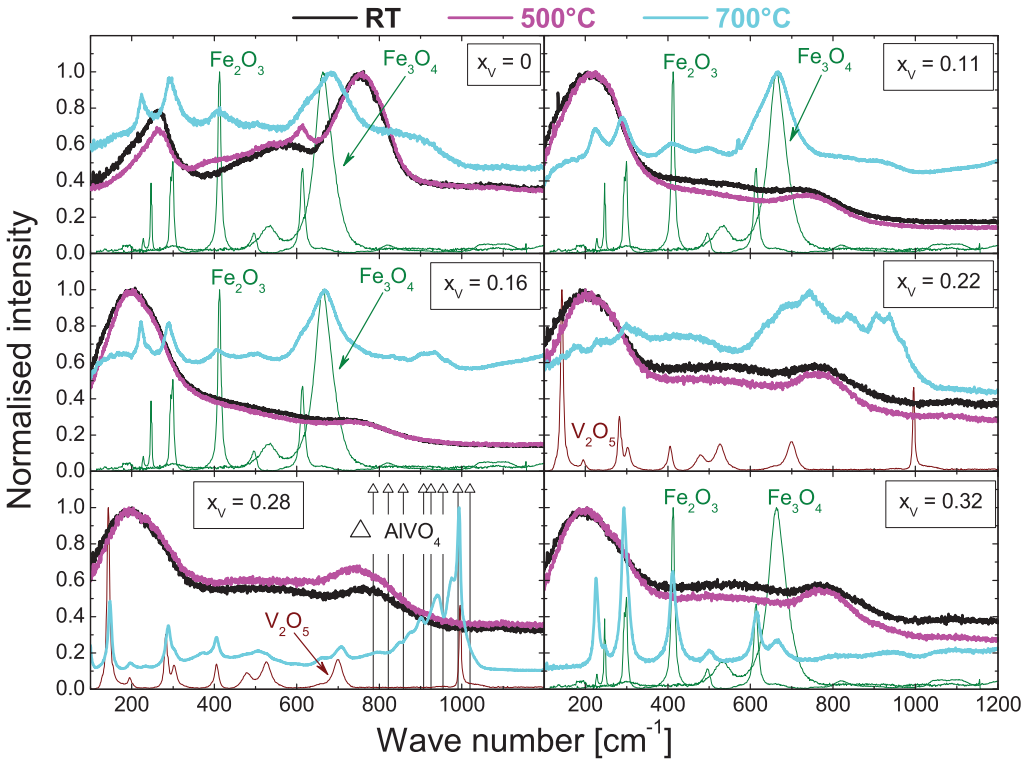

Figure 6: Raman spectra of the wear tracks after tribological testing at RT, 500°C and 700°C. Relevant standards are given for each coating composition ($AlVO_4$ peak positions from reference [22]).

appearance of the hcp phase, the peak pattern of the V containing coatings differ from the single fcc phase coating $Al_{0.71}Cr_{0.29}N$ [21] which also hold for 500°C tests.

Major changes in the wear track can be found at a testing temperature of 700°C. Up to a V concentration of 0.16, weakly crystalline iron oxides Fe_2O_3 (hematite) and Fe_3O_4 (magnetite) were formed in the wear track. Depth measurements of the wear track resulted in values close to the coating thickness for $x_V \leq 0.16$, thus indicating a partial removal of the coating and oxidation of the steel substrate. Also, the diffusion of iron atoms to the surface along column boundaries or underdense areas near to droplets [23], due to the reduced thickness of the remaining coating, can lead to the formation of iron oxides. The situation changes when the V content increases further. The wear track surface layer of $Al_{0.68}Cr_{0.10}V_{0.22}N$ could not be unambiguously clarified, but there is no clear evidence for formation of hematite or magnetite. In case of $x_V = 0.28$, the formation of the Magnéli phase oxide V_2O_5 can be confirmed by Raman spectroscopy (see Fig.6). Additional peaks with increasing intensity in the high-wavenumber range from 800 to 1000 cm^{-1} suggest also the presence of $AlVO_4$ [22] in the wear track. In contrast, the Cr-free coating revealed the most pronounced iron oxide peaks after tribological testing at 700°C indicating the most severe removal of the coating in the wear track compared to all other tested coatings within this study.

Applying optical profilometry to the wear tracks after tribological testing, the wear volume and the wear coefficient can be calculated (Fig.7). At room temperature the lowest value of $2.3 \cdot 10^{-16}$m^3/Nm was found for $x_V = 0$. The increase of the V content leads to an increase in the wear coefficient if $x_V \leq 0.22$. Higher amounts of V result in a slight reduction of wear.

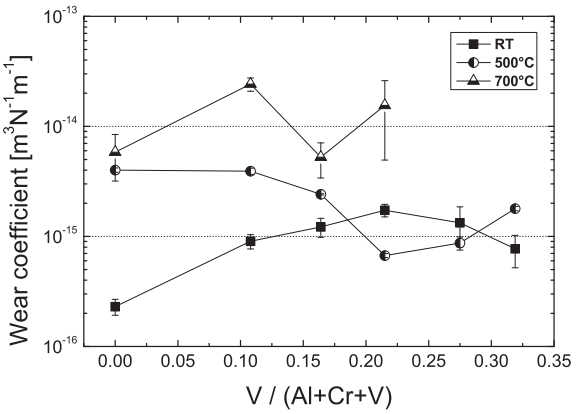

Figure 7: Calculated wear coefficient at different tribological testing temperatures dependent on V concentration in the coatings. Interconnecting lines are for better orientation.

The tribological tests at elevated temperatures reveal a different behaviour. The wear coefficient of the V-free coating rises approximately one order of magnitude [12]. In contrast to RT, at 500°C the wear reduces with increasing V concentration. While for $x_V = 0.22$ the maximum wear was found for RT, the wear coefficient reaches a minimum at 500°C and is actually lower than the RT value. The two coatings with the highest V amount show a slightly higher wear. At the highest testing temperature of 700°C there is no clear trend identifiable. The scattering of the measurement increases due to non-uniform material removal during the sliding tests and the wear coefficient represents a combination of coating and substrate wear if the coating was worn-through. If $x_V \geq 0.28$, no wear coefficients could be calculated because of melting and subsequent recrystallisation of the surface layer (Fig.8) as seen by the formation of dendritic crystallites during solidification of V_2O_5.

4 Discussion

The evolution of the mechanical properties hardness, Young's modulus and biaxial stress can be correlated with the coating structure. As the hcp phase fraction is rising with increasing V content the coating becomes softer and reveals a lower compressive stress. The transition from a metastable single phase state to more stable states with several phases leads to stress relaxation in the coating. There are slight differences in the behaviour if only small amounts of V are present, but all three properties indicate a saturation for the highest V concentrations. Since the mechanical properties mainly determine the wear of the tribological tests at RT, these results can be explained by the coating structure. Low hardness and

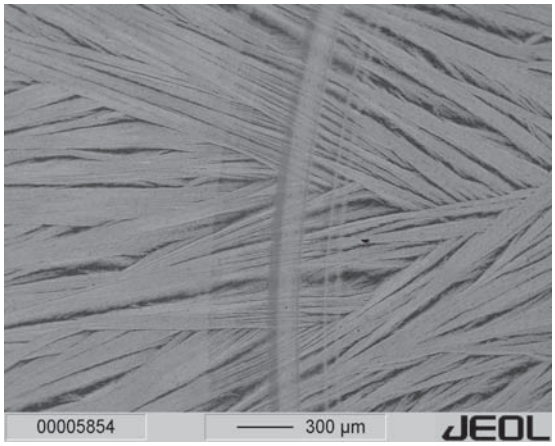

Figure 8: Wear track of $Al_{0.67}Cr_{0.05}V_{0.28}N$ after tribological test at 700°C. Backscattered electron SEM image.

coating stress lead to a maximum wear rate of $1.7 \cdot 10^{-15} m^3/Nm$ for $x_V = 0.22$. This is the coating that revealed the highest hcp phase fraction (see Fig.2).

A different situation was found when the temperature during tribological testing is increased. Here, the results are influenced by the oxidation behaviour and diffusion of V [24] rather than the structure and the mechanical properties as discussed before. At 500°C the minimum wear can be found for $x_V = 0.22 \ldots 0.28$. In this x_V range the hcp phase fraction has already reached a maximum leading to less advantageous mechanical properties. However, the wear rate correlates well with the friction coefficient that reaches a minimum in the same range.

A comprehensive discussion of the results of tribological testing at 700°C is not possible because of lacking wear data due to surface melting (see Fig.8). But it is evident, that the oxidation of V and the melting of V_2O_5 on the coating surface has a beneficial influence on the friction behaviour. In the case of $x_V = 0.28$, the COF drops from 0.7-0.8 at RT to 0.2 at 700°C. Raman measurements in the wear track clearly indicate the formation of the Magnéli phase oxide V_2O_5 which is the most stable one from the series V_nO_{3n-1} in this temperature range. V_2O_5 exhibits a bulk melting temperature of 685°C [25]. A transition to the lower-oxidised vanadium oxide VO_2 with a higher melting temperature could not be observed [16, 26]. But even before melting, the vanadium oxides are assumed to reduce the friction due to the formation of Magnéli phases with easily activated crystallographic shear planes [14]. Although these oxides could not be identified by Raman measurements (except V_2O_5), the formation of these phases in the tribo-chemical contact can explain the reduction of the COF at high-temperature testing. The influence of $AlVO_4$ formed in the wear track during the tests could not be clarified. In comparable tribological tests in the system Ti-Al-V-N the appearance of this oxide could be confirmed as well [17]. However, it can be summarised that in the sliding contact of the coating with $x_V = 0.28$ the Magnéli phase V_2O_5 and $AlVO_4$ are formed. And, assuming the formation of a protective alumina scale analogous to AlCrN [10, 11], the high-temperature sliding contact is essentially alumina vs. alumina with the Magnéli phase oxide V_2O_5 present as a third body.

5 Conclusion

Within this work, the influence of the V content on structure and properties of AlCrVN coatings deposited by arc-evporation has been studied. The evolution of the mechanical properties of V alloyed AlCrN coatings is directly related to structural changes. The appearance of a hexagonal phase causes a reduction in hardness and coating stress. The maximum hexagonal phase fraction of app. 35 wt.% for $x_V \geq 0.22$ correlates well with the hardness (app. 20 GPa) and stress (app. -900 MPa) minima as compared to the V-free coating $Al_{0.71}Cr_{0.29}N$ showing hardness and stress values of 28 GPa and -1700 MPa, respectively. This results in maximum wear for $Al_{0.68}Cr_{0.10}V_{0.22}N$ in tribological testing at room temperature.

When the testing temperature is increased up to 700°C, friction and wear are mainly determined by oxidation and diffusion of V. The best friction performance was found for $Al_{0.67}Cr_{0.05}V_{0.28}N$. Due to the formation and melting of V_2O_5 on the surface, the coefficient of friction could be reduced from 0.7 at room temperature to 0.2 at 700°C. The minimum wear at high temperatures was found for $Al_{0.68}Cr_{0.10}V_{0.22}N$ at 500°C with an improval in the wear coefficient compared to its RT value and to $Al_{0.71}Cr_{0.29}N$ which is higher by one order of magnitude.

In summary, the incorporation of V into AlCrN has been proven to beneficially influence the intermediate to high-temperature friction making it a promising candidate for tribological applications in this temperature range.

Acknowledgement

Financial support by the Christian Doppler Research Association is highly acknowledged.

References

[1] G. Fox-Rabinovich, B. Beake, J. Endrino, S. Veldhuis, R. Parkinson, L. Shuster, and M. Migranov, Surf. Coat. Technol. **200**, 5738 (2006).
[2] J. Endrino, G. Fox-Rabinovich, and C. Gey, Surf. Coat. Technol. **200**, 6840 (2006).
[3] O. Knotek, F. Loeffler, and H.-J. Scholl, Surf. Coat. Technol. **45**, 53 (1991).
[4] J. Vetter, E. Lugscheider, and S. Guerreiro, Surf. Coat. Technol. **98**, 1233 (1998).
[5] M. Kawate, A. Kimura, and T. Suzuki, J. Vac. Sci. Technol. A **20**, 569 (2002).
[6] A. Reiter, V. Derflinger, B. Hanselmann, T. Bachmann, and B. Sartory, Surf. Coat. Technol. **200**, 2114 (2005).
[7] A. Sugishima, H. Kajioka, and Y. Makino, Surf. Coat. Technol. **97**, 590 (1997).
[8] Y. Makino and K. Nogi, Surf. Coat. Technol. **98**, 1008 (1998).
[9] W. Münz, J. Vac. Sci. Technol. A **4**, 2717 (1986).
[10] M. Kawate, A. Hashimoto, and T. Suzuki, Surf. Coat. Technol. **165**, 163 (2003).
[11] O. Banakh, P. Schmid, R. Sanjinés, and F. Lévy, Surf. Coat. Technol. **163-164**, 57 (2003).
[12] R. Franz, B. Sartory, R. Kaindl, R. Tessadri, A. Reiter, V. Derflinger, P. Polcik, and C. Mitterer, in *16th International Plansee Seminar*, edited by G. Kneringer, P. Rödhammer, and H. Wildner (Reutte, Austria, 2005), vol. 2, pp. 932–945.

[13] A. Magnéli, Acta Crystallogr. **6**, 495 (1953).
[14] M. Woydt, A. Skopp, I. Dörfel, and K. Witke, Wear **218**, 84 (1998).
[15] A. Erdemir, Tribol. Lett. **8**, 97 (2000).
[16] G. Gassner, P. Mayrhofer, K. Kutschej, C. Mitterer, and M. Kathrein, Tribol. Lett. **17**, 751 (2004).
[17] P. Mayrhofer, P. Hovsepian, C. Mitterer, and W.-D. Münz, Surf. Coat. Technol. **177-178**, 341 (2004).
[18] K. Kutschej, P. Mayrhofer, M. Kathrein, P. Polcik, and C. Mitterer, Surf. Coat. Technol. **188-189**, 358 (2004).
[19] M. Kathrein, C. Michotte, M. Penoy, P. Polcik, and C. Mitterer, Surf. Coat. Technol. **200**, 1867 (2005).
[20] P. Mayrhofer and C. Mitterer, Surf. Coat. Technol. **133-134**, 131 (2000).
[21] R. Kaindl, R. Franz, J. Soldan, A. Reiter, P. Polcik, C. Mitterer, B. Sartory, R. Tessadri, and M. O'Sullivan, Thin Solid Films **515**, 2197 (2006).
[22] V. Brázdová, M. Ganduglia-Pirovano, and J. Sauer, J. Phys. Chem. B **109**, 394 (2005).
[23] A. Hörling, L. Hultman, M. Odén, J. Sjölén, and L. Karlsson, J. Vac. Sci. Technol. A **20**, 1815 (2002).
[24] J. Endrino and V. Derflinger, Surf. Coat. Technol. **200**, 988 (2005).
[25] N. Greenwood and A. Earnshaw, *Chemistry of the Elements* (Butterworth-Heinemann, Oxford, 1997), 2nd ed.
[26] Y. Ningyi, L. Jinhua, and L. Chenglu, Appl. Surf. Sci. **191**, 176 (2002).

Publication III

Micro- and bonding structure of arc-evaporated AlCrVN hard coatings

R. Franz, J. Neidhardt, B. Sartory, R. Tessadri, C. Mitterer

Thin Solid Film, submitted (2007)

Micro- and bonding structure of arc-evaporated AlCrVN hard coatings

R. Franz[a], J. Neidhardt[a], B. Sartory[b], R. Tessadri[b], C. Mitterer[a]

[a] *Christian Doppler Laboratory for Advanced Hard Coatings at the Department of Physical Metallurgy and Materials Testing, University of Leoben, Franz-Josef-Strasse 18, A-8700 Leoben, Austria*
[b] *Institute for Mineralogy and Petrography, University of Innsbruck, Innrain 52, A-6020 Innsbruck, Austria*

The incorporation of V into metastable cubic AlCrN coatings triggers the separation in a face-centered cubic (fcc) and a hexagonal wurtzite type phase whereas by using higher energetic growth conditions (ion energy), the metastable single-phase fcc structure can be retained. However, no preferential enrichment of V in either one of the phases was found by TEM. Independently from structural changes, the nitrides in all investigated coatings are in solid solution without any intermetallic compounds as it is shown by XPS, a detailed deconvolution of the measured core level spectra is presented.

KEY WORDS: hard coatings; AlCrVN; arc evaporation; XPS

1 Introduction

Commercially available AlCrN wear protective coatings offer high hardness [1–3], good oxidation resistance [4, 5] and thermal stability [6, 7]. As the need for reducing the use of lubricants in cutting applications is rising, cutting with minimised amounts of coolants or dry cutting offer feasible alternatives. However, the relatively high friction of the common hard coatings especially at elevated temperatures leads, under these conditions, to even higher thermal loads at the cutting edge. Alternatively, the formation of Magnéli phase oxides in this temperature range can provide a lubricious effect [8, 9] and, thus, help to reduce the energy dissipated in the tribological contact. The beneficial effect could be demonstrated in high-temperature tribological testing of oxidised VN [10, 11], but early coating failure due to massive oxidation occurred. In order to fulfil the high demands for industrial applications, V was incorporated into AlCrN offering the necessary combination of intrinsic mechanical and tribological properties [12]. A similar concept, namely the incorporation of V into TiAlN as multilayer system or solid solution, has been successfully applied in Refs. [13–15] . When V is alloyed to AlCrN, the formation of a phase with the hexagonal wurtzite type (w) structure of AlN in the otherwise face-centered cubic (fcc) AlCrN could be observed in Ref. [12] causing a congruent deterioration of the mechanical properties. However, details of the micro- and bonding structure remain largely unexplored. This work, therefore, intents to address the relation between growth conditions and several structural aspects of AlCrVN hard coatings and as such gives more insight into the micro- and bonding structure of AlCrVN hard coatings. In addition, a way to inhibit the disadvantageous phase separation is presented.

2 Experimental

Al-Cr-V-N coatings were synthesised in a commercial arc-evaporation system (Oerlikon Balzers RCS) with a base pressure below 4×10^{-3} Pa. The substrates, high-speed steel

(DIN 1.3343, AISI M2) coupons (⊘ 30 mm × 10 mm), cemented carbide cutting inserts (grade 10), and silicon stripes (Si (100)), were heated to 500°C and etched in a pure Ar plasma with ions extracted from an additional arc discharge. During deposition, the substrate bias voltage was set to constant values ranging from -40 V to -150 V whereas the N_2 gas pressure was regulated to 3.5 Pa. 4 arc-sources were current-controlled at 140 A and equipped with powder-metallurgically produced $Al_{0.70}Cr_{0.30-x}V_x$ targets with compositions of $x = 0, 0.1, 0.15, 0.2, 0.25$, and 0.3. The targets exhibit a homogeneous erosion behaviour at industrially competitive deposition rates of ∼50 nm/min on two-fold rotating substrates.

The chemical composition of the resulting coatings was determined by electron probe microanalysis (EPMA) by means of wavelength-dispersive X-ray spectroscopy (WDX) using a JEOL JXA 8100 Superprobe under an acceleration voltage of 10 kV and an analysed spot size of ∼40 μm × 40 μm. X-ray diffraction (XRD) data for analysing the crystal structure were obtained by a D8 diffractometer from Bruker AXS with parallel beam geometry equipped with a Cu-ceramic tube and an energy-dispersive detector (SolX from Bruker AXS) via $\theta - 2\theta$ scans. Here, the TOPAS software package was applied for Rietveld refinement of the XRD patterns. Insights into the microstructure of the coatings were provided by a FEI Tecnai F20 transmission electron microscope (TEM). X-ray photoelectron spectroscopy (XPS) was applied to study the chemical bonding structure using an Omicron Multiprobe system with a monochromised Al K_α beam of 1486.6 eV with a resolution < 0.5 eV. Prior to the measurement, the samples were heated in situ to 350°C to desorb volatile surface contaminants. This procedure was preferred to the common sputter cleaning as the initial surface bonding structure is retained. The resulting core level spectra were fitted with Unifit 2002 [16]. Hardness measurements were conducted using a H100C Fischerscope equipped with a Vickers indenter in the constant-depth mode of 300 nm. The tip shape was calibrated via the built-in procedures using single crystalline sapphire (100). The biaxial stress state was determined by means of the cantilever beam bending technique of Si stripes (20 mm × 7 mm × 0.525 mm) according to Ref. [17].

3 Results and discussion

3.1 Crystal structure evolution

All deposited coatings are well adherent and show a dark greyish colour. The nitrogen concentration measured by EPMA was stoichiometric and constant at ∼50 at.% for all coatings regardless the different bias voltages, whereas the metal ratios roughly mirror the respective target compositions. Only a minor Al deficiency of 2-3 at.%, presumably due to gas scattering, leads to an apparent slight increase in Cr and V concentrations. Structural investigations by means of XRD depending on the V content in the coating have been published in Ref. [12], where the formation of a phase with w-AlN structure was found as soon as V was added to the metastable fcc-$Al_{0.71}Cr_{0.29}N$ solid solution. There, Cr was substituted stepwise by V. According to Rietveld refinement of the XRD data, the maximum w-AlCrN phase fraction of app. 35 wt.% was reported for $Al_{0.68}Cr_{0.10}V_{0.22}N$ deposited at -40 V.

The effect of the ion energy on the micro- and bonding structure of AlCrVN is subject of this study. Hence, Figure 1 shows the dependence of the formation of crystalline phases on

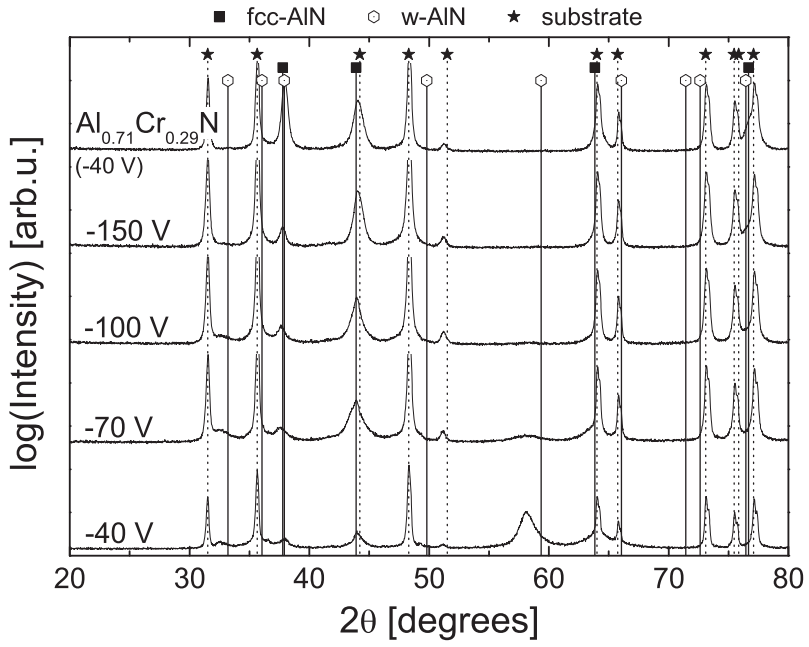

Figure 1: XRD patterns of $Al_{0.68}Cr_{0.10}V_{0.22}N$ coatings deposited at different bias voltages. $Al_{0.71}Cr_{0.29}N$ (bias: -40 V) is given as reference.

the applied bias voltage.

As reported, at a voltage of -40 V the dual-phase structure of $Al_{0.68}Cr_{0.10}V_{0.22}N$ can be clearly observed whereas at the maximum bias of -150 V the pattern is similar to $Al_{0.71}Cr_{0.29}N$ which serves as a reference for single-phase fcc-AlCrN structure. A quantification by Rietveld refinement in Figure 2 confirms the apparent decrease of the w-AlCrN phase fraction with increasing bias voltage.

The decrease is almost linear and even at a V concentration of $x \sim 0.2$ and a accompanied Al/Cr ratio of ~ 7, a single-phase coating with fcc-AlCrN structure can be restored alongside with the associated superior mechanical properties and oxidation resistance as compared to w-AlCrN [3, 6]. The existence of a significant amorphous phase fraction is highly unlikely as the typically raised background in the XRD pattern due to the short-range order in amorphous phases is absent. Further, the development of the crystallite size as obtained by XRD supports this notion. In the steady-state growth, a crystallite size for the w-AlCrN grains of 8–10 nm for all coatings deposited at -40 V bias voltage is obtained, whereas the size of the crystallites with fcc-AlCrN structure is in the range of 10–20 nm. Increasing the bias voltage up to -150 V results, however, in an increase of the fcc-AlCrN crystallite size to 30–40 nm while the w-AlCrN grains reduce slightly to ∼6 nm for bias voltages of -70 and -100 V before they vanish at -150 V. The formation of an amorphous phase would, however, disturb the crystal growth and should result in a constant renucleation leading to a decreased crystallite size. The presence of an amorphous phase is, therefore, highly unlikely.

Investigations of the stress state might provide an explanation for the stabilisation of

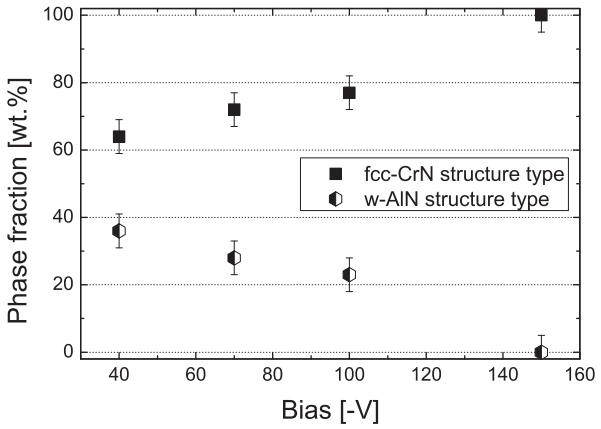

Figure 2: Phase fractions depending on the applied bias voltage as obtained by Rietveld refinement of the XRD patterns (coating: $Al_{0.68}Cr_{0.10}V_{0.22}N$).

the metastable fcc structure at higher bias voltages. It is known that higher ion energies cause higher defect densities in the crystal structure which manifest themselves in higher compressive stress states and in turn lead to an increase in hardness [18]. As shown in Figure 3, the compressive stress of $Al_{0.68}Cr_{0.10}V_{0.22}N$ triples from -1 GPa to -3 GPa for bias voltages of -40 V to -150 V.

Due to this strong increase in compressive stress the metastable fcc crystal structure might be energetically favoured as it presents a by ∼25% higher density compared to a wurtzite type structure. Further, higher energetic growth conditions stimulate adatom diffusion and collisional mixing at the growth front [19] whereas higher defect densities lower the adatom migration [20] and, thus, might hinder the rearrangement of the already deposited atoms. Mayrhofer et al. have shown that the distribution of the Al atoms in TiAlN significantly influences the metastable solubility limit of AlN in fcc-TiN [21]. A specific estimation of the influence of the above mentioned mechanims goes beyond the focus of this work, but it may be speculated, that these mechanisms counteract the (adatom mobility driven) phase separation and beneficially influence the stabilisation of the metastable fcc-AlCrN phase as it was experimentally verified by XRD within the range of applied bias voltages. However, the transformation of the mechanically less favourable w-AlCrN phase fraction into a single-phase fcc-AlCrN structure results in an additional increase in hardness. Thus, hardness values comparable to $Al_{0.71}Cr_{0.29}N$ are reached at the maximum bias of -150 V (see Figure 3) where the crystal structure of $Al_{0.71}Cr_{0.29}N$ could be restored [12].

3.2 TEM

TEM cross-section images of $Al_{0.68}Cr_{0.21}V_{0.11}N$ deposited at -40 V bias voltage reveal a dense microstructure as it can be seen in Figure 4. Following the development of the crystallite size from the substrate to the coating surface, an increase in grain size can be noticed which is attributed to a transition from the nucleation phase to steady-state growth. In this steady-

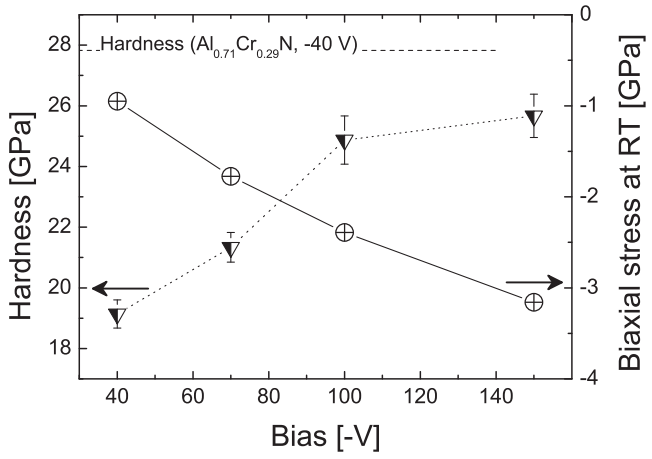

Figure 3: Hardness and biaxial coating stress of as-deposited $Al_{0.68}Cr_{0.10}V_{0.22}N$ coatings in dependence on bias voltage. The values for the $Al_{0.71}Cr_{0.29}N$ coating deposited at a bias voltage of -40 V were taken from Ref. [12]. (Interconnecting lines are for better orientation.)

state growth region, the crystallites are of elongated shape revealing nano-columnar structure with a width in the range of 10–20 nm.

The question whether V is preferentially incorporated in the cubic or wurtzite phase, which might provide for indications about its effect on the respective phase stability, was addressed by energy-filtered TEM. Here, the elemental distribution of V can be analysed by taking the jump ratio between two energy ranges below and above the V L absorption edge [22]. For the investigations at an appropriate resolution, an area of steady-state growth near the film surface of $Al_{0.68}Cr_{0.10}V_{0.22}N$ was chosen as shown by the bright-field image in Figure 5a.

The corresponding selected area electron diffraction (SAED) pattern in Figure 5b confirms the dual-phase structure of the investigated zone. Further, the in Figure 5c presented homogeneous V distribution indicated, however, no preferential enrichment of V in either fcc-AlCrN or w-AlCrN grains or grain boundaries within the resolution limits and it can be inferred, that V is incorporated substitutionally into the crystal lattice similarly to Cr, while Cr atoms are most likely substituted by V atoms. This substitution can explain the appearance of a w-AlN structured phase as the metastable solubility limit of AlN in fcc-VN is slightly lower than in fcc-CrN according to Ref. [23].

3.3 XPS

More insights into the bonding structure of AlCrVN can be provided by XPS as it addresses primarily the nearest neighbour configuration. Here, all relevant core level spectra, namely N1s, Al2p, Cr2p, and V2p, for the whole investigated composition range and a bias voltage of -40 V have been analysed as well as two coatings, $Al_{0.68}Cr_{0.10}V_{0.22}N$ and $Al_{0.67}Cr_{0.05}V_{0.28}N$, deposited at -150 V. The N1s spectra of all coatings deposited at -40 V are shown in Figure 6.

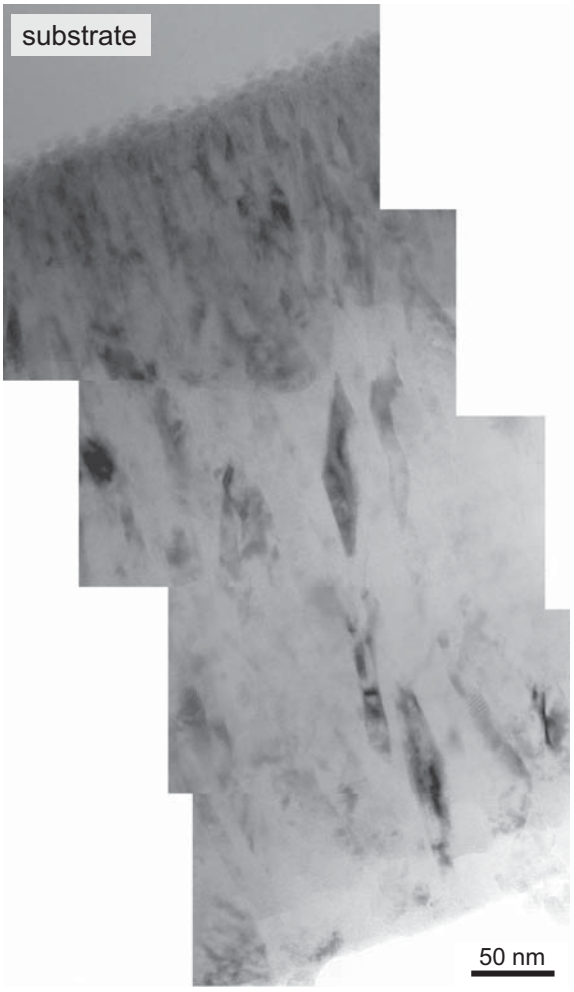

Figure 4: Cross-sectional TEM bright-field image of $Al_{0.68}Cr_{0.21}V_{0.11}N$ (bias: -40 V) over the whole coating thickness.

From the three contributions, that can be deconvoluted, the subpeak in the low-energy region was assigned to surface contamination, since, similar to Ref. [26], it vanished after sputter cleaning with 2 keV Ar ions. A straightforward labelling of the other subpeaks is not possible as only a few references for Al-N, Cr-N and V-N as bulk or coating material were found. Therefore, a thorough analysis of the N1s spectra has been performed. In Refs. [24, 25] all published binding energies E_b for N-Al and N-Cr are in the range 396.2–396.8 eV, except for Taylor et al. [27] who obtained $E_b = 397.3$ eV for N-Al. This energy would overlap with contributions from N-V ($E_b = 397.2 - 397.4$ eV [25]) and N-Cr in Cr_2N configuration ($E_b = 397.2 - 397.6$ eV [24, 25]). Structural analyses by XRD gave no evidence for a Cr_2N phase and this contribution can, therefore, be excluded. The increasing intensity of the subpeak at higher E_b values in Figure 6 for higher V content suggests an assignment of this contribution to N-V bonds while the subpeak at intermediate E_b values seems to be exclusively attributed to N-(Al,Cr) bonds with an indistinguishable binding energy overlap. In order to verify the chosen peak assignment, the peak area ratio between N-V and the sum of N-(Al,Cr) and N-V has been calculated for all different coatings as shown in Figure 7.

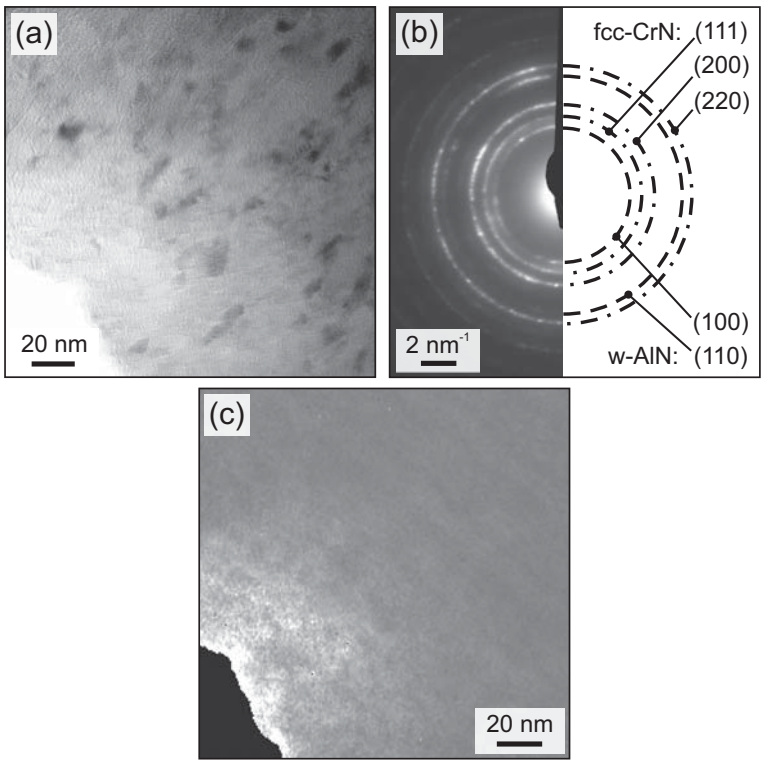

Figure 5: (a) TEM bright-field image and (b) SAED pattern of the investigated zone near the surface of $Al_{0.68}Cr_{0.10}V_{0.22}N$ deposited at a bias voltage of -40 V. The sample thickness ranges from ∼15-40 nm. (c) Energy-filtered TEM (jump ratio) for V contrast (drift corrected).

This ratio represents the coating composition near the surface and is, therefore, compared to the respective target ratios. For the coatings deposited at -40 V bias voltage, both values show a good agreement and the validity of the chosen peak assignment (indicated in Figure 6) as well as the measured coating composition by EPMA is supported.

No changes in the N1s core level spectra are, however, observed for the transition from a dual-phase (fcc-AlCrN + w-AlCrN) towards a single-phase (fcc-AlCrN) crystal structure. As exemplified by XRD investigations of $Al_{0.68}Cr_{0.10}V_{0.22}N$, the formation of a w-AlCrN phase can be inhibited by higher energetic growth conditions. The measured N1s spectra for the bias voltages of -40 and -150 V reveal neither significant differences in the intensity and position of the fitted subpeaks (see Figure 8) nor the calculated peak area ratio (see Figure 7). A similar result is obtained for $Al_{0.67}Cr_{0.05}V_{0.28}N$. This can be understood by the similar nearest neighbour bonding configuration of the fcc and wurtzite crystal strutcure where only the stacking order of the atom sheets differs.

As for the metallic constituents, the results of the core level spectra Al2p, Cr2p and V2p measured on $Al_{0.68}Cr_{0.10}V_{0.22}N$ as shown in Figure 8 will serve as an example. Yet again, there are no significant differences between the spectra measured for the coatings synthesised at different bias voltages. In case of Al2p, the core level spectrum consists of two contributions. The subpeak at lower E_b values but with higher intensity lies, as expected, within the Al-N binding energy range of 73.8–74.4 eV [28, 29]. As the sample was not sputter-cleaned prior

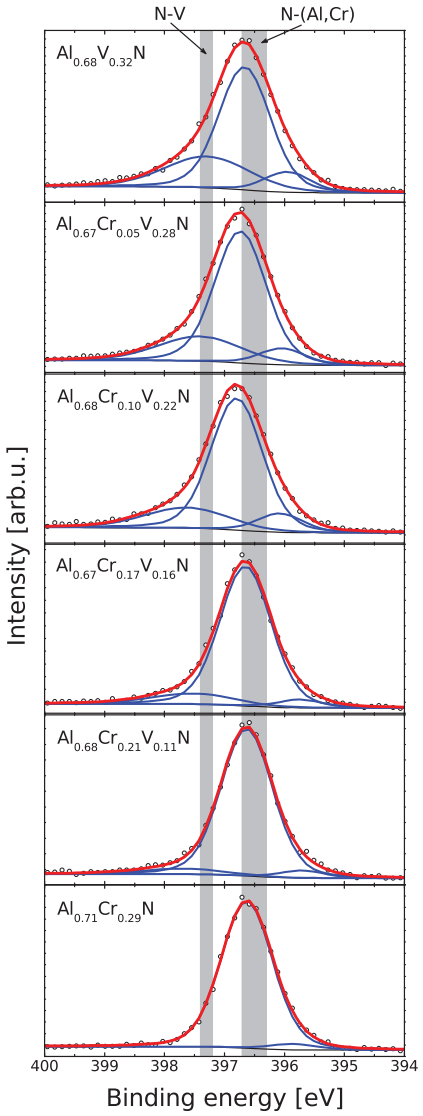

Figure 6: N1s XPS core level spectra of AlCrVN coatings (bias: -40 V) with fitted subpeaks. Relevant binding energy ranges are given according to Refs. [24, 25].

to analysis, surface oxides are present and the subpeak at higher E_b is, therefore, assigned to Al-O bonds ($E_b = 74.0 - 74.7$ eV [29, 30]) due to the higher electronegativity of oxygen. At a binding energy of 74.4 eV [31], the Cr3s peak should also contribute in this range, but since the Cr/Al ratio of $\sim$1/7 is small, its contribution can be neglected.

Continuing with Cr2p and V2p, the separation in energy between the 2p1/2 and 2p3/2 core level spectra due to spin-orbit coupling is noticeable. Fitting these peaks, again two contributions have to be considered as it was the case for Al2p. The subpeak at lower E_b can be assigned to Me-N bonds (Cr-N: $E_b = 575.5 - 575.8$ eV [30, 32, 33], V-N: $E_b = 514.1 - 514.4$ eV [28, 30, 34]) while the other contribution in the spectra are due to Me-O

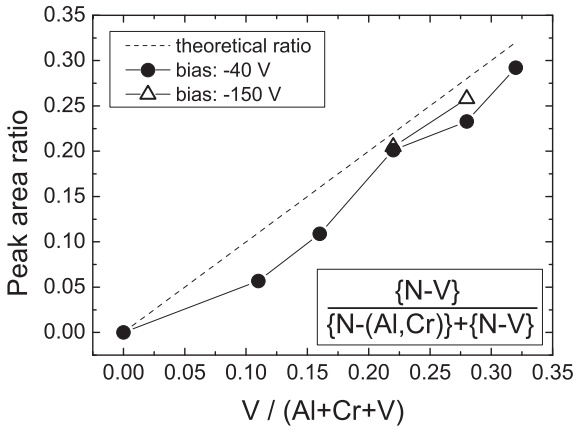

Figure 7: Peak area ratio of nitrogen-metal bonds in N1s signal representing coating composition in the near surface region. Theoretical compositions are according to the targets used for deposition. (Interconnecting lines are for better orientation.)

bonds (Cr-O: $E_b = 576.5 - 576.8$ eV [30, 32]). In case of V-O, two configurations have to be considered (V_2O_5: $E_b = 517.0 - 517.5$ eV [28, 30, 35], VO_2: $E_b = 515.5 - 515.8$ eV [30, 35]). In general, surface oxides can beneficially influence the coating properties. A thermodynamically stable mixed Al_2O_3-Cr_2O_3 scale hinders oxygen diffusion into the coating due to its dense microstructure [36], whereas the formation of V_2O_5 offers lubricious effects at elevated temperatures [12].

All three investigated metall core level spectra are not influenced by the bias voltage, except for the apparent deviation of the intensity ratios in the Cr2p spectra indicating a reduced formation of chromium oxides on the coating deposited at -150 V bias. However, as the bonding structure of V remains unchanged regardless the difference in crystal structure, a homogeneous V distribution can be assumed. This fact supports the findings by energy-filtered TEM.

Another important aspect within the XPS investigations is the absence of contributions due to Me-Me bonds which should appear at low binding energies (Al-Al: $E_b = 72.3 - 72.9$ eV [30], Cr-Cr: $E_b = 574.0 - 574.3$ eV [30, 32], V-V: $E_b = 512.0 - 512.3$ eV [28, 30]). The presence of intermetallic compounds can, therefore, be excluded. Since all metal atoms are bonded predominantly to nitrogen independent from the applied bias voltage and the manifested structural changes, the coatings have to be seen as solid solution of various nitrides as it was already suggested by the via EPMA established stoichiometry.

4 Conclusions

In conclusion, it can be stated that the incorporation of V into AlCrN coatings lowers the apparent metastable solubility limit of AlN in face-centered cubic CrN and, thus, triggers a phase separation into fcc-CrN and w-AlN structured grains. Within the TEM resolution

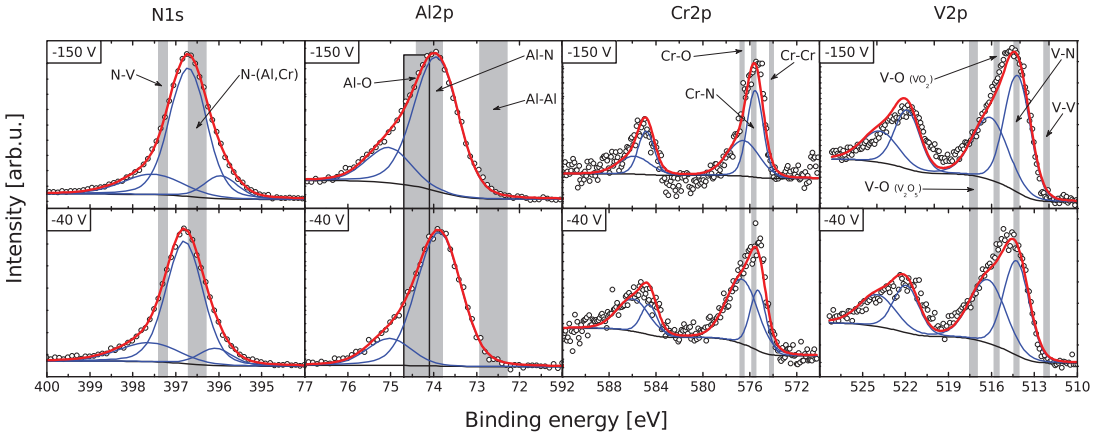

Figure 8: XPS core level spectra with fitted subpeaks of $Al_{0.68}Cr_{0.10}V_{0.22}N$ deposited at different bias voltages. Relevant binding energy ranges are given according to Refs. [24, 25, 32, 35]

limit, no preferential enrichment of V in either type of grains or at grain boundaries could be detected. Higher ion energies provided by higher bias voltages during deposition affect the solubility and single-phase Al-Cr-V-N coatings with fcc-CrN structure can be restored. Here, the chemical bonding structure remains unaltered supporting the finding of a homogeneous V distribution. Independently from phase changes and different compositions, all coatings are solid solutions without any intermetallic compounds. A detailed analysis of the N1s core level spectra allowed for an assignment of the different contributions due to N-V and N-(Al,Cr) bonds.

Acknowledgments

The authors are grateful to Werner Grogger and Christian Gspan (Austrian Centre for Electron Microscopy and Nanoanalysis, Graz) for TEM investigations and to Alexander Fian (Institute of Nanostructured Materials and Photonics, Weiz, Austria) for XPS measurements. Financial support by the Christian Doppler Research Association within the framework of the CD lab 'Advanced Hard Coatings' with its partners Plansee GmbH (Lechbruck, Germany) and Oerlikon Balzers Coatings AG (Balzers, Liechtenstein) is highly acknowledged.

References

[1] O. Knotek, F. Loeffler, and H.-J. Scholl, Surf. Coat. Technol. **45**, 53 (1991).
[2] J. Vetter, E. Lugscheider, and S. Guerreiro, Surf. Coat. Technol. **98**, 1233 (1998).
[3] M. Kawate, A. Kimura, and T. Suzuki, J. Vac. Sci. Technol. A **20**, 569 (2002).

[4] O. Banakh, P. Schmid, R. Sanjinés, and F. Lévy, Surf. Coat. Technol. **163-164**, 57 (2003).
[5] M. Kawate, A. Hashimoto, and T. Suzuki, Surf. Coat. Technol. **165**, 163 (2003).
[6] A. Reiter, V. Derflinger, B. Hanselmann, T. Bachmann, and B. Sartory, Surf. Coat. Technol. **200**, 2114 (2005).
[7] H. Willmann, P. Mayrhofer, P. Persson, A. Reiter, L. Hultman, and C. Mitterer, Scripta Mater. **54**, 1847 (2006).
[8] M. Woydt, A. Skopp, I. Dörfel, and K. Witke, Wear **218**, 84 (1998).
[9] A. Erdemir, Tribol. Lett. **8**, 97 (2000).
[10] G. Gassner, P. Mayrhofer, K. Kutschej, C. Mitterer, and M. Kathrein, Tribol. Lett. **17**, 751 (2004).
[11] N. Fateh, G. Fontalvo, G. Gassner, and C. Mitterer, Wear **262**, 1152 (2007).
[12] R. Franz, J. Neidhardt, B. Sartory, R. Kaindl, R. Tessadri, P. Polcik, V. Derflinger, and C. Mitterer, Tribol. Lett. **23**, 101 (2006).
[13] W.-D. Münz, L. Donohue, and P. Hovsepian, Surf. Coat. Technol. **125**, 269 (2000).
[14] P. Mayrhofer, P. Hovsepian, C. Mitterer, and W.-D. Münz, Surf. Coat. Technol. **177-178**, 341 (2004).
[15] K. Kutschej, P. Mayrhofer, M. Kathrein, P. Polcik, and C. Mitterer, Surf. Coat. Technol. **188-189**, 358 (2004).
[16] U. Software, *http://www.uni-leipzig.de/∼unifit/* (12/2006).
[17] P. Mayrhofer and C. Mitterer, Surf. Coat. Technol. **133-134**, 131 (2000).
[18] P. Mayrhofer, F. Kunc, J. Musil, and C. Mitterer, Thin Solid Films **415**, 151 (2002).
[19] J. E. Greene, J. Vac. Sci. Technol. A **5**, 1947 (1987).
[20] J.-E. Sundgren, Thin Solid Films **128**, 21 (1985).
[21] P. Mayrhofer, D. Music, and J. Schneider, J. Appl. Phys. **100**, 094906 (2006).
[22] G. Kothleitner, M. Rogers, A. Berendes, W. Bock, and B. Kolbesen, Appl. Surf. Sci. **252**, 66 (2005).
[23] Y. Makino, ISIJ Int. **38**, 925 (1998).
[24] La Surface database, *http://www.lasurface.com/accueil/*.
[25] NIST database, *http://srdata.nist.gov/xps/*.
[26] J. Neidhardt, Z. Czigány, B. Sartory, R. Tessadri, M. O'Sullivan, and C. Mitterer, Acta Mater. **54**, 4193 (2006).
[27] J. A. Taylor and J. W. Rabalais, J. Chem. Phys. **75**, 1735 (1981).
[28] D. Briggs and M. P. Seah, *Practical surface analysis*, vol. 1 (John WILEY & SONS, 1993), 2nd ed.
[29] G. McGuire, G. Schweitzer, and T. Carlson, Inorg. Chem. **12**, 2450 (1973).
[30] C. D. Wagner, W. M. Riggs, L. E. Davis, and J. F. Moulder, *Handbook of X-ray photoelectron spectroscopy* (Perkin-Elmer Corporation (Physical Electronics), 1979).
[31] S. K. Kulkarni, M. G. Thube, and A. S. Nigavekar, Phys. Rev. B **37**, 6723 (1988).
[32] A. Lippitz and T. Hübert, Surf. Coat. Technol. **200**, 250 (2005).
[33] O. Nishimura, K. Yabe, and M. Iwaki, J. Electron. Spectrosc. Relat. Phenom. **49**, 335 (1989).
[34] M. Romand and M. Roubin, Analysis **4**, 309 (1976).
[35] G. Silversmit, D. Depla, H. Poelman, G. Marin, and R. De Gryse, J. Electron. Spectrosc. Relat. Phenom. **135**, 167 (2004).

[36] A. E. Reiter, C. Mitterer, and B. Sartory, J. Vac. Sci. Technol. A **25**, 711 (2007).

Publication IV

Oxidation and diffusion processes during annealing of AlCrVN hard coatings

R. Franz, J. Neidhardt, B. Schaffer, H. Hutter, R. Kaindl, B. Sartory, R. Tessadri, M. Lechthaler, P. Polcik, C. Mitterer

Journal of Vacuum Science and Technology A, submitted (2007)

Oxidation and diffusion processes during annealing of AlCrVN hard coatings

R. Franz[a], J. Neidhardt[a], B. Schaffer[b], H. Hutter[c], R. Kaindl[d], B. Sartory[d], R. Tessadri[d], M. Lechthaler[e], P. Polcik[f], C. Mitterer[a]

[a] *Christian Doppler Laboratory for Advanced Hard Coatings at the Department of Physical Metallurgy and Materials Testing, University of Leoben, Franz-Josef-Strasse 18, A-8700 Leoben, Austria*
[b] *Research Institute for Electron Microscopy and Fine Structure Research, Graz University of Technology, Steyrergasse 17, A-8010 Graz, Austria*
[c] *Institute of Chemical Technologies and Analytics, Vienna University of Technology, Getreidemarkt 9/164, A-1060 Wien, Austria*
[d] *Institute of Mineralogy and Petrography, University of Innsbruck, Innrain 52, A-6020 Innsbruck, Austria*
[e] *Oerlikon Balzers Coating AG, Iramali 18, FL-9496 Balzers, Principality of Liechtenstein*
[f] *Plansee GmbH, Siebenbürgerstrasse 23, D-86983 Lechbruck am See, Germany*

V-alloyed AlCrN hard coatings were deposited by reactive arc-evaporation in an industrial-sized deposition system and subsequently annealed in ambient air at temperatures ranging from 500–700°C in order to study the formation mechanisms of the desired lubricious oxides. The oxidised samples were investigated by means of secondary ion mass spectrometry depth profiling, X-ray diffraction, Raman spectroscopy and analytical transmission electron microscopy. Vanadium diffusion in the oxidised part of the coating leads to the formation of a V-rich toplayer containing $AlVO_4$ and the desired lubricious oxide V_2O_5 followed by a V-depleted inner oxide layer consisting of a mixed or nanocrystalline $(Al,Cr,V)_2O_3$ on top of the intact AlCrVN coating.

KEY WORDS: hard coatings, AlCrVN, lubricious oxides, arc-evaporation

1 Introduction

Over the last years, the formation of high-temperature lubricious oxides on ceramic hard coatings has drawn much attention as to decrease the energy dissipated in the tribological contact zone. Here, Magnéli phase oxides [1] which can act as solid and liquid lubricants are of special interest [2, 3]. Tribological testing of sputtered VN revealed the formation of lubricious oxides for temperatures ≥ 500°C [4, 5]. There, oxides from the homologous series V_nO_{2n-1} could be evidenced while the low-friction effects were mainly attributed to the formation of V_2O_5. This oxide has a bulk melting temperature of 670°C [6] and coefficients of friction (COF) drop to $0.2-0.3$ at temperatures $\sim$700°C attributed to liquid lubrication. However, the massive oxidation of VN at elevated temperatures compromises the mechanical properties and results in high wear rates.

In order to design low-friction coatings applicable for industrial operations, the incorporation of V into existing state-of-the-art hard coatings synthesised by physical vapour deposition presents a successful strategy. Here, retaining an adequate mechanical integrity in combination with a controlled V out-diffusion are the requirements for the coating. Competitive wear rates were obtained via the deposition of TiAlN/VN multilayers and TiAlVN and AlCrVN solid solutions [7–10] with friction coefficients in the range of $0.2-0.4$ at 700°C. Again, the lubricious effects could be related to the formation of V_2O_5 during tribological testing at elevated temperatures. Dry sliding tests at room temperature of TiAlN/VN multilayers revealed the formation of an oxidised tribolayer with an amorphous structure, but

no V_2O_5 could be detected on the worn surface [11]. As it seems, the peak temperatures in the asperities of the tribological contact zone during dry sliding are not sufficient to form a stable V_2O_5 layer, but in cutting operations higher temperatures are commonly encountered and a pronounced reduction of friction can be expected.

The processes leading to the formation of V_2O_5 were studied in several investigations addressing the oxidation and diffusion behaviour of V containing Ti-Al-N coatings. Zhou et al. report on a two-layer structure of the oxides formed during annealing of TiAlN/VN multilayers at temperatures ≥ 600°C [12]. V_2O_5 was clearly detected at 638°C, whereas a further increase in temperature to 672°C resulted in complete oxidation. According to Lewis et al., V_2O_5 reacts with Al_2O_3 in this temperature range to form $AlVO_4$ [13]. Thus, the main compounds of the formed oxide at 670°C are TiO_2 and $AlVO_4$. Mayrhofer et al. report a reduction of V_2O_5 to VO_2 during differential scanning calorimetry measurements of TiAlN/VN multilayers up to 1200°C [8]. This reaction might explain the increase of the COF for longer durations as VO_2 exhibits a higher melting point (1967°C [6]) and therefore a back-transition from liquid to solid lubrication occurs accompanied by higher friction values. Similar observations were reported by Kutschej et al. for the investigation of the oxidation behaviour and high-temperature tribological properties of Ti-Al-V-N coatings [14].

Since AlCrN exhibits a higher oxidation resistance as compared to TiAlN [15], a beneficial influence on the oxidation behaviour of V alloyed AlCrN can be expected. Therefore, this work intends to extend the knowledge about oxide formation and diffusion processes in hard coatings during heat treatment to the system Al-Cr-V-N with an emphasis on lubricious oxide formation mechanisms. Depth profiles were measured by secondary ion mass spectrometry (SIMS) in order to gain information about diffusion processes, whereas X-ray diffraction (XRD), Raman spectroscopy and transmission electron microscopy (TEM) were applied to study the morphology and microstructure of the oxides formed.

2 Experimental

AlCrVN was synthesised in a commercial arc-evaporation system (Oerlikon Balzers RCS) with a base pressure below $4 \cdot 10^{-3}$ Pa [16]. The ultra-sonically cleaned substrates, high-speed steel coupons (DIN 1.3343, AISI M2), were heated to 500°C and etched in a pure Ar plasma with ions extracted from an additional arc discharge. During deposition a bias voltage of –40 V was applied while the N_2 gas pressure was kept constant at 3.5 Pa. 4 arc-sources were equipped with powder-metallurgically produced $Al_{0.70}Cr_{0.10}V_{0.20}$ targets and current controlled at 140 A during the deposition time of 60 min. All targets exhibit a homogeneous erosion behaviour at an industrially competitive deposition rate of ∼50 nm/min on two-fold rotating substrates.

The deposited samples were annealed in ambient atmosphere at temperatures $T = 550$, 600, 650 and 700°C. SIMS depth profiles of the oxidised coatings were obtained with a CAMECA IMS-3f using Cs^+ with an energy of 15.5 keV as primary ions for sputtering. The sputtered area was 300×300 μm while the analysis was restricted to an area in the center with a diameter of 150 μm. The SIMS depth scale was calibrated by the coating thickness measured on fracture cross-sections taken with a Zeiss EVO 50 scanning electron microscope (SEM). The deviations in the sublayer thicknesses originating from variations of the sputter rate are less than 10%. The crystallinity was investigated by means of XRD and

Raman spectroscopy. The XRD data were obtained from a D8 diffractometer from Bruker AXS with Cu-K_α radiation in parallel beam geometry and grazing incidence with an angle of 2°. Raman spectra were acquired with a HORIBA Jobin Yvon LabRam-HR800 Raman micro-spectrometer equipped with a 30 mW Ar^+ ion laser (emission line 488 nm). For TEM analysis, a cross-section of the sample annealed at 700°C was prepared by the focused ion beam (FIB) lift-out method [17] and studied on a Philips CM 20 equipped with an energy-dispersive X-ray spectroscopy (EDX) system from Noran with a HPG detector and a Gatan Imaging Filter for electron energy-loss spectroscopy (EELS). High-resolution TEM (HR-TEM) investigations were performed on a Tecnai TF 20 with a Schottky FEG cathode. The microscope is equipped with a scanning unit and a high-angle-annular-dark-field detector, a High-Resolution Gatan Imaging Filter with a 2k CCD camera and an EDX system from EDAX (Si(Li) detector). Both microscopes were operated with an acceleration voltage of 200 kV. Elemental mappings were obtained by applying the scanning TEM spectrum imaging (STEM SI) technique of recorded EELS spectra for N and O and EDX spectra for Al, Cr, V and Fe [18]. Multiple-linear-least-square (MLLS) fits were used to extract the element-specific signal from the EELS spectra [19].

3 Results

3.1 SIMS

The investigated coating with a chemical composition of $Al_{0.68}Cr_{0.10}V_{0.22}N$ as determined in a previous publication [10] is well adherent and shows a dark greyish colour. If deposited at lower bias voltages (–40 V - as in this case - up to –100 V), the coating reveals a thermodynamically favoured dual-phase structure of face-centered cubic (fcc) Cr(Al,V)N and wurtzite (w) type Al(Cr,V)N domains while no preferential incorporation of V in either phase was resolved [20].

To detect the onset of oxidation, O and N SIMS depth profiles for samples annealed at different temperatures are shown in Figure 1. First indications of oxidation can be detected at 600°C where a thin top layer is formed, represented by a decrease of the N and an increase of the O signal. If the temperature exceeds 600°C, more N is released and at 700°C approximately half of the coating is oxidised after 1 hour annealing time. Since the SIMS signal of each species depends strongly on its ion yield (ionisation), especially if the matrix changes, variations of up to one order of magnitude can be expected in a two layer system. The element specific calibration of the intensity scale is, however, impractical and the presented uncalibrated profiles serve for qualitative comparison only.

The important question of the diffusion of metallic components is addressed in Figure 2. Since Al and Cr do not present any indications of directed diffusion, only the V signal is shown. For $T \geq 600$°C, a V-rich layer on the coating surface can be noticed, whereas the remainder of the oxidised zone is V-depleted. Further, the obtained results suggest that diffusion of V occurs exclusively within the oxide layer, since a constant signal is measured for the remaining nitride.

An overview of the situation after annealing at 700°C is depicted in Figure 3 where all elemental depth profiles as obtained by SIMS are presented. While the bottom part of the coating remains unaffected, the oxidised part can be divided into two sublayers as indicated in

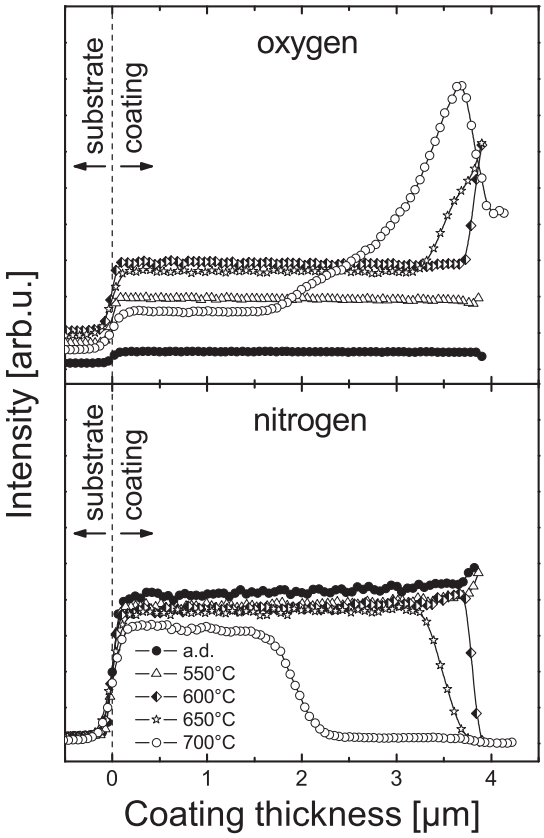

Figure 1: O and N depth profiles of oxidised $Al_{0.68}Cr_{0.10}V_{0.22}N$ at different annealing temperatures as obtained by SIMS. Lines are a guide for the eye.

Figure 3. V out-diffusion leads to a depletion in the lower layer resulting in an augmentation near the surface where, consequently, lower Al and Cr concentrations are detected.

3.2 XRD and Raman spectroscopy

The identification of crystalline compounds was addressed by XRD and Raman spectroscopy. For XRD measurements, a configuration with grazing incidence (2°) was used in order to restrict the information depth to the upper part of the coating. After annealing at $T \leq 600$°C, the coating remained unchanged as compared to the as-deposited state (see Figure 4a). First oxides can be detected at 650°C. The peak position and width suggest a nanocrystalline $(Al,Cr,V)_2O_3$ mixed oxide as Al and Cr oxides are able to form a complete solid solution at high temperatures, whereas V_2O_3 is only partially soluble in Al_2O_3 [21]. However, a further increase in temperature to 700°C results in the formation of several oxides after heating while the peaks originating from the nitride diminish. In addition to the already mentioned mixed oxide, $AlVO_4$ and V_2O_5 can be identified. Here, $AlVO_4$ is a solid state reaction product of the immiscible oxides Al_2O_3 and V_2O_5 [21, 22].

Raman spectroscopy is a more surface sensitive analysis method [23]. As shown in Figure 4b, there are already indications of oxide formation at 600°C owing to the very broad bands

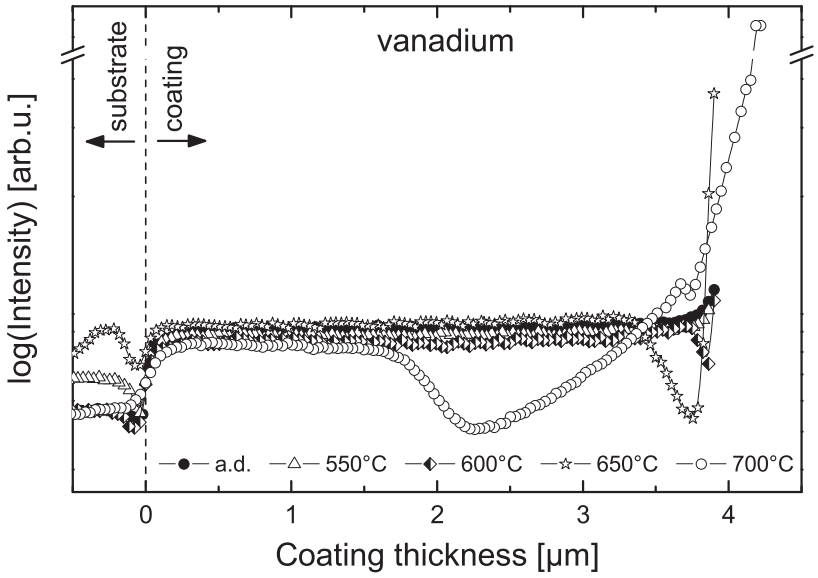

Figure 2: V depth profiles of oxidised $Al_{0.68}Cr_{0.10}V_{0.22}N$ at different annealing temperatures as obtained by SIMS. Lines are a guide for the eye.

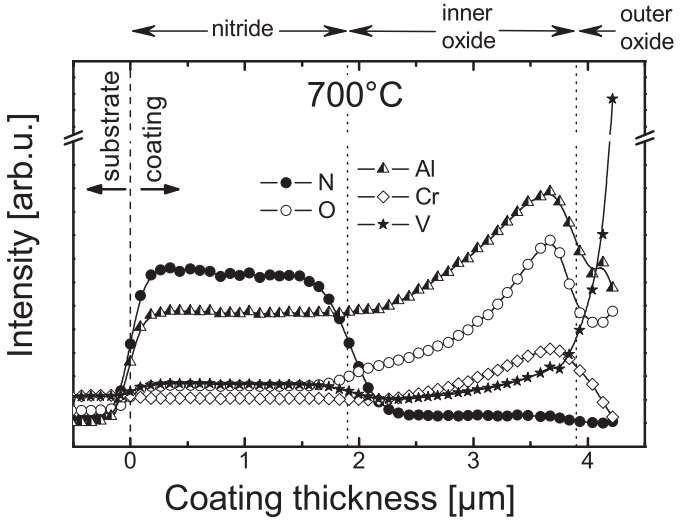

Figure 3: Elemental depth profiles of oxidised $Al_{0.68}Cr_{0.10}V_{0.22}N$ at 700°C as obtained by SIMS. Lines are a guide for the eye.

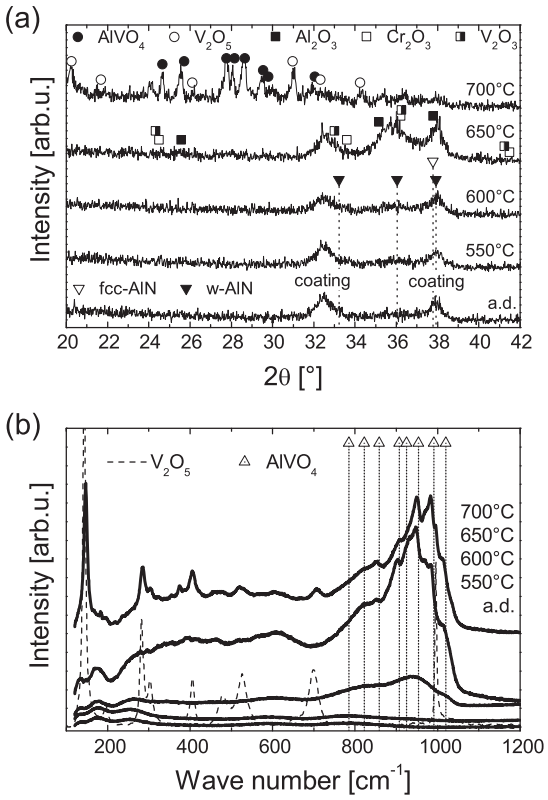

Figure 4: XRD (a) and Raman spectroscopy (b) measurements of oxidised $Al_{0.68}Cr_{0.10}V_{0.22}N$ at different annealing temperatures. Relevant standards are given.

in the wave number range 700–1000 cm^{-1}. These peaks are more intense for $T > 600°C$ and correlate well with characteristic vibrational modes of $AlVO_4$ [24, 25]. At the maximum temperature of 700°C, the formation of the desired V_2O_5 can be clearly identified by Raman spectroscopy corroborating the XRD results.

3.3 TEM

3.3.1 Morphology

A detailed analysis of the morphology and the crystalline phases of $Al_{0.68}Cr_{0.10}V_{0.22}N$ oxidised at 700°C is provided by TEM. Figure 5a shows a zero-loss filtered bright-field image of the cross-section where the formed oxide and the remaining nitride layer are clearly observable. As expected, the synthesised nitride coating reveals a columnar but dense microstructure. The in Figure 5c observable multilayer structure can be attributed to a compositional variation due to the substrate rotation during deposition [26]. Contrary to the original coating, the inner oxide layer presents a voided microstructure (see Figure 5c) most likely caused by the V out-diffusion. The V-rich toplayer, however, consists of dense crystallites with a diameter of up to 1 μm while a few of these crystallites are highlighted in Figure 5a and b.

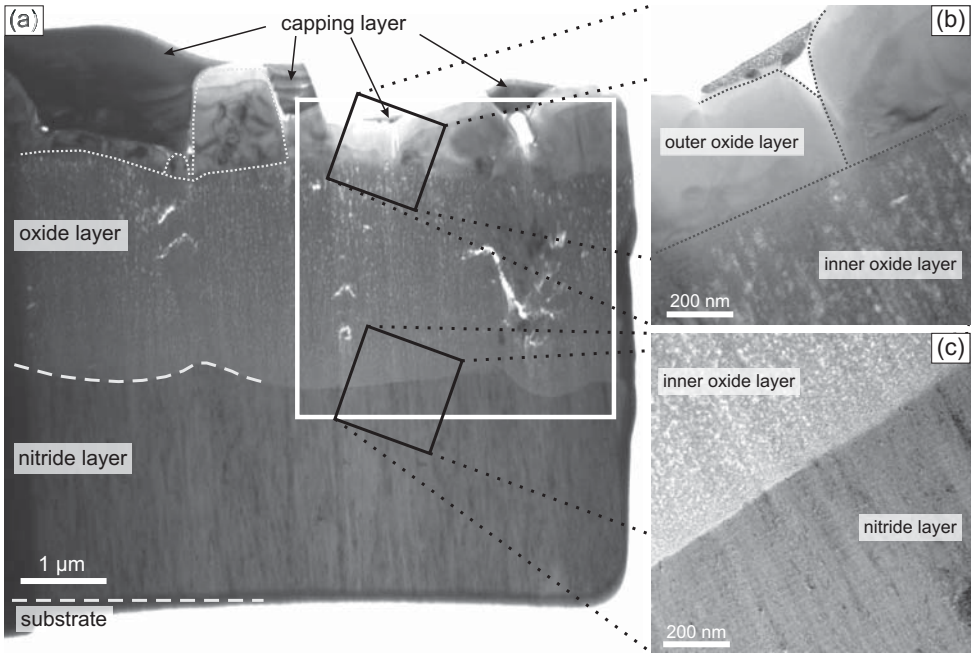

Figure 5: (a) Bright-field (zero loss) image of investigated TEM sample for overview. Areas with changes in the microstructure are magnified in (b) and (c). White dashed lines in (a) mark the border substrate-nitride as well as nitride-oxide. White dotted lines in (a) and grey dotted lines in (b) denote formed crystallites in the outer oxide layer.

3.3.2 Elemental distribution

Elemental mappings of N and O of the by the white rectangle in Figure 5a indicated zone are shown in Figure 6. As observable in the EELS spectra, there is a strong overlap of the V, O and Cr signal in the energy range 500–600 eV inhibiting the use of conventional energy-filtered TEM methods like three-window or jump ratio technique [27]. Therefore, STEM SI and MLLS were employed for obtaining the N and O mappings where a relatively sharp border between the remaining nitride layer and the oxidised part can be seen. Further, the contrast difference in the O mapping in the upper part corroborates the presence of two different oxide layers. The disturbance on the right hand side in both mappings is due to a growth defect within the imaged area and will be addressed later.

Mappings of the metallic components of the coating and Fe are shown in Figure 7. V diffusion to the surface is clearly detectable as seen by the increased intensity of the V signal in the near surface region in Figure 7a. The remaining Al,Cr-rich mixed oxide is observable in Figure 7b and c, whereas the toplayer still contains small traces of Al and Cr, attributed either to a preparation artifact or an incomplete separation. All these findings are again in agreement with the above presented SIMS results.

In addition, Fe diffusion from the substrate in this temperature range is generally negligible, the Fe mapping in Figure 7d only indicates diffusion to underdense areas in the vicinity of droplets. The formation of molten globules is inherent to the arc-evaporation technique and their incorporation into thin films results in the formation of growth defects [28, 29] as

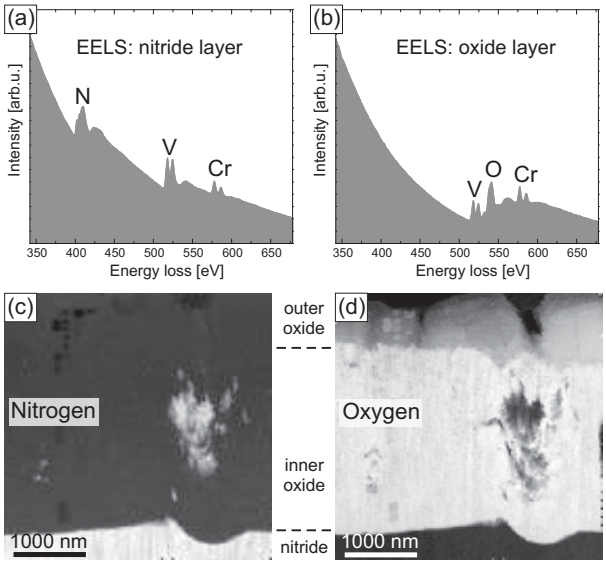

Figure 6: Examples of EELS spectra from (a) the unaffected nitride coating and (b) the oxidised part. The elemental mappings of (c) N and (d) O were obtained by EELS using STEM SI technique and MLLS fitting. The mapped area is indicated in Figure 5a by the white rectangle.

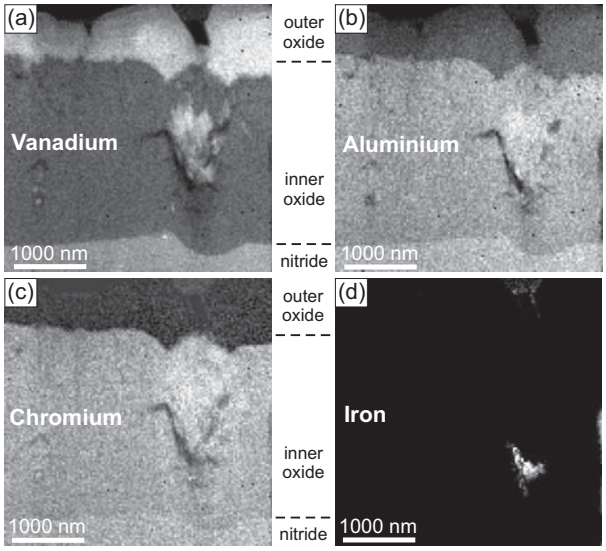

Figure 7: Elemental mappings of (a) V, (b) Al, (c) Cr and (d) Fe as obtained by EDX using STEM SI technique. The mapped area is indicated in Figure 5a by the white rectangle.

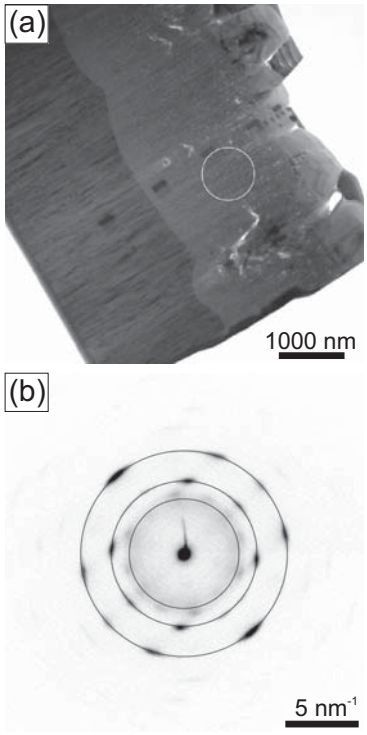

Figure 8: (a) TEM bright-field (zero loss) image of investigated sample for overview and (b) SAED pattern of the indicated area.

can be seen in the N and O mappings in Figure 6 by the O-depleted, but N-rich zone on the right-hand side. These growth defects influence the coating properties as they, e.g., increase the surface roughness and open pathways for O and Fe diffusion [30]. While the droplet itself normally oxidises easily, the coated zone on top of the droplet appears to remain unaffected and, thus, seems to be more resistant against oxidation.

3.3.3 Crystal structure

The camera constant λL of the TEM was calibrated using XRD data of $Al_{0.68}Cr_{0.10}V_{0.22}N$ in the as-deposited state and the selected area electron diffraction (SAED) pattern of the remaining nitride coating. Here, the via XRD obtained lattice parameters of $a = 0.4105$ nm for the fcc-AlCrVN phase and $a = 0.3173$ nm and $c = 0.5005$ nm for the w-AlCrVN phase were compared to the cubic lattice planes (111), (200), and (220) as well as the hexagonal planes (100) and (110) resulting in a camera constant of $\lambda L = 0.98$.

With the so obtained camera constant, the lattice spacings according to the three diffraction rings in the SAED pattern of the inner oxide (see Figure 8) can be calculated as shown in Table 1. These lattice spacing were assigned to the (104), (202) and (300) planes of the mixed $(Al,Cr,V)_2O_3$ after comparing to standard values of Al_2O_3, Cr_2O_3 and V_2O_3. All three single oxides exhibit a rhombohedral structure with similar lattice constants and the lattice parameters of the mixed oxide should, thus, be within their range.

For the outer V-rich oxide layer, the investigated zone is indicated in Figure 9a. The HR-TEM bright-field image shown in Figure 9c reveals a monocrystalline structure which can

Table 1: Radii R and calculated lattice spacings d of the fringes in the SAED pattern in Figure 8b. Lattice spacings of different oxides are given as reference.

R [nm^{-1}]	d [nm]	Al_2O_3[1]	Cr_2O_3[2]	V_2O_3[3]	lattice plane
3.72	0.26	0.2551	0.2665	0.2712	(104)
4.94	0.20	0.1965	0.2048	0.2029	(202)
7.00	0.14	0.1374	0.1432	0.1430	(300)

be understood by melting and subsequent crystallisation of V_2O_5 during the heat treatment cycle [10]. More details concerning the crystal structure can be derived from the SAED pattern in Figure 9b. Although an unambiguous determination is impractical from a single pattern, it appears to be reasonable to assign the lattice spacing of 0.43 nm, calculated from the marked spot distance in the SAED pattern, to the (001) lattice planes of orthorhombic V_2O_5. First, the obtained lattice spacing is in good agreement with reference values of 0.4368 nm [34] and 0.4383 nm [35] and, second, the peak at $2\theta = 20.244°$ [35] in the XRD pattern (700°C) results from diffraction on (001) planes.

4 Discussion

The measured SIMS depth profiles suggest that coating oxidation is needed for the diffusion of V to the surface where it forms a lubricious oxide scale [10]. Diffusion from the remaining nitride coating can be excluded since the V concentration is constant within this region. The segregation could be understood by the immiscibility of the V oxides (V_2O_5 and V_2O_3) with Al_2O_3 and Cr_2O_3 [21] and the occurring phase separation leads to the formation of the obtained dual-layer structure of the oxidised part. Here, the by XRD and Raman spectroscopy evidenced $AlVO_4$, the reaction product of Al_2O_3 and V_2O_5, is most likely located at the border between both layers while no indications for $CrVO_4$ were found within this work.

Within the V-rich toplayer the identification of the (001) planes in orthorhombic V_2O_5 is suggested by XRD and SAED investigations. Since these planes are exclusively bonded by van der Waals forces between the oxygen atoms [36], this specific bonding structure allows for easy shearing of the (001) planes giving rise to the expected possible solid lubrication offered by V_2O_5. In Figure 9b, the (001) lattice planes are indicated by solid lines and compared to the orientation of the substrate-coating interface which is depicted by the dashed line. Although both orientations are not parallel to each other in the investigated area, the lattice planes can align parallel to the direction of relative motion in a tribological contact [37]. In tribological tests at 700°C, the formation of V_2O_5 in the wear track was evidenced by Raman spectroscopy [10] and is in agreement with the observation within this work. However, the reduction of friction with a recorded COF of 0.2 [10] was mainly attributed to liquid lubrication as V_2O_5 presents a low melting point of 670°C [6] and that apparently has a stronger effect than solid lubrication. The occurring melting and subsequent solidification during cooling was indicated by dendritic structures on the surface and is corroborated by the rather large crystallite size in the outer oxide as shown in Figure 5a and b.

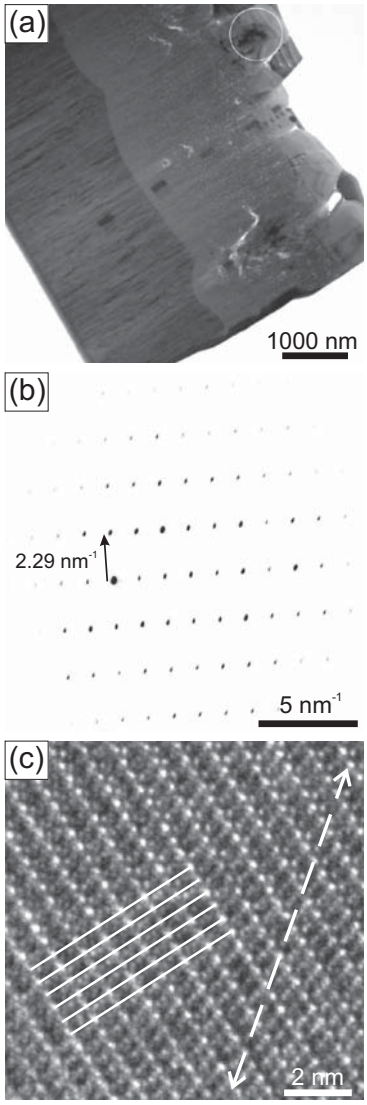

Figure 9: (a) TEM bright-field (zero loss) image of investigated sample for overview. (b) SAED pattern of indicated area and (c) higher magnified TEM bright-field image within the same zone. In (c), dashed arrows represent orientation of substrate-coating interface and solid lines mark (001) lattice planes of V_2O_5.

A comparison of AlCrVN with TiAlN/VN multilayers coatings reveals an onset temperature for oxidation in the same range of ∼600°C, whereas different oxides were found at this temperature. In case of TiAlN/VN multilayers the lubricious oxide V_2O_5 was detected as soon as oxidation occurred [12] while at higher temperatures only TiO_2 and $AlVO_4$ are present. During the oxidation process of AlCrVN, the formation of the oxides $AlVO_4$ and $(Al,Cr,V)_2O_3$ was obtained first. V_2O_5 was only evidenced at an annealing temperature of 700°C marking a 100 K increase as compared to TiAlN/VN multilayers. That means, the higher oxidation resistance of AlCrN [15] seems to beneficially influence the oxidation behaviour of AlCrVN. After comparable heat treatments in a temperature range of 650 − 700°C, the TiAlN-based coatings were completely oxidised [8, 12–14] whereas only

$\sim$50% of $Al_{0.68}Cr_{0.10}V_{0.22}N$ were oxidised at the maximum annealing temperature of 700°C. Thus, lubricating effects at increased temperatures are offered by AlCrVN which still maintains its mechanical integrity.

5 Conclusion

From the investigation of oxidised AlCrVN hard coatings several interesting conclusions can be drawn. As a result of the immiscibility between the V oxides and Al_2O_3 as well as Cr_2O_3, two different oxide layers are formed during annealing of $Al_{0.68}Cr_{0.10}V_{0.22}N$ in ambient atmosphere. While the occurring V diffusion leads to a V-depleted inner oxide, the outer oxide is V enriched and mainly contains V_2O_5 as evidenced by XRD and Raman spectroscopy, whereas its dense morphology is due to melting and subsequent solidification of V_2O_5. In general, V_2O_5 with its easy shearable lattice planes might provide for solid lubrication in tribological applications at elevated temperatures as well as liquid lubrication owing to its low melting point. Further, oxidation is needed to trigger the diffusion process as no out-diffusion of V could be observed from the remaining nitride coating. Thus, the mechanical integrity of the remaining nitride layer is preserved resulting in a competitive wear resistance of the AlCrVN hard coatings.

Acknowledgement

Financial support by the Christian Doppler Research Association is highly acknowledged as well as the assistance by Plansee GmbH (Lechbruck, Germany) and Oerlikon Balzers Coatings AG (Balzers, Liechtenstein) within the framework of the CD laboratory 'Advanced Hard Coatings'.

References

[1] A. Magnéli, Acta Crystallogr. **6**, 495 (1953).
[2] M. Woydt, A. Skopp, I. Dörfel, and K. Witke, Wear **218**, 84 (1998).
[3] A. Erdemir, Tribol. Lett. **8**, 97 (2000).
[4] G. Gassner, P. Mayrhofer, K. Kutschej, C. Mitterer, and M. Kathrein, Tribol. Lett. **17**, 751 (2004).
[5] N. Fateh, G. Fontalvo, G. Gassner, and C. Mitterer, Wear **262**, 1152 (2007).
[6] D. R. Lide, ed., *CRC Handbook of Chemistry and Physics* (CRC Press, 2004), 85th ed.
[7] W.-D. Münz, L. Donohue, and P. Hovsepian, Surf. Coat. Technol. **125**, 269 (2000).
[8] P. Mayrhofer, P. Hovsepian, C. Mitterer, and W.-D. Münz, Surf. Coat. Technol. **177-178**, 341 (2004).
[9] K. Kutschej, P. Mayrhofer, M. Kathrein, P. Polcik, and C. Mitterer, Surf. Coat. Technol. **188-189**, 358 (2004).
[10] R. Franz, J. Neidhardt, B. Sartory, R. Kaindl, R. Tessadri, P. Polcik, V. Derflinger, and C. Mitterer, Tribol. Lett. **23**, 101 (2006).
[11] Q. Luo, Z. Zhou, W. Rainforth, and P. Hovsepian, Tribol. Lett. **24**, 171 (2006).

[12] Z. Zhou, W. Rainforth, D. Lewis, S. Creasy, J. Forsyth, F. Clegg, A. Ehiasarian, P. Hovespian, and W.-D. Münz, Surf. Coat. Technol. **177-178**, 198 (2004).
[13] D. Lewis, S. Creasey, Z. Zhou, J. Forsyth, A. Ehiasarian, P. Hovsepian, Q. Luo, W. Rainforth, and W.-D. Münz, Surf. Coat. Technol. **177-178**, 252 (2004).
[14] K. Kutschej, P. Mayrhofer, M. Kathrein, P. Polcik, and C. Mitterer, Surf. Coat. Technol. **200**, 1731 (2005).
[15] M. Kawate, A. Hashimoto, and T. Suzuki, Surf. Coat. Technol. **165**, 163 (2003).
[16] W. Kalss, A. Reiter, V. Derflinger, C. Gey, and J. Endrino, Int. J. Refract. Met. Hard Mater. **24**, 399 (2006).
[17] J. Mayer, L. Giannuzzi, T. Kamino, and J. Michael, MRS Bulletin **32**, 400 (2007).
[18] V. Keast and M. Bosman, Microsc. Res. Tech. **70**, 211 (2007).
[19] R. Leapman and C. Swyt, Ultramicroscopy **26**, 393 (1988).
[20] R. Franz, J. Neidhardt, B. Sartory, R. Tessadri, and C. Mitterer, Thin Solid Films (submitted).
[21] R. S. Roth, ed., *Phase Equilibria Diagrams - Phase Diagrams for Ceramists*, vol. XI - Oxides (The American Ceramic Society, Westerville, Ohio, USA, 1995).
[22] O. Yamaguchi, T. Uegaki, Y. Miyata, and K. Shimizu, J. Am. Ceram. Soc. **70**, C (1987).
[23] R. McCreery, *Raman Spectroscopy for Chemical Analysis*, vol. 157 of *Chemical Analysis* (Wiley-Interscience, New York, 2000).
[24] B. Leyer, H. Schmelz, H. Göbel, H. Meixner, T. Scherg, and H. Knözinger, Thin Solid Films **310**, 228 (1997).
[25] V. Brázdová, M. Ganduglia-Pirovano, and J. Sauer, J. Phys. Chem. B **109**, 394 (2005).
[26] J. Neidhardt, M. O'Sullivan, A. Reiter, W. Rechberger, W. Grogger, and C. Mitterer, Surf. Coat. Technol. **201**, 2553 (2006).
[27] J. Verbeeck, D. Van Dyck, and G. Van Tendeloo, Spectrochim. Acta, Part B **59**, 1529 (2004).
[28] R. L. Boxman, D. M. Sanders, and P. J. Martin, eds., *Handbook of Vacuum Arc Science and Technology: Fundamentals and Applications* (Noyes Publications, New Jersey, 1995).
[29] I. Petrov, P. Losbichler, D. Bergstrom, J. Greene, W.-D. Münz, T. Hurkmans, and T. Trinh, Thin Solid Films **302**, 179 (1997).
[30] A. Hörling, L. Hultman, M. Odén, J. Sjölén, and L. Karlsson, J. Vac. Sci. Technol. A **20**, 1815 (2002).
[31] Powder Diffraction File 01-081-1667, International Center for Diraction Data, PDF-2/Release 2005.
[32] Powder Diffraction File 00-038-1479, International Center for Diraction Data, PDF-2/Release 2005.
[33] Powder Diffraction File 03-065-9474, International Center for Diraction Data, PDF-2/Release 2005.
[34] R. Enjalbert and J. Galy, Acta Crystallogr. C: Cryst. Struct. Commun. **42**, 1467 (1986).
[35] Powder Diffraction File 01-089-0611, International Center for Diraction Data, PDF-2/Release 2005.
[36] J. Galy, A. Ratuszna, J. Iglesias, and A. Castro, Solid State Sci. **8**, 1438 (2006).
[37] A. Erdemir, in *Modern Tribology Handbook*, edited by B. Bhushan (CRC Press, Boca Raton, 2001), vol. 2, chap. 22, pp. 787–825.

Publication V

Influence of phase transition on the tribological performance of arc-evaporated AlCrVN hard coatings

R. Franz, J. Neidhardt, R. Kaindl, B. Sartory, R. Tessadri, M. Lechthaler, P. Polcik, C. Mitterer

final preparation

Influence of phase transition on the tribological performance of arc-evaporated AlCrVN hard coatings

R. Franz[a], J. Neidhardt[a], R. Kaindl[b], B. Sartory[b], R. Tessadri[b], M. Lechthaler[c], P. Polcik[d], C. Mitterer[a]

[a] *Christian Doppler Laboratory for Advanced Hard Coatings at the Department of Physical Metallurgy and Materials Testing, University of Leoben, Franz-Josef-Strasse 18, A-8700 Leoben, Austria*
[b] *Institute of Mineralogy and Petrography, University of Innsbruck, Innrain 52, A-6020 Innsbruck, Austria*
[c] *Oerlikon Balzers Coating AG, Iramali 18, FL-9496 Balzers, Principality of Liechtenstein*
[d] *Plansee GmbH, Siebenbürgerstrasse 23, D-86983 Lechbruck am See, Germany*

V-alloyed AlCrN hard coatings were synthesised by reactive arc-evaporation in an industrial-sized deposition system at bias voltages ranging from –40 to –150 V. X-ray diffraction analysis has shown that higher energetic growth conditions stabilise the desired metastable face-centered cubic (fcc) crystal structure of $Al_{0.70}Cr_{0.05}V_{0.25}N$ even at very high Al/Cr ratios resulting in hardness values comparable to $Al_{0.70}Cr_{0.30}N$ at room temperature. Ball-on-disc tests were used to assess the friction at 700°C where $Al_{0.70}Cr_{0.05}V_{0.25}N$ coatings revealed a generally lower coefficient of friction due to the formation of a tribolayer containing the lubricious oxide V_2O_5 as evidenced by Raman spectroscopy. Here, the single-phase fcc-$Al_{0.70}Cr_{0.05}V_{0.25}N$ coating appears to be more oxidation resistant leading to a reduced formation of V_2O_5 and, hence, an increase in friction. Wear data was obtained by conducting side milling tests under dry conditions. $Al_{0.70}Cr_{0.05}V_{0.25}N$ coatings showed a competitive cutting performance regardless the growth conditions as the reduced lubricity is compensated by higher hardness.

KEY WORDS: hard coatings, AlCrVN, lubricious oxides, arc-evaporation

1 Introduction

The metastable face-centered cubic (fcc) structure of AlCrN hard coatings can be stabilised up to an Al/Cr ratio of ∼3 [1, 2]. These coatings are characterised by high hardness [3–5], good thermal stability [6, 7] and oxidation resistance [8–12] and are nowadays used in metal cutting and many other industrial applications [13–16]. Tribological investigations though revealed a high coefficient of friction (COF), especially at elevated temperatures ≥500°C [17]. These temperatures are easily reached when the environmentally and economically more favourable cutting with reduced coolants or even dry-cutting is used. Therefore, research has focused on the development of self-adaptive coatings, that offer lubricity at elevated temperatures [18, 19] while retaining their mechanical integrity [20–23].

The incorporation of V into existing state-of-the-art hard coatings, namely TiAlN/VN multilayers and TiAlVN and AlCrVN solid solutions, enabled the combination between the formation of lubricious oxides and high wear resistance in high-temperature tribological tests. At a testing temperature of 700°C, the formation of V_2O_5 results in a drop of the COF from 0.6–0.8 to 0.2–0.3 which was mainly attributed to a liquid lubrication mechanism [21–23]. V_2O_5 can act as liquid lubricant due to its low melting point of 670°C [24] as well as solid lubricant owing to weakly-bonded and, hence, easy shearable lattice planes in the crystal structure [25]. However, controlled oxidation is a prerequisite for the V_2O_5 formation. Investigations of the oxidation behaviour of the above mentioned V-containing TiAlN coatings have revealed that V_2O_5 forms at temperatures ≥600°C, whereas rapid oxidation and transition to other oxides at temperatures up to 700°C result in a strongly

reduced V_2O_5 content on the surface [21, 26–28]. On the other hand, AlCrVN appears to be more oxidation resistant and even at 700°C a pronounced V_2O_5 scale is formed on the surface after annealing in ambient air [29]. This increase is most likely attributed to the stronger self-passivating effect of AlCrN as compared to TiAlN [9].

However, the composition of the AlCrVN coatings used within this work is in the range of the maximum metastable solubility of AlN in fcc-(Cr,V)N causing a partial transition to a hexagonal wurtzite (w) type phase if synthesised at a low bias voltage of –40 V. In Ref. [30] it has been shown that higher energetic growth conditions achieved by applying higher bias voltages during deposition stabilise the fcc-AlCrVN phase and, hence, reduce the w-AlCrVN phase fraction and at a bias voltage of –150 V a single-phase fcc-AlCrVN can be retained. This work, therefore, relates the occurring phase transition at increasing bias voltage to the tribological behaviour of the AlCrVN hard coatings with a focus on the formation of a lubricating tribolayer containing the lubricious oxide V_2O_5 and compares it to the V-free AlCrN.

2 Experimental

V-alloyed AlCrN coatings were synthesised in a commercial arc-evaporation system (Oerlikon Balzers RCS) with a base pressure below 4×10^{-3} Pa. The substrates, high-speed steel (DIN 1.3343, AISI M2) coupons (⌀ 30 mm × 10 mm), cemented carbide cutting inserts (grade 10), and silicon stripes (Si (100), 20 mm × 7 mm × 0.525 mm), were heated to 500°C and etched in a pure Ar plasma with ions extracted from an additional arc discharge. During deposition, the substrate bias voltage was set to a constant value of –40 V, –70 V, –100 V and –150 V, whereas the N_2 gas pressure was regulated at 3.5 Pa. 4 arc-sources were equipped with powder-metallurgically produced $Al_{0.70}Cr_{0.05}V_{0.25}$ or $Al_{0.70}Cr_{0.30}$ targets and current controlled to 140 A. The targets exhibit a homogeneous erosion behaviour at industrially competitive deposition rates of ∼50 nm/min on two-fold rotating substrates. The chemical composition of the resulting coatings was determined by electron probe microanalysis (EPMA) by means of wavelength-dispersive X-ray spectroscopy using a JEOL JXA 8100 Superprobe under an acceleration voltage of 10 kV and an analysed spot size of ∼40 μm × 40 μm. X-ray diffraction (XRD) data for analysing the crystal structure were obtained by a D8 diffractometer from Bruker AXS with parallel beam geometry equipped with a Cu-ceramic tube and an energy-dispersive detector (SolX from Bruker AXS) via $\theta - 2\theta$ scans. Hardness measurements according to Oliver and Pharr [31] were conducted using a UMIS II nanoindenter equipped with a Berkovich indenter applying a maximum load ranging from 30–40 mN. The cantilever beam bending technique used for determining the biaxial stress state of the coatings on the silicon stripes is described in Ref. [32].

The tribological tests were performed using a ball-on-disc tribometer from CSM Instruments at a testing temperature of 700°C. The load was kept constant at 5 N and the sliding speed was set to 10 cm/s. No lubricant was applied. Sintered alumina balls with a purity of 99.8% and a diameter of 6 mm were chosen as counterpart due to their chemical inertness at high temperatures. The sliding distance was set to 300 m and the radius of the wear track to 7 mm. Raman spectra after tribological testing were obtained with a HORIBA Jobin Yvon LabRam-HR800 Raman micro-spectrometer from areas out and inside of the wear track. The device is equipped with a 5.9 mW He-Ne laser (633 nm line) and a 30 mW Ar^+-laser

Table 1: Chemical composition, growth rate and thickness of the synthesised AlCrVN and AlCrN coatings in dependence on the bias voltage. Deposition time was 60 min, except for –40 V where 110 min were used.

Bias [-V]	Coating composition $Al_{x_{Al}}Cr_{x_{Cr}}V_{x_V}N$	Growth rate [nm/min]	Thickness [μm]
40	$Al_{0.67}Cr_{0.07}V_{0.26}N$	55	6.0
70	$Al_{0.68}Cr_{0.07}V_{0.25}N$	56	3.4
100	$Al_{0.67}Cr_{0.07}V_{0.26}N$	52	3.1
150	$Al_{0.68}Cr_{0.07}V_{0.25}N$	49	2.9
[-V]	$Al_{x_{Al}}Cr_{x_{Cr}}N$	[nm/min]	[μm]
40	$Al_{0.71}Cr_{0.29}N$	48	5.3
70	$Al_{0.69}Cr_{0.31}N$	53	3.2
100	$Al_{0.69}Cr_{0.31}N$	52	3.1
150	$Al_{0.69}Cr_{0.31}N$	50	3.0

(514 and 488 nm line). The laser spot on the surface had a diameter of approximately 1 μm and the spectral resolution ranged between 0.8 and 2.1 cm^{-1}. Scanning electron microscopy (SEM) images of the wear track were taken by the device used for EPMA while backscattered electrons were utilised for a more pronounced elemental contrast. Side milling tests of stainless steel (DIN 1.4571) under dry conditions were conducted on a Mikron VCE equipped with a 3-teeth cutter of 8 mm in diameter and 0.5 mm corner radius. The cutting speed was set to $v_c = 145$ m/min at a feed rate of $f_z = 0.079$ mm/tooth and an axial and radial feed of $a_e = 0.3$ mm and $a_p = 5$ mm, respectively.

3 Results

3.1 Structure and mechanical properties

A short overview of the crystal structure and related mechanical properties will be presented. In general, all coatings are well adherent and show a dark greyish colour. As shown in Table 1, the variation of the bias voltage does not affect the coating composition significantly. All deposited coatings are stoichiometric and the obtained N ratio of $\sim$ 50 at.% suggests the absence of intermetallic phases. Further, the target compositions of $Al_{0.70}Cr_{0.05}V_{0.25}$ and $Al_{0.70}Cr_{0.30}$ are roughly mirrored in the metal ratio indicating no element-specific effect of resputtering due to the increase of ion energy. Only, a slight Al deficiency of 2–3 at.%, presumably due to gas scattering, throughout the whole range of bias voltages can be noticed which is in agreement with previous results [23, 30].

Differences are, however, expected regarding the coating structure as investigated by XRD. The dual-phase structure of AlCrVN deposited at a bias voltage of –40 V is clearly observable in Figure 1. An increase of the ion energy during synthesis stabilises the cubic phase and at

the maximum bias voltage of –150 V, a single-phase fcc-AlCrVN coating is obtained. This coating exhibits a structure equivalent to fcc-AlCrN with its superior mechanical properties and oxidation resistance as compared to w-AlCrN [6].

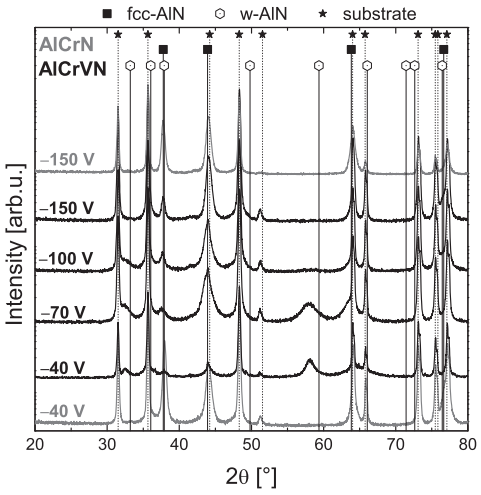

Figure 1: XRD patterns of AlCrVN and AlCrN coatings deposited at different bias voltages.

Details concerning the hardness and biaxial coating stress are shown in Figure 2 and related to the fcc phase fraction. The increase of the defect density generated by the bombardment of energetic ions at higher bias voltages leads to a distinct increase of the compressive stress from 1–1.5 GPa to 3.5–4 GPa similar for both coating types. Strain hardening effects associated with the increase of the stress state at higher bias voltages result in a slight increase in hardness to ∼34 GPa for AlCrN. In case of AlCrVN, the occurring phase transition additionally influences the evolution of the hardness while the significant hexagonal phase fraction at low bias voltages is related to a low hardness of ∼25 GPa. The stabilisation of the metastable fcc phase at higher bias voltages results in a dramatic increase in hardness leading to comparable values of ∼34 GPa at voltages of –100 V or higher.

As shown in Table 1, indications of the structural changes are also manifested in the evolution of the growth rate since the exact sample position during deposition was maintained when raising the bias voltage from –70 V to –150 V. The general decrease of the growth rate with increasing bias voltage can be understood by a densification of the coating due to the enhanced ion bombardment. In case of AlCrVN, the occurring phase transition should additionally influence the growth rate as the fcc crystal structure reveals a by ∼25% higher density as compared to the wurtzite type structure.

3.2 Friction behaviour and cutting performance

The main focus of the present study lies on the tribological behaviour of the AlCrVN coatings investigating the influence of the occurring changes in the crystal structure on the formation of lubricious oxides and, hence, the COF at elevated temperatures. Therefore, the COF versus sliding distance was recorded at a testing temperature of 700°C as shown in Figure 3.

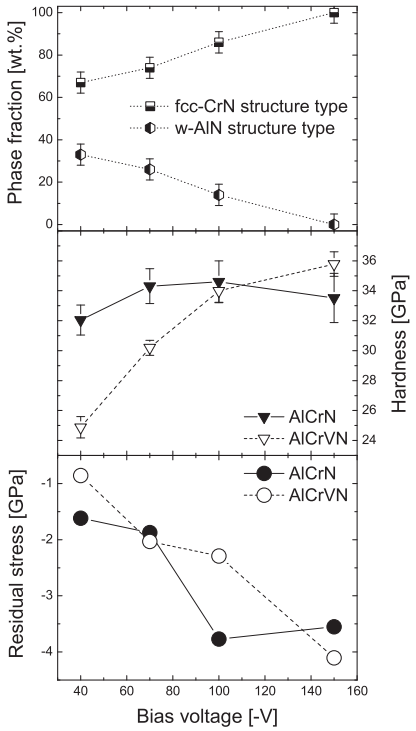

Figure 2: Phase fractions as obtained by Rietveld refinement of the XRD patterns, hardness and biaxial coating stress of as-deposited AlCrVN and AlCrN coatings in dependence on bias voltage. Lines are a guide for the eye.

In general, there is a distinct reduction of friction for the V containing coatings as compared to the V-free AlCrN. While the COF for AlCrN is in the range of 0.6–0.7 regardless the bias voltage, a decrease to 0.2–0.4 can be obtained if V is present. In contrast to AlCrN, there is a slight dependence of the friction on the applied bias voltage for AlCrVN. In the low-bias regime (–40 and –70 V) the COF remains constant at a value of 0.2 over the whole sliding distance, whereas, in case of –100 V, a slight increase of the COF to 0.3 can be observed. A further increase of the bias voltage to –150 V results in the highest recorded friction values for the V containing coatings. The COF reaches a steady-state value of 0.4 after a running-in period of up to 100 m.

More insights about lubricating mechanisms active during ball-on-disc tests on AlCrVN coatings can be gained by means of Raman spectroscopy. Here, the chemical analysis outside of the wear track indicates the situation prior to tribological testing at 700°C. As shown in Figure 4a, all four AlCrVN coatings exhibit similar Raman spectra regardless the applied bias voltage. The main contribution in the spectra is attributed to V_2O_5, whereas small amounts of $AlVO_4$ are also present as suggested by the broad bands at wave numbers around 900 cm^{-1}. A different situation is encountered when analysing the worn surface inside the wear track as shown in Figure 4b. Up to a bias voltage of –100 V, there is still a significant amount of V_2O_5 present, but the contribution of $AlVO_4$ has increased considerably. Further, at the maximum applied bias voltage of –150 V, only $AlVO_4$ can be detected on the worn surface while the absence of the lubricious V_2O_5 correlates with the increase of the COF.

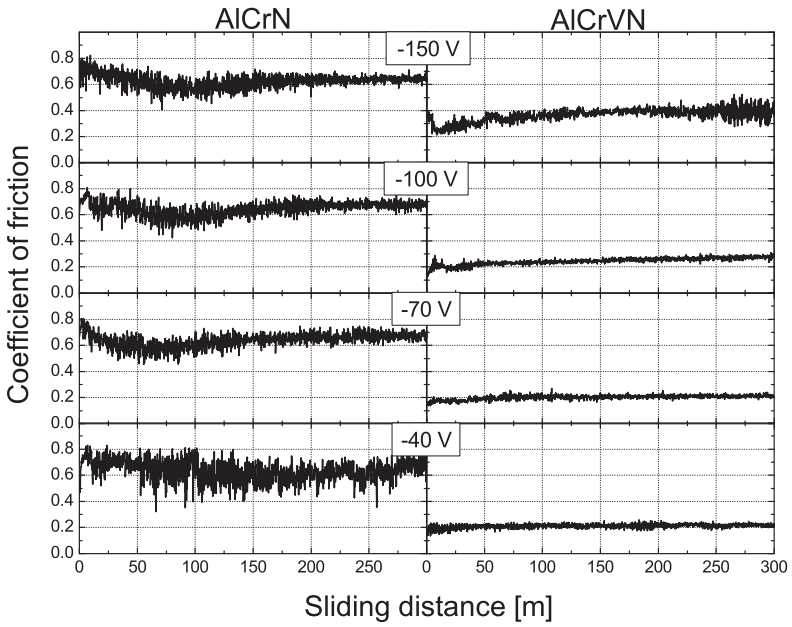

Figure 3: Coefficient of friction versus sliding distance obtained by ball-on-disc tests of AlCrN and AlCrVN coatings at 700°C.

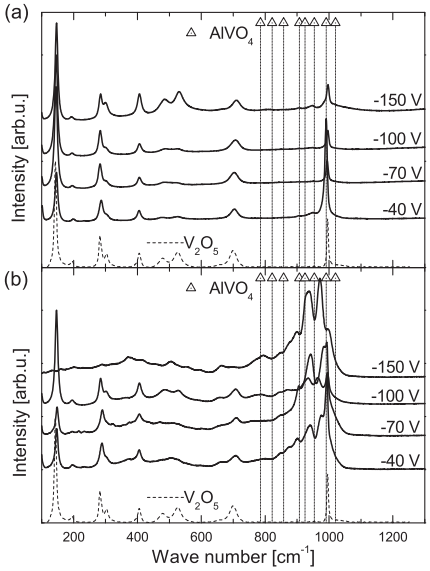

Figure 4: Raman spectra of (a) the surface outside of the wear track and (b) the worn surface in the wear track after ball-on-disc tests at 700°C. Relevant standards are given ($AlVO_4$ peak positions from Ref. [33]).

Details of the impact of high-temperature tribological testing on the surface morphology are provided by SEM images of the wear track. As shown in Figure 5, differences in the morphology of the worn surface as well as the coating surface outside of the wear track are obtained. In the low-bias regime (–40 and –70 V), dendritic structures cover the entire surface area, unlike the pronounced wear track that is visible at higher bias voltages. In the latter case, the increased contrast results from a difference in the chemical composition, most likely due to Fe enrichment in the wear track caused by diffusion from the substrate through the thin remaining coating or partial removal of the same. Further, both coatings reveal a surface morphology after tribological testing similar to AlCrN (bias –40 V) as shown in Figure 5a.

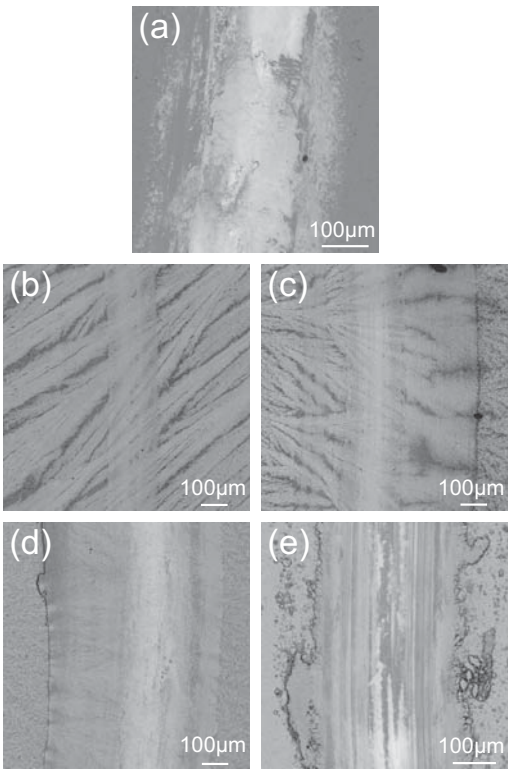

Figure 5: Backscattered electron SEM images of the surface morphology after ball-on-disc tests at 700°C in dependence on the bias voltage. AlCrN deposited at –40 V (a) and AlCrVN deposited at –40 V (b), –70 V (c), –100 V (d) and –150 V (e).

As to the cutting performance, wear data from side milling tests of stainless steel under dry conditions are shown in Figure 6. The performance of both tested AlCrVN coatings (–40 and –100 V bias) is generally comparable to the optimised commercial AlCrN. Indications for a slightly longer lifetime of tools coated with AlCrVN at –100 V as compared to –40 V can be noticed. However, the alike performance of these two coatings appears to be a result of the interplay between friction and mechanical properties. With increasing bias voltages the loss of lubricity is compensated by the higher hardness and vice versa.

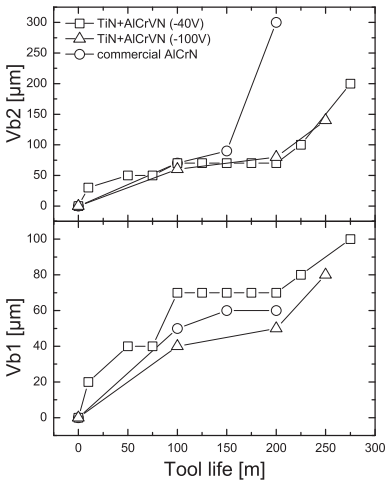

Figure 6: Average flank wear Vb1 and maximum flank wear Vb2 during side milling tests of stainless steel under dry conditions.

4 Discussion

The lubricious effects obtained during ball-on-disc tests of AlCrVN coatings at elevated temperatures can be clearly related to the presence of the lubricious oxide V_2O_5. Due to its low melting point of 670°C [24], it can act as a liquid lubricant at a testing temperature of 700°C. However, oxidation and diffusion processes determine the amount of V_2O_5 that is formed [29] and, hence, decide if a continuous lubricious layer can be established. Annealing experiments of AlCrN revealed a reduced oxidation resistance for coatings exhibiting a w-AlCrN structure as compared to fcc-AlCrN [6, 12]. The by ∼25% higher density of the fcc crystal structure seems to hinder oxygen diffusion into the coating more effectively than the hexagonal structure. Assuming an analogous influence of the phase structure of AlCrVN on the oxidation behaviour, the coatings deposited at higher bias voltages might be more resistant against oxidation. Here, the enhanced ion bombardment with increasing bias appears to be beneficial for the stabilisation of the fcc-AlCrVN phase as it enables adatom diffusion and collisional mixing at the growth front [30]. However, oxidation is a prerequisite for reducing the friction and investigations of oxidised AlCrVN revealed the formation of a V-rich toplayer at 700°C containing mainly V_2O_5 [29]. Figures 5d and e indicate that less V_2O_5 is formed on the surfaces of the AlCrVN coatings deposited at higher bias voltages (–100 V and –150 V). These smaller amounts of V_2O_5 appear not to be sufficient to maintain a continuous lubricious layer during the ball-on-disc test and higher COF values are recorded. This is corroborated by the finding, that the exposed $AlVO_4$ is most likely located between the V_2O_5 toplayer and an underlying layer consisting of a mixed or nanocrystalline $(Al,Cr,V,)_2O_3$ [29]. As the instable lubricious layer is removed during sliding, only the solid $AlVO_4$ remains in the wear track. The reduction of V_2O_5 to VO_2 that was related to an increase in friction of TiAlN/VN multilayer coatings in Ref. [21] does not occur in case of AlCrVN in the tested temperature range since no VO_2 was detected by Raman spectroscopy.

Promising results were obtained in the conducted cutting tests, despite the fact that the tested AlCrVN coatings exhibit a dual-phase crystal structure as compared to the optimised commercial AlCrN with single-phase fcc structure. Most surprising is the observed competitive wear resistance of the AlCrVN coating synthesised at a bias voltage of –40 V with its considerably reduced hardness. The unfavourable mechanical properties seem to be compensated by the lubrication effect resulting from the formation of V_2O_5. The opposite effect occurs for the coating deposited at –100 V where the reduced amount of V_2O_5 is outbalanced by the higher hardness. So far, the influence of the lubricious oxide could not be verified in the performed cutting tests directly, but is derived from the high-temperature ball-on-disc tests. The operation temperature in milling applications is exclusively controlled by the process parameters since no external heating is applied. However, lubricious oxides can form at the asperities due to the very high flash temperatures encountered at the cutting edge.

5 Conclusion

Studying the tribological behaviour of arc-evaporated AlCrVN at elevated temperatures, the occurrence of oxidation is a prerequisite for the formation of a lubricious tribolayer. Coatings deposited at low bias voltages at –40 V and –70 V with a distinct fraction of wurtzite type AlCrVN, presumably present a lower oxidation resistance and a continuous lubricating layer containing V_2O_5 can form at a testing temperature of 700°C leading to a COF of 0.2. Reducing the formation of V_2O_5 due to the higher oxidation resistance of nearly or completely single-phase face-centered cubic AlCrVN coatings synthesised in the high-bias regime (–100 V and –150 V), results in instable lubricious layers and the COF increases up to 0.4. However, all AlCrVN coatings reveal a lower friction as compared to the V-free AlCrN with a COF of 0.6–0.7 at the tested temperature. As to the wear resistance, the interplay between friction and mechanical properties leads to comparable cutting performances of both, low- and high-bias AlCrVN coatings. Here, the obtained tool lifetime is in the range of an optimised commercial AlCrN showing the potential of the AlCrVN hard coatings.

Acknowledgement

Financial support by the Christian Doppler Research Association is highly acknowledged.

References

[1] A. Sugishima, H. Kajioka, and Y. Makino, Surf. Coat. Technol. **97**, 590 (1997).
[2] Y. Makino and K. Nogi, Surf. Coat. Technol. **98**, 1008 (1998).
[3] O. Knotek, F. Loeffler, and H.-J. Scholl, Surf. Coat. Technol. **45**, 53 (1991).
[4] J. Vetter, E. Lugscheider, and S. Guerreiro, Surf. Coat. Technol. **98**, 1233 (1998).
[5] M. Kawate, A. Kimura, and T. Suzuki, J. Vac. Sci. Technol. A **20**, 569 (2002).
[6] A. Reiter, V. Derflinger, B. Hanselmann, T. Bachmann, and B. Sartory, Surf. Coat. Technol. **200**, 2114 (2005).
[7] H. Willmann, P. Mayrhofer, P. Persson, A. Reiter, L. Hultman, and C. Mitterer, Scripta Mater. **54**, 1847 (2006).

[8] Y. Ide, T. Nakamura, and K. Kishitake, in *Proceedings of the Second International Conference on Processing Materials for Properties*, edited by B. Mishra and C. Yamauchi (2000), pp. 291–296.
[9] M. Kawate, A. Hashimoto, and T. Suzuki, Surf. Coat. Technol. **165**, 163 (2003).
[10] O. Banakh, P. Schmid, R. Sanjinés, and F. Lévy, Surf. Coat. Technol. **163-164**, 57 (2003).
[11] J. Endrino, G. Fox-Rabinovich, A. Reiter, S. Veldhuis, R. Escobar Galindo, J. Albella, and J. Marco, Surf. Coat. Technol. **201**, 4505 (2007).
[12] A. E. Reiter, C. Mitterer, and B. Sartory, J. Vac. Sci. Technol. A **25**, 711 (2007).
[13] W. Kalss, A. Reiter, V. Derflinger, C. Gey, and J. Endrino, Int. J. Refract. Met. Hard Mater. **24**, 399 (2006).
[14] G. Fox-Rabinovich, B. Beake, J. Endrino, S. Veldhuis, R. Parkinson, L. Shuster, and M. Migranov, Surf. Coat. Technol. **200**, 5738 (2006).
[15] J. Endrino, G. Fox-Rabinovich, and C. Gey, Surf. Coat. Technol. **200**, 6840 (2006).
[16] C. Nouveau, C. Labidi, J.-P. Martin, R. Collet, and A. Djouadi, Wear **263**, 1291 (2007).
[17] R. Franz, B. Sartory, R. Kaindl, R. Tessadri, A. Reiter, V. Derflinger, P. Polcik, and C. Mitterer, in *16th International Plansee Seminar*, edited by G. Kneringer, P. Rödhammer, and H. Wildner (Reutte, Austria, 2005), vol. 2, pp. 932–945.
[18] M. Woydt, A. Skopp, I. Dörfel, and K. Witke, Wear **218**, 84 (1998).
[19] A. Erdemir, Tribol. Lett. **8**, 97 (2000).
[20] W.-D. Münz, L. Donohue, and P. Hovsepian, Surf. Coat. Technol. **125**, 269 (2000).
[21] P. Mayrhofer, P. Hovsepian, C. Mitterer, and W.-D. Münz, Surf. Coat. Technol. **177-178**, 341 (2004).
[22] K. Kutschej, P. Mayrhofer, M. Kathrein, P. Polcik, and C. Mitterer, Surf. Coat. Technol. **188-189**, 358 (2004).
[23] R. Franz, J. Neidhardt, B. Sartory, R. Kaindl, R. Tessadri, P. Polcik, V. Derflinger, and C. Mitterer, Tribol. Lett. **23**, 101 (2006).
[24] D. R. Lide, ed., *CRC Handbook of Chemistry and Physics* (CRC Press, 2004), 85th ed.
[25] J. Galy, A. Ratuszna, J. Iglesias, and A. Castro, Solid State Sci. **8**, 1438 (2006).
[26] Z. Zhou, W. Rainforth, D. Lewis, S. Creasy, J. Forsyth, F. Clegg, A. Ehiasarian, P. Hovespian, and W.-D. Münz, Surf. Coat. Technol. **177-178**, 198 (2004).
[27] D. Lewis, S. Creasey, Z. Zhou, J. Forsyth, A. Ehiasarian, P. Hovsepian, Q. Luo, W. Rainforth, and W.-D. Münz, Surf. Coat. Technol. **177-178**, 252 (2004).
[28] K. Kutschej, P. Mayrhofer, M. Kathrein, P. Polcik, and C. Mitterer, Surf. Coat. Technol. **200**, 1731 (2005).
[29] R. Franz, J. Neidhardt, B. Schaffer, H. Hutter, R. Kaindl, B. Sartory, R. Tessadri, M. Lechthaler, P. Polcik, and C. Mitterer, J. Vac. Sci. Technol. A (submitted).
[30] R. Franz, J. Neidhardt, B. Sartory, R. Tessadri, and C. Mitterer, Thin Solid Films (submitted).
[31] W. Oliver and G. Pharr, J. Mater. Res. **7**, 1564 (1992).
[32] P. Mayrhofer and C. Mitterer, Surf. Coat. Technol. **133-134**, 131 (2000).
[33] V. Brázdová, M. Ganduglia-Pirovano, and J. Sauer, J. Phys. Chem. B **109**, 394 (2005).